



Wireless Power Transfer for Combined Sensing and Stimulation in Implantable Biomedical Devices

Thèse

Esmaeel Maghsoudloo

Doctorat en génie électrique
Philosophiæ doctor (Ph.D.)

Québec, Canada

© Esmaeel Maghsoudloo, 2018

Résumé

Actuellement, il existe une forte demande de Headstage et de microsystèmes intégrés implantables pour étudier l'activité cérébrale de souris de laboratoire en mouvement libre. De tels dispositifs peuvent s'interfacer avec le système nerveux central dans les paradigmes électriques et optiques pour stimuler et surveiller les circuits neuronaux, ce qui est essentiel pour découvrir de nouveaux médicaments et thérapies contre des troubles neurologiques comme l'épilepsie, la dépression et la maladie de Parkinson. Puisque les systèmes implantables ne peuvent pas utiliser une batterie ayant une grande capacité en tant que source d'énergie primaire dans des expériences à long terme, la consommation d'énergie du dispositif implantable est l'un des principaux défis de ces conceptions.

La première partie de cette recherche comprend notre proposition de la solution pour diminuer la consommation d'énergie des microcircuits implantables. Nous proposons un nouveau circuit de décalage de niveau qui convertit les niveaux de signaux sub-seuils en niveaux ultra-bas à haute vitesse en utilisant une très faible puissance et une petite zone de silicium, ce qui le rend idéal pour les applications de faible puissance. Le circuit proposé introduit une nouvelle topologie de décaleur de niveau de tension utilisant un condensateur de décalage de niveau pour augmenter la plage de tensions de conversion, tout en réduisant considérablement le retard de conversion. Le circuit proposé atteint un délai de propagation plus court et une zone de silicium plus petite pour une fréquence de fonctionnement et une consommation d'énergie donnée par rapport à d'autres solutions de circuit. Les résultats de mesure sont présentés pour le circuit proposé fabriqué dans un processus CMOS TSMC de 0,18- μm . Le circuit présenté peut convertir une large gamme de tensions d'entrée de 330 mV à 1,8 V et fonctionner sur une plage de fréquence de 100 Hz à 100 MHz. Il a un délai de propagation de 29 ns et une consommation d'énergie de 61,5 nW pour les signaux d'entrée de 0,4 V, à une fréquence de 500 kHz, surpassant les conceptions précédentes.

La deuxième partie de cette recherche comprend nos systèmes de transfert d'énergie sans fil proposé pour les applications optogénétiques. L'optogénétique est la combinaison de la méthode génétique et optique d'excitation, d'enregistrement et de contrôle des neurones biologiques. Ce système combine plusieurs technologies telles que les MEMS et la microélectronique pour collecter et transmettre les signaux neuronaux et activer un stimulateur optique via une liaison sans fil. Puisque les stimulateurs optiques consomment plus de puissance que les stimulateurs électriques, l'interface utilise la transmission de puissance par induction en utilisant des moyens innovants au lieu de la batterie avec la

petite capacité comme source d'énergie.

Notre première contribution dans la deuxième partie fournit un système de cage domestique intelligent basé sur des barrettes multi-bobines superposées à travers un récepteur multicellulaire implantable mince de taille $1 \times 1 \text{ cm}^2$, implanté sous le cuir chevelu d'une souris de laboratoire, et unité de gestion de l'alimentation intégrée. Ce système inductif est conçu pour fournir jusqu'à 35,5 mW de puissance délivrée à un émetteur-récepteur full duplex de faible puissance entièrement intégré pour prendre en charge des implants neuronaux à haute densité et bidirectionnels. L'émetteur (TX) utilise une bande ultra-large à impulsions radio basée sur des approches de combinaison, et le récepteur (RX) utilise une topologie à bande étroite à incrémentation de 2,4 GHz. L'émetteur-récepteur proposé fournit un débit de données de liaison montante TX à 500 Mbits/s double et un débit de données de liaison descendante RX à 100 Mbits/s, et est entièrement intégré dans un processus CMOS TSMC de $0,18\text{-}\mu\text{m}$ d'une taille totale de $0,8 \text{ mm}^2$. La puissance peut être délivrée à partir d'un signal de porteuse de 13,56-MHz avec une efficacité globale de transfert de puissance supérieure à 5% sur une distance de séparation allant de 3 cm à 5 cm.

Notre deuxième contribution dans les systèmes de collecte d'énergie porte sur la conception et la mise en œuvre d'une cage domestique de transmission de puissance sans fil (WPT) pour une plate-forme de neurosciences entièrement sans fil afin de permettre des expériences optogénétiques ininterrompues avec des rongeurs de laboratoire vivants. La cage domestique WPT utilise un nouveau réseau hybride de transmetteurs de puissance (TX) et des résonateurs multi-bobines segmentés pour atteindre une efficacité de transmission de puissance élevée (PTE) et délivrer une puissance élevée sur des distances aussi élevées que 20 cm. Le récepteur de puissance à bobines multiples (RX) utilise une bobine RX d'un diamètre de 1 cm et une bobine de résonateur d'un diamètre de 1,5 cm. L'efficacité moyenne du transfert de puissance WPT est de 29,4%, à une distance nominale de 7 cm, pour une fréquence porteuse de 13,56 MHz. Il a des PTE maximum et minimum de 50% et 12% le long de l'axe Z et peut délivrer une puissance constante de 74 mW pour alimenter le headstage neuronal miniature. En outre, un dispositif implantable intégré dans un processus CMOS TSMC de $0,18\text{-}\mu\text{m}$ a été conçu et introduit qui comprend 64 canaux d'enregistrement, 16 canaux de stimulation optique, capteur de température, émetteur-récepteur et unité de gestion de l'alimentation (PMU). Ce circuit est alimenté à l'intérieur de la cage du WPT à l'aide d'une bobine réceptrice d'un diamètre de 1,5 cm pour montrer les performances du circuit PMU. Deux tensions régulées de 1,8 V et 1 V fournissent 79 mW de puissance pour tout le système sur une puce.

Notre dernière contribution est un système WPT insensible aux désalignements angulaires pour alimenter un headstage pour des applications optogénétiques qui a été précédemment proposé par le Laboratoire de Microsystèmes Biomédicaux (BioML-UL) à ULAVAL. Ce système est la version étendue de notre deuxième contribution aux systèmes de collecte d'énergie. Dans la version mise à jour, un récepteur de puissance multi-bobines utilise une bobine RX d'un diamètre de 1,0 cm et une nouvelle bobine de résonateur fendu d'un diamètre de 1,5 cm, qui résiste aux défauts d'alignement angulaires. Dans cette version qui utilise une cage d'animal plus petite que la dernière version, 4 résonateurs sont

utilisés côté TX. De plus, grâce à la forme et à la position de la bobine de répéteur L_3 du côté du récepteur, la liaison résonnante hybride présentée peut correctement alimenter la tête sans interruption causée par le désalignement angulaire dans toute la cage de la maison. Chaque 3 tours du répéteur RX a été enveloppé avec un diamètre de 1,5 cm, sous différents angles par rapport à la bobine réceptrice. Les résultats de mesure montrent un PTE maximum et minimum de 53 % et 15 %. La méthode proposée peut fournir une puissance constante de 82 mW pour alimenter le petit headstage neural pour les applications optogénétiques. De plus, dans cette version, la performance du système est démontrée dans une expérience *in-vivo* avec une souris ChR2 en mouvement libre qui est la première expérience optogénétique sans fil et sans batterie rapportée avec enregistrement électrophysiologique simultané et stimulation optogénétique. L'activité électrophysiologique a été enregistrée après une stimulation optogénétique dans le Cortex Cingulaire Antérieur (CAC) de la souris.

Abstract

Currently, there is a high demand for Headstage and implantable integrated microsystems to study the brain activity of freely moving laboratory mice. Such devices can interface with the central nervous system in both electrical and optical paradigms for stimulating and monitoring neural circuits, which is critical to discover new drugs and therapies against neurological disorders like epilepsy, depression, and Parkinson's disease. Since the implantable systems cannot use a battery with a large capacity as a primary source of energy in long-term experiments, the power consumption of the implantable device is one of the leading challenges of these designs.

The first part of this research includes our proposed solution for decreasing the power consumption of the implantable microcircuits. We propose a novel level shifter circuit which converting subthreshold signal levels to super-threshold signal levels at high-speed using ultra low power and a small silicon area, making it well-suited for low-power applications such as wireless sensor networks and implantable medical devices. The proposed circuit introduces a new voltage level shifter topology employing a level-shifting capacitor to increase the range of conversion voltages, while significantly reducing the conversion delay. The proposed circuit achieves a shorter propagation delay and a smaller silicon area for a given operating frequency and power consumption compared to other circuit solutions. Measurement results are presented for the proposed circuit fabricated in a 0.18- μm TSMC CMOS process. The presented circuit can convert a wide range of the input voltages from 330 mV to 1.8 V, and operate over a frequency range of 100-Hz to 100-MHz. It has a propagation delay of 29 ns, and power consumption of 61.5 nW for input signals 0.4 V, at a frequency of 500-kHz, outperforming previous designs.

The second part of this research includes our proposed wireless power transfer systems for optogenetic applications. Optogenetics is the combination of the genetic and optical method of excitation, recording, and control of the biological neurons. This system combines multiple technologies such as MEMS and microelectronics to collect and transmit the neuronal signals and to activate an optical stimulator through a wireless link. Since optical stimulators consume more power than electrical stimulators, the interface employs induction power transmission using innovative means instead of the battery with the small capacity as a power source.

Our first contribution in the second part provides a smart home-cage system based on overlapped multi-coil arrays through a thin implantable multi-coil receiver of $1 \times 1 \text{ cm}^2$ of size, implantable bel-

low the scalp of a laboratory mouse, and integrated power management circuits. This inductive system is designed to deliver up to 35.5 mW of power delivered to a fully-integrated, low-power full-duplex transceiver to support high-density and bidirectional neural implants. The transmitter (TX) uses impulse radio ultra-wideband based on an edge combining approach, and the receiver (RX) uses a 2.4-GHz on-off keying narrow band topology. The proposed transceiver provides dual-band 500-Mbps TX uplink data rate and 100-Mbps RX downlink data rate, and it is fully integrated into 0.18- μm TSMC CMOS process within a total size of 0.8 mm^2 . The power can be delivered from a 13.56-MHz carrier signal with an overall power transfer efficiency above 5% across a separation distance ranging from 3 cm to 5 cm.

Our second contribution in power-harvesting systems deals with designing and implementation of a WPT home-cage for a fully wireless neuroscience platform for enabling uninterrupted optogenetic experiments with live laboratory rodents. The WPT home-cage uses a new hybrid parallel power transmitter (TX) coil array and segmented multi-coil resonators to achieve high power transmission efficiency (PTE) and deliver high power across distances as high as 20 cm. The multi-coil power receiver (RX) uses an RX coil with a diameter of 1 cm and a resonator coil with a diameter of 1.5 cm. The WPT home-cage average power transfer efficiency is 29.4%, at a nominal distance of 7 cm, for a power carrier frequency of 13.56-MHz. It has maximum and minimum PTE of 50% and 12% along the Z axis and can deliver a constant power of 74 mW to supply the miniature neural headstage. Also, an implantable device integrated into a 0.18- μm TSMC CMOS process has been designed and introduced which includes 64 recording channels, 16 optical stimulation channels, temperature sensor, transceiver, and power management unit (PMU). This circuit powered up inside the WPT home-cage using receiver coil with a diameter of 1.5 cm to show the performance of the PMU circuit. Two regulated voltages of 1.8 V and 1 V provide 79 mW of power for all the system on a chip.

Our last contribution is an angular misalignment insensitive WPT system to power up a headstage which has been previously proposed by the Biomedical Microsystems Laboratory (BioML-UL) at ULaval for optogenetic applications. This system is the extended version of our second contribution in power-harvesting systems. In the updated version a multi-coil power receiver uses an RX coil with a diameter of 1.0 cm and a new split resonator coil with a diameter of 1.5 cm, which is robust against angular misalignment. In this version which is using a smaller animal home-cage than the last version, 4 resonators are used on the TX side. Also, thanks to the shape and position of the repeater coil of L_3 on the receiver side, the presented hybrid resonant link can properly power up the headstage without interruption caused by the angular misalignment all over the home-cage. Each 3 turns of the RX repeater has been wrapped up with a diameter of 1.5 cm, in different angles compared to the receiver coil. Measurement results show a maximum and minimum PTE of 53 % and 15 %. The proposed method can deliver a constant power of 82 mW to supply the small neural headstage for the optogenetic applications. Additionally, in this version, the performance of the system is demonstrated within an *in-vivo* experiment with a freely moving ChR2 mouse which is the first fully wireless and batteryless optogenetic experiment reported with simultaneous electrophysiological

cal recording and optogenetic stimulation. Electrophysiological activity was recorded after delivering optogenetic stimulation in the Anterior Cingulate Cortex (ACC) of the mouse.

Table des matières

Résumé	iii
Abstract	vi
Table des matières	ix
Liste des tableaux	xi
Liste des figures	xii
Remerciements	xxi
Remerciements	xxii
Avant-propos	xxiii
Introduction	1
1.1 Electrical Stimulation	2
1.2 Optical Stimulation	4
1.3 Power Transmission Systems for Biomedical Applications	6
1.4 Specific Absorption Rate	7
1.5 Objectives of This Thesis	8
1.6 Low Power Design Techniques	10
1.7 Inductive Power Link	11
1.8 Review of Literature	13
1.9 Contributions	16
1.10 Thesis Outline	18
2 A High-Speed and Ultra Low-Power Subthreshold Signal Level Shifter	20
Résumé	20
Abstract	21
2.1 Introduction	22
2.2 Proposed LS Design	24
2.3 Implementation and Simulation Results	28
2.4 Measurement Results	31
2.5 Discussion and Comparison	36
2.6 Conclusion	38

3	A Wirelessly Powered High-Speed Transceiver for High-Density Bidirectional Neural Interfaces	39
	Résumé	39
	Abstract	40
	3.1 Introduction	41
	3.2 System Overview	42
	3.3 Inductive Power Transmission System Design	44
	3.4 Measurement Results	46
	3.5 Conclusion	49
4	A Smart Neuroscience Platform with Wireless Power Transmission for Simultaneous Optogenetics and Electrophysiological Recording	50
	Résumé	50
	Abstract	52
	4.1 Introduction	53
	4.2 System Overview	55
	Wireless Neural Headstage	55
	Hybrid Resonant Link	55
	Wireless Neuro Interfacing Microsystem	57
	Motion Tracking System	60
	4.3 Measurement Results	61
	Powered up Headstage Moving Inside WPT Home-cage	61
	Measured Performances of The Implantable Device Inside WPT Home-cage	62
	4.4 Conclusion	64
5	A Wireless Neuroscience Platform for Uninterrupted Optogenetics and Electrophysiology Recording in Live Animals	65
	Résumé	65
	Abstract	67
	5.1 Introduction	68
	5.2 System Overview	71
	5.3 System Design	72
	Wireless Neural Headstage and Base Station	72
	Hybrid WPT Home-Cage System	72
	5.4 Experimental Results	77
	Measured Performance	77
	<i>in-vivo</i> Results	81
	Surgical procedure	81
	Freely moving extracellular recordings	83
	5.5 Conclusion	84
6	Discussion and conclusion	86
	Discussion	86
	Conclusion	88
	publication	90
	Bibliographie	92

Liste des tableaux

2.1	THE CIRCUIT ELEMENTS SIZES	27
2.2	MEASUREMENT COMPARISON TO THE FABRICATED LS DESIGNS	38
3.1	SPECIFICATIONS OF THE IMPLEMENTED SPIRAL COILS	46
3.2	PARAMETER COMPARISON WITH THE STATE OF THE ART	48
4.1	SPECIFICATIONS OF THE COILS USED IN THE WPT HOME-CAGE	57
4.2	PERFORMANCE SUMMARY AND COMPARISON WITH THE STATE-OF-THE-ART	64
5.1	SPECIFICATIONS OF THE COILS USED IN THE WPT HOME-CAGE	76
5.2	MEASURED PTE COMPARISON OF THREE WPT TOPOLOGIES	78
5.3	PERFORMANCE SUMMARY AND COMPARISON OF PROPOSED WPTS WITH THE STATE OF THE ART	80
5.4	PERFORMANCE SUMMARY AND COMPARISON OF THE WIRELESS HEAD-STAGE WITH THE STATE OF THE ART	81

Liste des figures

1.1	A typical biphasic stimulation current waveform [22].	3
1.2	The photosensitive channelrhodopsin2 (ChR2) ion channels expressed in neurons allow the polarization of the cells by sodium (Na) [36].	4
1.3	Illustration of the limitations of electrical stimulation and the benefits of INS. (a) Threshold electrical stimulation necessitates contact, evokes an action potential in both the gastrocnemius and biceps femoris fascicles, and is accompanied by a stimulation artifact. (b) Threshold INS is contact free and spatially precise as only the gastrocnemius fascicle is targeted [37].	5
1.4	Representation of the Wireless neural recording and stimulation architecture.	6
1.5	The SAR vs. frequency for human blood, bone, fat, and muscle[52].	7
1.6	(a)The block diagram of a wireless implantable system, (b) the schematic of implanted device of neural recording and Opto-stimulating system.	9
1.7	(a) Challenges of high power consumption, (b) low power design techniques and, (c) multi power domain interface.	10
1.8	(a) An inductive link between the TX and RX coils with a distance of d , (b) the geometrical parameters of a square-shaped printed spiral coil. (c) The ratio of the optimum diameter of TX [53] and (d) the maximum achievable coupling coefficient (k), as a function of the distance between TX and RX [53].	12
1.9	Circuit models of (a) 3-coil inductive power link [45] and (b) 4-coil inductive link [59]	14
1.10	Rendered view of the EnerCage system showing its modular architecture[64].	14
1.11	3D power transmitter made of several primary resonators (L2,1-L2,18) [48].	15
1.12	(a) A conceptual representation of the proposed EnerCage-HC2 system for wireless powering and communication with a headstage [67]. (b) The implemented prototypes of power transmission systems scaled down for mouse application.	16
2.1	Conventional level shifters based on : (a) cross-coupled structure, (b) current mirror structure	22
2.2	The proposed level shifter circuit schematic based on a level-shifting capacitor.	23
2.3	Two operation cycles of the proposed LS circuit (a) low-to-high transition and (b) high-to-low transition of the input signal (c) time domain analysis for different nodes, from the input to the output, where t_{Id4} is the time interval during which the current source I_{D4} charges the capacitor C , while t_{pd1} and t_{pd2} are the propagation delays associated to low-to-high and high-to-low transitions, respectively.	25
2.4	Equivalent circuits of the inverter chain of the proposed LS.	27
2.5	Simulated waveforms of (a) the input and output voltages of the proposed circuit with $V_{DDL} = 0.4$ V and $V_{DDH} = 1.8$ V, (b) the current source of I_{D4}	29
2.6	Monte Carlo simulation results of the delay distribution for $V_{DDH} = 1.8$ V, $V_{DDL} = 0.4$ V and $T = 27^\circ\text{C}$	29

2.7	Transient response of the proposed circuit (a) with capacitor C , and (b) without capacitor C	30
2.8	The variation of the delay of the proposed circuit across PVT corners.	32
2.9	(a) Chip micrograph, (b) partially enlarged view of the test circuit with output buffer and (c) chip view of the proposed LS (area : $229.5 \mu m^2$).	32
2.10	Effect of V_{DDL} on the maximum operating frequency.	33
2.11	Power consumption variation with frequency for different V_{DDL}	33
2.12	Measured waveforms of the level shifter at 500-kHz input pulse with amplitude of 400 mVp-p to 1.8 Vp-p.	34
2.13	(a) Rise transition delay and (b) fall transition delay of the measured signal of the test chip at 500-kHz input pulse with amplitude of 400 mVp-p into 1.8 Vp-p.	35
2.14	Measured variation of the delay and power consumption for different V_{DDL} at $V_{DDH}=1.8$ V and 500-kHz.	36
2.15	Measured variation of the delay and power consumption for different V_{DDH} at $V_{DDL}=0.4$ V and 500-kHz.	37
3.1	The proposed implantable neural recording and stimulating brain machine interface including an inductive power link and a CMOS system on a chip including power recovery circuits and a full-duplex transceiver.	42
3.2	(a) Fabricated multi-icoil array including two 50%-overlapping FR4 layers. (b) The top FR4 layer of the inductive array (c) the bottom FR4 layer of the inductive array (d) the two FR4 layers are superimposed (a+b) for implementing a surface providing uniform power transmission density.	43
3.3	(a) The full block diagram of the power transmission system includes a Class E power amplifier, a 5-coil inductive link, a rectifier, a regulator and end load. (b) The measured transmission coefficient of the 3-coil link and 5-coil link (for a single resonator and the power surface) at frequency of 13.56-MHz.	44
3.4	Implemented power surface prototype located below a mouse home-cage and proposed wireless implantable device.	45
3.5	(a) Measured power delivered to the load and power transfer efficiency of the multi-icoil inductive link along the Z axis. (b) The measured voltage of the rectifier and regulator at $d=4$ cm.	46
3.6	The measured output data of the transmitter while powered up by the proposed 5-coil inductive link showing the generated short-impulse transmitter signals using BPSK modulation at a rate of 100 Mbps.	47
3.7	The chip micrograph of the fabricated circuit in a CMOS 180-nm process.	48
4.1	Representation of the wireless neuroscience platform including a wireless neural headstage, a multi-coil resonant WPT system, a motion tracking system and a wireless base station.	53
4.2	(a) WPT home-cage prototype, and animal motion tracking system, (b) overview of the 4-coil resonant link including the primary coil array (L_{1i}) and the segmented resonators (L_{2i}), (c) measured transmission coefficient of the 4-coil resonant link, (d) the wireless headstage and the multicoil receiver, including the RX resonator (L_3) and the RX secondary coil (L_4).	55
4.3	Schematic of the equivalent circuit of the proposed wireless power transfer system.	56
4.4	Block diagram of the proposed system.	58
4.5	The block diagram of the PMU circuit.	59

4.6	Die photograph of the chip fabricated in a 0.180- μm CMOS process and occupying 3 mm x 4 mm.	59
4.7	(a) Motion tracking system, (b) user interface of the tracking system showing the tracking path, (c) measured voltage retrieved by the power RX on the headstage side (voltage across capacitor C_R), and (d) motion tracking path of an object moving inside the home-cage.	60
4.8	(a) Measured 200- $\mu\text{Vp-p}$ input synthetic neural signals using the headstage powered up wirelessly inside the home-cage with the WPT system, (b) an isolated recorded synthetic spike, and (c) the LED forward current provided by the wireless power link.	61
4.9	The PCB prototype.	62
4.10	The rectified voltage measured while the implantable device powered up inside WPT home-cage.	63
4.11	The regulated voltages of 1.8 V and 1 V measured while the implantable device powered up inside WPT home-cage.	63
5.1	Conceptual representation of the proposed wireless platform for combined optogenetics and electrophysiology experiments. It includes a hybrid (multi-coil/segmented) resonant link, a wireless multichannel optoelectronic headstage and a base station. . .	68
5.2	(a) The wireless platform, (b) WPT home-cage prototype, (c) the compact folded PCB, (d) the head mountable PCB housing with split power transmission coils including the RX resonator (L_{3i}) and the RX secondary coil (L_4), and (e) the encapsulated headstage.	70
5.3	Overall block diagram of the wireless neuroscience platform. (a) The animal home-cage consists of a power source, a class E power amplifier, TX primary parallel coil array (L_{1i}) and TX resonator segmented coil array (L_{2i}). (b) The headstage includes a split RX resonator coil array (L_{3i}), a RX secondary coil (L_4), a neural recording chip, a 2.4-GHz ISM wireless transceiver, a power management unit, a low-power MCU, an LED driver, and an optrode including one implantable fiber optic and 4 microelectrodes. (c) The base station consists of a 2.4-GHz ISM wireless transceiver, a low power MCU, a USB controller and a user interface running on a nearby computer.	71
5.4	(a) The PCB of the headstage, (b) the compact folded PCB, (c) the head mountable PCB housing with split power transmission resonator coils, and the RX coil, and (d) USB dongle including a transceiver, an antenna, and USB interface connected to the base station.	73
5.5	The definition of the movement directions of the head of the mouse.	74
5.6	The measured PTE of the WPTS as a function of the misalignment angle (see Fig. 5) for three L_{3i} configurations : (a) along the angle α , (b) along the angle β	75
5.7	The circuit schematic of the proposed WPT system based on a 4-coil structure including a power driver, a primary TX coil array, four TX resonators, an RX resonator, an RX secondary coil, a rectifier and a regulator.	76
5.8	The 4-coil resonant link optimization procedure considering the carrier of 13.56 Hz, the size of the animal home-cage, the size and weight of the RX unit, and the expected separation distance of the RX and TX coils.	77
5.9	The implemented power transmission system prototypes. (a) Power surface resonator array (WPTS1), (b) copper foil resonators using one coil as a primary TX (WPTS2) and (c) copper foil resonator using 3 TX paralleled coils as a primary TX array (WPTS3).	78
5.10	The measured PTE when the receiver is swept inside the cage across the X-Y at a distance of $d=5$ cm.	79

5.11 (a) Experimental measurement setup. (b) Implanted headstage on the head of a ChR2 transgenic mouse.	82
5.12 Recorded spontaneous neural activity without any optical stimulation.	83
5.13 Measured voltage retrieved by the power RX on the headstage side (voltage across capacitor C_R).	84
5.14 The experimental results showing extracellular recordings in the brain of a ChR2 mouse in response to local optogenetic light activation of 10 ms with a period of 2 s. APs with amplitude of up to 1.1 mV were evoked by the light activation.	85

Abbreviations

2D	2-Dimension
3D	3-Dimension
AC	Alternating Current
ACC	Anterior Cingulate Cortex
AFE	Analog Front-End
ANSI	American National Standards Institute
AWG	American Wire Gauge
BCC	Best Case Corner
BioML-UL	Biomedical Microsystems Laboratory-Université Laval
BMI	Brain Machine Interface
BPSK	Binary Phase Shift Keying
BW	Bandwidth
CMOS	Complementary Metal-Oxide Semiconductor
CRIUSMQ	Quebec Mental Health Institute Research Center
DC	Direct Current
DVFS	Dynamic Voltage -Frequency Scaling
EMC	Electromagnetic Compatibility
FOM	Figure Of Merit
FR4	Flame Retardant-4
IMD	Implantable Medical Device
ISM	Industrial, Scientific and Medical
LDO	Low-Dropout Regulator
LED	Light Emitting Diode
LFP	Local Field Potentials
LNA	Low-Noise Amplifier
LRTS	Laboratoire de Radiocommunication et de Traitement du Signal
LS	Level Shifter
MCU	Micro-Controller Unit
MEMS	Microelectromechanical systems
MOSCAP	Metal Oxide Semiconductor Capacitor

MOSFET	Metal-Oxide-Semiconductor Field-Effect Transistor
NMOS	Negative-channel Metal-Oxide Semiconductor
OOK	On-Off Keying
OSRAM	Oil Spill Risk Analysis Model
PC	Personal Computer
PCB	Printed Circuit Boards
PDL	Power Delivered to the Load
PMOS	Positive-channel Metal-Oxide Semiconductor
PMU	Power Management Unit
PTE	Power Transfer Efficiency
PVT	Process, Voltage and Temperature
RF	Radio Frequency
RFIC	Radio Frequency Integrated Circuit
RX	Receiver
SAR	Specific Absorption Rate
SNR	Signal-to-Noise Ratio
SoC	Systems on Chip
TCC	Typical Case Corner
TI	Texas Instrument
TX	Transmitter
USB	Universal Serial Bus
VDD	Drain supply Voltage
WCC	Worst Case Corner
WPT	Wireless Power Transmission

List of symbols

C	Capacitor
C_{DS}	The drain-source capacitance of transistor
C_{gmin}	The modeling parameter
C_G	The gate capacitance of transistor
C_{GS}	The gate-source capacitance of transistor
C_i	Capacitor number i
C_p	Parasitic Capacitor
d	Separation distance
d_i	Inner diameter of coil
d_O	Outer diameter of coil
d_{OR}	Outer diameter of coil
d_R	Diameter of receiver coil
d_T	Diameter of transmitter coil
f	Frequency
I_D	Drain current of transistor
$K_{i,j}$	Coupling between Coils number i and j
l_c	The length of the conductive trace in printed coil
L	Inductance of coil
L_i	Inductance of coil number i
$M_{i,j}$	Mutual inductance between coils number i and j
M_r	The number of gate fingers of transistor
n	Quantity of coil elements in parallel
N	Number of turns in coil element
P	Density of power
P_{in}	Input power
P_j	The bulk junction bottom potential
P_{out}	Output power
Q	Quality factor of coil element
R	Resistor
R_{eq}	The equivalent series resistance

R_G	The gate resistance
R_L	Load resistor
R_S	Source resistor
S	The line's space in printed coil
S_{21}	Scattering parameter, transmission coefficient
t_c	The thickness of printed coil
V	Voltage
V_{DD}	Supply voltage
V_i	Voltage of node i
V_{out}	Output voltage
V_S	Source voltage
W	The line's width of printed coil
Z	Distance between TX and RX coils
Z_{in}	Equivalent input impedance
η	Power transfer efficiency
η_0	The impedance in free space
$\tau(\omega)$	Group Delay
μ_0	The permeability of space
ϕ	The fill factor
ρ_c	The resistivity of the conductive material in printed coil

To my wife Michèle,
and all my family

Acknowledgement

Firstly, I would like to express my sincere gratitude to my advisor Professor Benoit Gosselin for the continuous support of my PhD study and related research, motivation, and immense knowledge. I would also like to thank Professor Mohammad Sawan for his advice and great support. His guidance helped me in all the time of research and writing of this thesis. It is my great honour working under his supervision. Besides, I would like to thank the rest of my thesis committee for their insightful comments and encouragement.

I would also like to thank my team members Masoud Rezaei, Gabriel Gagnon-Turcotte, and Zahra Rezaei for their cooperation, help and support through the research.

Finally, I would like to thank my wife and my family for supporting me spiritually throughout writing my thesis and my life in general.

Foreword

The two chapters (3 and 4) of this thesis consist of the materials already published in International Symposium on Circuits and Systems (ISCAS), and the two other chapters (2 and 5) are including the materials previously published or under review in *IEEE Transactions on Circuits and Systems I* and *IEEE Transactions on Biomedical Circuits and Systems* respectively. In this thesis, text and figures have been modified to be consistent with the rest of the document. Additionally, some material which did not find a place in the original papers has been added. The introduction section has been most heavily modified.

Here, I detail my contributions to these 2 Transactions articles (chapter 2 and 5) and 2 Conference papers (chapter 3 and 4).

Paper 1 : E. Maghsoudloo, M. Rezaei, M. Sawan, and B. Gosselin, “A High-Speed and Ultra Low-Power Subthreshold Signal Level Shifter,” in *IEEE Transactions on Circuits and Systems I : Regular Papers*, vol. 64, no. 5, pp. 1164-1172, May 2017. This paper presents a novel level shifter circuit converting subthreshold signal levels to super-threshold signal levels at high-speed using ultra-low-power and a small silicon area, making it well-suited for low-power applications such as wireless sensor networks and implantable medical devices. The original idea is proposed by myself; the experiments were conducted at Smart Biomedical Microsystems Laboratory at Laval University under the supervision of Dr. Gosselin. I have integrated the proposed circuit and fabricated in a 0.18- μm TSMC CMOS process, and tested it the Lab. I was assisted in the experiments and integration by my supervisor Dr. Gosselin, and Masoud Rezaei, a PhD student within our group. I prepared the manuscript, and the other authors revised it before submission. Dr. Sawan and Dr. Gosselin extensively revised the content of the paper, added material and corrected the English.

Paper 2 : E. Maghsoudloo, M. Rezaei, and B. Gosselin, “A Wirelessly Powered High-Speed Transceiver for High-Density Bidirectional Neural Interfaces,” *IEEE International Symposium on Circuits and Systems (ISCAS)*, Baltimore, MD, 2017, pp. 1-4 (Invited paper). This paper is devoted to a wireless power transfer system based on the paralleled coil array strategy to power up a fully-integrated, low-power full-duplex transceiver to support high-density and bidirectional neural implants. This smart home-cage using the original idea of the smart home-cage system based on overlapped multi-coil arrays which is already introduced by Dr. Mirbozorgi in a paper entitled “A Smart cage with uniform wireless power distribution in 3D for enabling long-term experiments with freely moving animals,”

IEEE Trans. Biomed. Circuits Syst., vol. 10, no. 2, pp. 424–434, Apr. 2016. The idea of the 5-coil inductive link using a double-sided receiver coil which is the main approaches of the paper is proposed by Dr. Gosselin and myself. Beside the design of a low-power full-duplex transceiver introduced by Masoud Rezaei, a PhD student within our group. The experiments were conducted at Smart Biomedical Microsystems Laboratory at Laval University under the supervision of Dr. Gosselin. I was assisted in the experiments and Measurements by Masoud Rezaei. The manuscript was prepared by me and revised by the other authors before submission. Dr. Gosselin extensively revised the content of the paper, added material and corrected the English.

Paper 3 : E. Maghsoudloo, G. Gagnon-Turcotte, Z. Rezaei, and B. Gosselin, “A Smart Neuroscience Platform with Wireless Power Transmission for Simultaneous Optogenetics and Electrophysiological Recording,” *International Symposium on Circuits and Systems (ISCAS)*, (Accepted, February 2018). This paper explores a fully wireless neuroscience platform for enabling uninterrupted optogenetic experiments with live laboratory rodents. The original idea of the Wireless Power Transmission (WPT) home-cage using a 4-coil resonant link which is the main approach of the paper is proposed by myself which is the extended version of the WPT home-cage introduced by Dr. Mirbozorgi in a paper titled “A Wirelessly-Powered Homecage With Segmented Copper Foils and Closed-Loop Power Control,” in *IEEE Transactions on Biomedical Circuits and Systems*, vol. 10, no. 5, pp. 979-989, Oct. 2016. The measurement results have been done by the powering up an optogenetics headstage which is already introduced by Gabriel Gagnon-Turcotte, a PhD student within our group which is presented in this paper for *ISCAS* conference. I was assisted in the experiments by my supervisor Dr. Gosselin, Gabriel Gagnon-Turcotte and Zahra Rezaei, a PhD and master students, respectively, within our group. I prepared the manuscript, and the other authors revised it before submission. The paper was selected to be published in a special issue of *IEEE Transactions on Biomedical Circuits and Systems* 2018. Additionally, a power management unit (PMU) integrated into a 0.18- μm TSMC CMOS process designed by myself has been introduced in this chapter, and the measurement results related to this design powered up in WPT home-cage has been provided. Dr. Gosselin extensively revised the content of the paper, added material and corrected the English.

Paper 4 : E. Maghsoudloo, G. Gagnon-Turcotte, Z. Rezaei, C. Bories, I. Keramidis, Y. De Koninck, and B. Gosselin, “A Wireless Neuroscience Platform for Uninterrupted Optogenetics and Electrophysiology Recording in Live Animals,” *IEEE Transactions on Biomedical Circuits and Systems*, (Under review, 2018). This paper is devoted to studying of the Wireless Power Transmission (WPT) system for enabling uninterrupted optogenetic experiments with live laboratory rodents. The original idea of the inductive link to solve the angular misalignment for optogenetics applications which is the main idea of the paper is proposed by myself under the supervision of Dr. Gosselin. The experiments were done by me, my supervisor Dr. Gosselin, Gabriel Gagnon-Turcotte, a PhD student within our group, Zahra Rezaei, a Master student within our group and with the valuable help of Cyril Bories and Iason Keramidis, the PhD students at Prof. Yves De Koninck’s lab in Quebec Mental Health Institute Research Center (CRIUSMQ). I prepared the manuscript with Gabriel Gagnon-Turcotte, and Zahra

Rezaei's help and Dr. Gosselin extensively revised the content of the paper, added material and corrected the English.

Introduction

In the past, monitoring biological electrical activities were done with expensive, bulky instruments that had several drawbacks. Since stationary devices were used to record biological activities, patients needed to be hospitalized during monitoring procedures. Now, this recording can be done on freely moving subjects using portable microsystems. Researchers have used this method for studying behavioural neuroscience and even special applications that diagnose diseases. Several studies have reported advances in neuroprostheses for both human and non-human primates [1–5]. Multielectrode neural recordings have even been used to check spike train of neurons in people with epilepsy [6]. This method can be used to detect and prevent the progress of the disease. Several types of broadband neural interface systems are recommended for animal and human applications. However, there are some limitations for the few acquisitions and stimulation channels since they have to use hardware systems as an interface to send the data to a processing site. Therefore, neural recordings experiments are only possible in a clinical environment.

Recent advances in microelectronics have enabled promising bioelectrical interfaces with enhanced complexity and functionality in this field. These devices have been broadly applied in areas ranging from clinical and research experiments to in-house treatments, and they are commercially available for biomedical applications. For example, some medically approved prostheses can be used to treat brain diseases, such as epilepsy and Parkinson’s disease. The NeuroPort system from Blackrock Microsystems, an FDA 510k (premarket approval), is the first multiunit recording system to have been approved for studying human neural activity [7]. This system has been used in clinical trials since 2005 in more than two dozen patients with spinal cord injuries or brainstem stroke to recognize and process the patients’ neural activity [1, 2], [8]. The interface decodes neural signals and uses them to control a robotic arm.

In these first neuroprostheses experiments, a cumbersome cable was used between the patient and the electronic parts. This cable limited the patient’s ability to move freely, and the electrical signal quality was affected by the long conductor path. The neural interface connection cables were eventually replaced with a short-range wireless link to improve the signal and allow the patient more mobility.

Over the past decade, several wireless recording systems have been proposed and developed for animal use [9–13]. One of these is the “Hermes” series of head-mounted wireless systems, which has been designed for primates [9, 10]. However, these systems were designed for specific primate-based

research and were not designed for potential human use. When designing a wireless neural recording system for human use, the design should include several features, such as simultaneous broadband multichannel recording, low power use, low-noise, and high data rate wireless communication. Such a design should also account for safety requirements for human clinical use, such as patient safety, moisture resistance, and Electromagnetic Compatibility (EMC) safety. However, the researchers must measure both the beneficial and the harmful effects of a compound on a whole organism. A neuroscientist is initially tested in vitro using tissues and isolated organs, but legally and ethically it must also be tested in a suitable animal model before clinical trials in humans can take place.

1.1 Electrical Stimulation

Electrode-based techniques have long been the preferred method for activating, modifying, recording, and studying neurons and their behavior [14–16]. While the depolarization of a neuron is usually achieved via synaptic currents, a propagating action potential may be caused following artificially made depolarization of the transmembrane potential through an electrical current. An electrode should be in contact with the axon or nerve fiber bundle to make an action potential in the axon. To generate an action potential, the transmembrane potential of a neuron must be depolarized beyond a certain threshold. The threshold can be defined as the minimum amplitude or pulse duration of an electrical current needed to induce an action potential. This value defines the quantity of charge transferred at the cathode [17]. The electrical stimulus amplitude can be controlled by either voltage or current. Depending on the application, they can also be used in tandem.

There are several advantages to using current-controlled stimuli. The injected charge can be calculated accurately regardless of whether the stimulation thresholds remain more or less constant. The accurate calculation of the injected charge is important as it controls the voltage of the electrode through the phase boundary. This regulated voltage allows for stimulation to be conducted without electrochemical reactions and tissue damage happening at the electrode-tissue interface [18]. Another important factor to account for electrical stimulation is the pulse duration of the electrical stimulus. A shorter pulse duration would need a larger amplitude to start an action potential [19, 20]. Although a longer pulse duration with a smaller amplitude would transfer the same total charge, it would carry a higher risk of tissue damage [21]. The charge threshold also increases with increasing pulse duration. In most neuroprosthetic applications, the pulse durations are on the order of 10 μ s to 100 μ s [17]. All the parameters of the stimulation, such as current, voltage, pulse-duration, and repetition rate, can be easily varied and measured. The waveform of the stimulation and the electrode configuration are also important parameters to be considered. Monophasic stimulation is one of the first methods developed to stimulate neural tissue, but this method causes tissue harm via electrochemical reactions (i.e. corrosion). Biphasic waveforms cause less tissue damage and are mainly used for long-term stimulation.

Fig. 1.1 shows the typical current waveform of a biphasic stimulation train. It is composed of a cathodic phase (area A) and an anodic phase (area B) separated by an inter-phase interval. Electrons

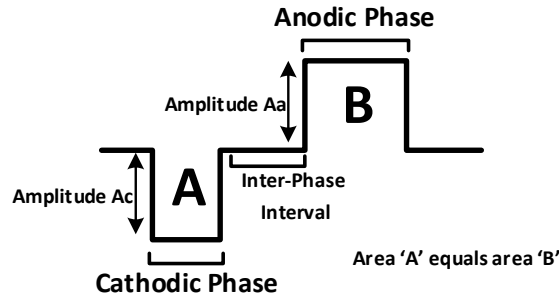


Figure 1.1 – A typical biphasic stimulation current waveform [22].

are injected into the tissue during the cathodic phase to elicit action potentials along the nerve fibre or axons and are removed during the anodic phase. A paper comparing stimulating waveforms and ranking their effectiveness in action potential initiation, tissue damage, and corrosion clearly explains how different electrode configurations, such as monopolar and bipolar electrodes, can be used to deliver different waveforms to tissues [22].

While monopolar electrodes have lower stimulation thresholds, using bipolar electrodes can reduce the current spread. Choosing an electrode configuration is dependent on the application [23–25]. Electrical stimulation is easy to control and adjust, and it is also more accurate, reliable, reproducible, and precise compared to other types of stimulation modalities, such as chemical, mechanical, or magnetic. Electrical stimulation is commonly used in applications such as the restoration of motor function, seizure control, and deep brain stimulation [17, 26, 27].

In electrical stimulation, an external current with a specific waveform but without any ionic identity is injected, which carries the membrane potential above its threshold to trigger an action potential (AP). Past studies have optimized the waveform for electrical stimulation in applications such as electronic pacemakers and defibrillators to make the waveforms more efficient at the minimum charge for neuroscience [28, 29] and cardiac applications [30, 31].

The physical restrictions of electrical stimulation systems limit neural stimulation. From the stimulus viewpoint, the galvanic pathway that occurs between the tissue and the electrode requires a precise charge balance to reduce leakage and prevent corrosion and tissue damage [32]. This problem is usually solved using coupling capacitors that increase the volume of the implant device and necessitate more stimulation circuitry. The conductivity of the electrode limits the level of electromagnetic exposure from conditions such as magnetic resonance imaging (MRI) and electrosurgery, which restrict post-implant treatment and diagnostics [33]. The use of electrical stimulation in driving neural circuits is also limited by electrode scaling, location, and surgical placement. In these situations, methods need to be designed to control the electrical field and the volume of stimulated tissue be able to compensate

for these limitations [34]. Also, while stimulating excited neurons in this way is efficient, preventing network activity is a power-wasteful process as it requires a high stimulation frequency [35].

Although electrical stimulation has been used for neural stimulation in clinical and research-based systems, it has several limitations. One of the disadvantages is that contact between the electrode and the neurons is required. While it is intuitive that the intracellular electrodes that spike the neurons will damage them, extracellular electrodes can also cause tissue harm.

Electrical stimulation causes two main types of damage : mechanical damage and electrochemical damage. Mechanical damage may happen because of tension on the nerve or displacement between the electrode and the nerve. Damage due to electrical stimulation, such as interstitial edema and early axonal degeneration, can result from electrochemical reactions at the electrode-tissue interface [17].

1.2 Optical Stimulation

Optogenetics is a method for controlling a neuron's activity using light and genetic engineering. Genetic engineering is a process where scientists change the information in the genetic code of a living thing. In optogenetic studies, scientists take the genetic code of the neurons they want to study and add a new piece of code to it.

The capacity to control and induce action potentials in neurons using light has been recognized for de-

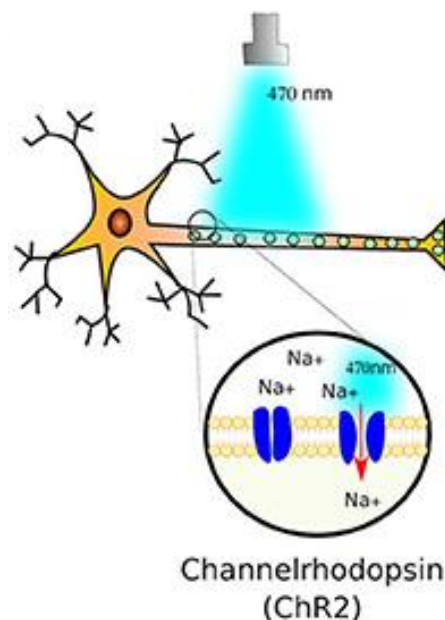


Figure 1.2 – The photosensitive channelrhodopsin2 (ChR2) ion channels expressed in neurons allow the polarization of the cells by sodium (Na) [36].

acades. After the discovery of caged compounds, Channelrhodopsin-2, and infrared neural stimulation (INS), light-based techniques have become more popular [36,37]. Caged compounds make known to into the cytoplasm of the cells or tissues and extract biomolecules inert until the light with a suitable wavelength that will not damage the cells release them [37]. Photo stimulation is a common method of conducting research on brain activity. However, this method has its limitations in spatiotemporal resolution [38]. Researchers have proven that neurons can be depolarized using light sensitive proteins such as *Chlamydomonas reinhardtii* Channelrhodopsin-2 (ChR2) or *Natronomonas pharaonis* halorhodopsin (NpHR) [36,39]. Fig. 1.2 shows Channelrhodopsin-2 (ChR2) which can be excited by blue light (a wavelength of 470 nm) and induced polarization by admitting sodium [40].

INS is a method that focuses on pulsed, low-intensity infrared light on a nerve to create a propagating action potential inside the neuron. Generally, INS can stimulate neurons while causing less damage to radiant exposures below the threshold [41–44].

Fig. 1.3 illustrates the advantages of INS compared to electrical stimulation. In electrical stimulation, contact with the neuron is required (Fig. 1.3(a)) while in INS, the light can be delivered to the nerve from the optical fiber without any contact (Fig. 1.3(b)). As shown in Fig. 1.3(a), the compound nerve action potentials (CNAPs) of the electrically stimulated nerve contain a stimulation artefact. This artefact is absent in INS (Fig. 1.3(b)). Also, INS has a higher resolution than electrical stimulation and requires the recruitment of fewer axons.

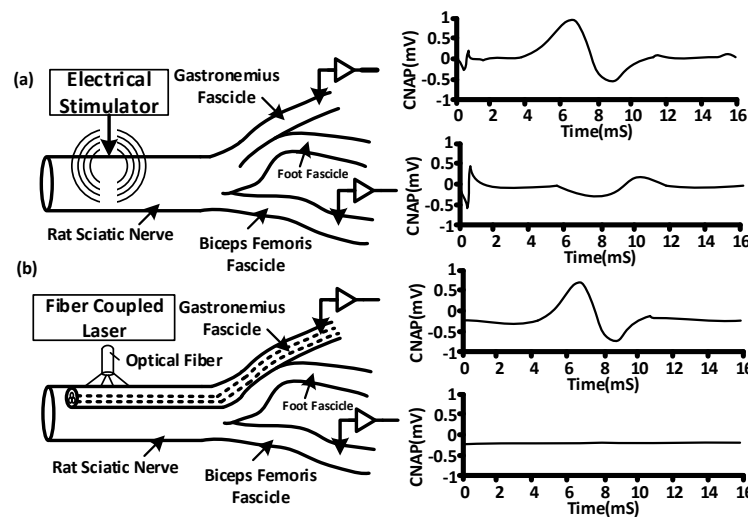


Figure 1.3 – Illustration of the limitations of electrical stimulation and the benefits of INS. (a) Threshold electrical stimulation necessitates contact, evokes an action potential in both the gastrocnemius and biceps femoris fascicles, and is accompanied by a stimulation artifact. (b) Threshold INS is contact free and spatially precise as only the gastrocnemius fascicle is targeted [37].

1.3 Power Transmission Systems for Biomedical Applications

Several neural prostheses have been developed based on nerve stimulation and recording as therapeutic systems which are the most efficient interface between the brain and the external world, called Brain Machine Interface (BMI) [9–11]. Acquisition of neural electrical activity via implanted electrode arrays has enabled a wide range of advances in electrophysiological experimentation towards basic neuroscience as well as neural prosthetics. A wireless neural recording and stimulation architecture is shown in Fig. 1.4, an electrode is implanted, and the data is sent through an antenna to a site outside of the body for processing, and the entire system is powered up inductively.

One of the most important aspects of neural stimulation and recording is powering up the system once it has been implanted under the skull [45–47]. Recently, researchers have presented methods for transferring power wirelessly to the whole implanted system. As shown in Fig. 1.4, this method uses a primary coil and a receiver coil. Humans and animals share hundreds of illnesses, and consequently, animals can act as models for the study of human illness. These make them natural candidates for research into these disorders. From such models, we learn how a disease affects the body, how the immune system responds, who will be affected, and more. Animals are widely used in neuroscience research to explore normal and abnormal biological mechanisms of nervous system function, to identify the genetic basis of disease states, and to provide models of human disorders and diseases for the development of new treatments. Therefore, before testing the implantable devices on human subjects, the verification of functionality and performance of these devices on freely moving animal subjects is essential. There

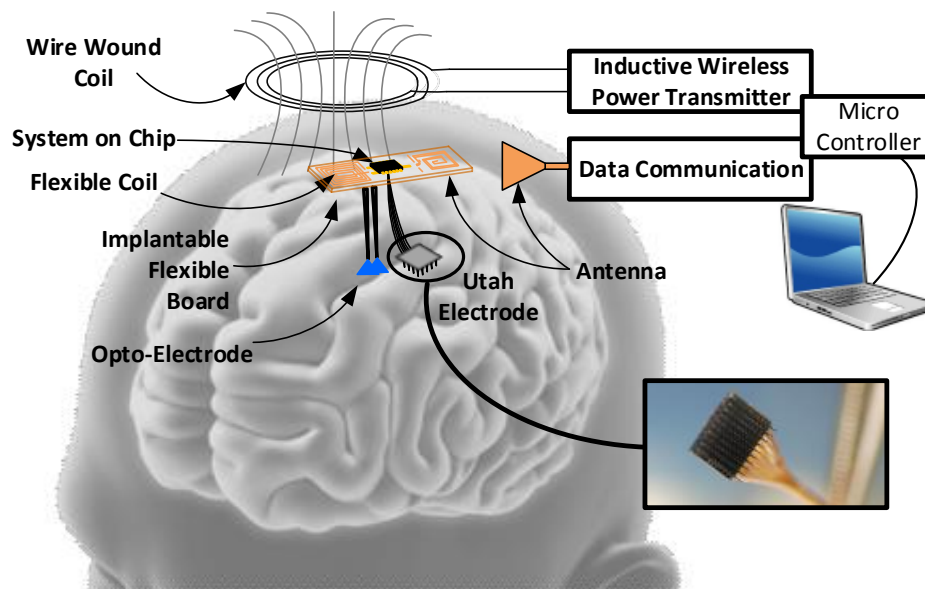


Figure 1.4 – Representation of the Wireless neural recording and stimulation architecture.

is a trade-off between the size of the receiver and the power delivered to the receiver coil. A larger receiver can receive more power, but receiver size is limited by the natural size of the animal under study [48].

Regarding the limitations of the weight and the thickness of the implantable board for the freely moving animal test, a flexible coil is used to provide the power of the implantable device. The system on a chip, illustrated in Fig. 1.4, is the circuit interface part of the neural recording and stimulation system. It includes an analog front-end stimulator circuit and a TX/RX wireless data transfer. The analog front-end is the first stage of the circuit interface at the recording site and is usually implemented by a filter stage at the input to remove the noise of the input data and a gain stage to increase the amplitude of the signal. Stimulator circuitry depends on the type of stimulus (electrical or optical) and will either include an LED driver or an electrical stimulator circuit. To transferring the data to the processor and to receive data through its antenna, the chip also needs to have a transceiver.

1.4 Specific Absorption Rate

A critical parameter for evaluating the tissue-safety of implantable wireless devices using the wireless link is the Specific Absorption Rate (SAR), which quantifies the rate at which energy is absorbed by biological tissues when exposed to a radio frequency (RF) electromagnetic field. The American National Standards Institute (ANSI) has specified a limitation of 1.6 W/kg [49], which translates into different average radiated power : approximately 6 mW (7.78 dBm) for the implanted antenna (the maximum power that the implanted UWB transmitter authorized to transmit) [50] and 9 mW (9.5 dBm) for the external antenna (maximum power that external 2.4 GHz transmitter allowed to transfer) [51]. Sending more power may damage the biological tissues.

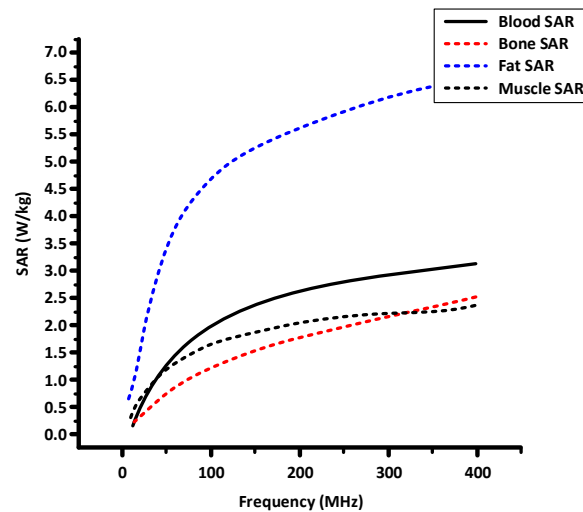


Figure 1.5 – The SAR vs. frequency for human blood, bone, fat, and muscle[52].

The relation between SAR of tissues and frequency is shown in Fig. 1.6. When the resonant frequency of the wireless power transfer system is 50 MHz, the SNR for human fat is about 2.7 times higher than human blood, 4.5 times than human bone and 2.8 times than human muscle. However, if the frequency is up to 200 MHz, the SAR for the fat is 2.2 times higher than the blood, 3.2 times than the bone, and 2.8 times than the muscle. Therefore, it is indicated that the SAR differences between fat and other tissues (blood, bone, muscle) become smaller at high magnetic field than at low magnetic field. It is also demonstrated that some parts of human body with more fat, such as hip, abdomen, will have much higher SAR than others. The relationship of SAR between bone and muscle will become reversal when RF frequency is higher than 300MHz. This may be caused by faster increase of bone's conductivity when frequency increases [52]. As shown in Fig. 1.6, the fastest rate of SAR occurs when the resonant frequency increases from 15 to 85 MHz, especially for the tissue of human fat. So, it is preferable to transfer power at the frequencies lower than 15 MHz in biomedical applications.

SAR can be calculated by $SAR = \sigma |E|^2 / \rho$. Where σ is the tissue conductivity, and ρ is density, we consider the rat model made entirely out of brain tissue with $\sigma = 105 \text{ S/m}$ and $\rho = 1040 \text{ kg/m}^3$ in frequency of 13.56 MHz, which generates the worst case for SAR calculation. If we set the input power of 1 W, then, the maximum SAR value will be 0.15 W/kg. As mentioned before a SAR level of 1.6 W/kg has been designated as the limit of radio frequency energy that can be safely absorbed by humans. Therefore, the maximum allowable transmitted power can be found from $1 \text{ W} \times 1.6 \text{ (W/kg)} / 0.15 \text{ (W/kg)} = 10.7 \text{ W}$. It means that the maximum power at the output of the power amplifier used in TX side can be up to 10.7 W.

1.5 Objectives of This Thesis

The wirelessly-powered medical devices are widely employed for neural interfacing applications which should be verified by in-vivo experiment with the freely moving animal systems [9–13]. However, for such animal experiments, the use of cables for power transmission has limitations including 1) the area that the animal can move inside the experimental arena is limited to the length of the cable, 2) the weight and shear stress of the cable add to the abnormal conditions that the “freely” behaving animal would experience, and 3) no more than one animal can be tested due to the entanglement of the wires [13]. Addressing these issues is the motivation for designing a fully wireless animal experiment setup. There are two major challenges concerning to equip neural implantable devices to be fully wireless. This thesis addresses both challenges by providing high-performance inductive power link for a low power implantable device.

The big view of the project consists of implementing a multichannel neural recording system with a high-performance wireless interface for power and data transfer. My research focused on innovative techniques that decrease the power consumption of the circuit interface and improve the performance of the wireless power transfer system. Fig. 1.6(a) shows a block diagram of an implantable system, including the PC control unit, inductive power link, data transceiver link, and recording and stimula-

ting electrodes and analog front-end unit. Fig. 1.6(b) shows the schematic of the implanted side with more details, including the power receiver coil, antenna, integrated circuits, recording electrodes, and opto-stimulating electrodes.

Since this system will be used for the optogenetics application, the power consumption of the system will be one of the most significant challenges to overcome. Also, increasing the recording channels of the implantable device will increase the complexity and power consumption in the digital part of the system. Researchers have proven that neurons can be depolarized using light sensitive proteins such as *Chlamydomonas reinhardtii* Channelrhodopsin-2 (ChR2) or *Natronomonas pharaonis* halorhodopsin (NpHR) [36, 39]. Channelrhodopsin-2 (ChR2) can be excited by blue light (a wavelength of 470 nm) and induced polarization by admitting sodium [40]. Since this application requires blue light stimulation, the power consumption of the implanted device will need to be increased compared to electrical stimulator applications.

The challenges and requirements of the proposed systems in this thesis are presented below :

- Decrease the power consumption of the implantable circuit interface.
- Improve the performance of the wireless power transfer system to be used for the batteryless recording and stimulation systems in the long-term experiments.
- Reduce the size and weight of the receiver side of the inductive power link appropriate for the small animals like mouse and rat.

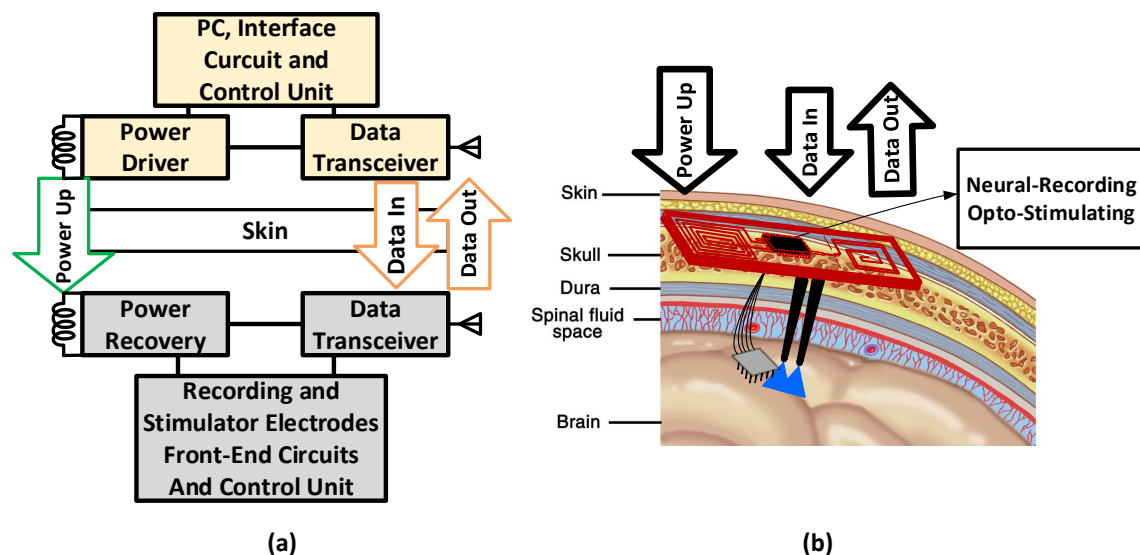


Figure 1.6 – (a)The block diagram of a wireless implantable system, (b) the schematic of implanted device of neural recording and Opto-stimulating system.

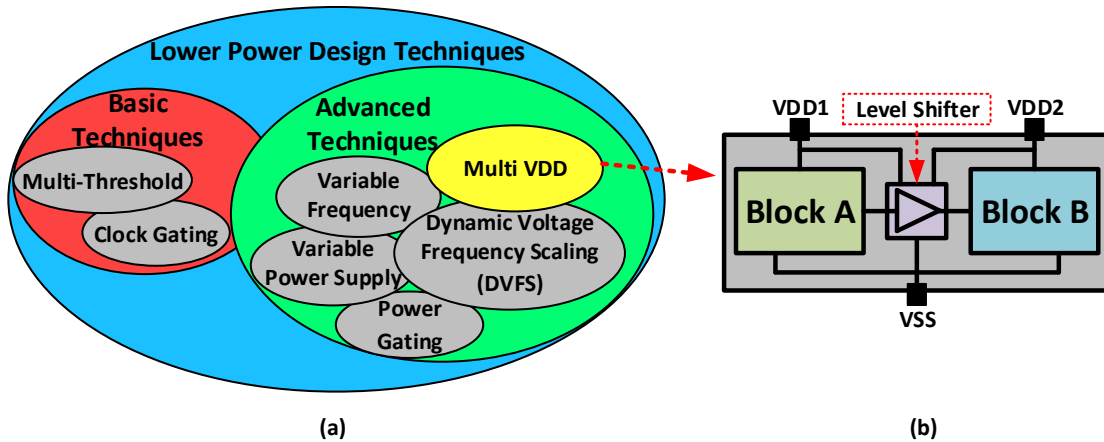


Figure 1.7 – (a) Challenges of high power consumption, (b) low power design techniques and, (c) multi power domain interface.

- Increase the separation distance between the transmitter and receiver coils while providing enough power for the fully wireless implantable device.
- Improve the localization and uniformity of the power transfer system all over the home-cage of the animal.
- Increase the reliability of the power transfer system against the angular misalignments for enabling uninterrupted optogenetic experiments with live laboratory rodents.

1.6 Low Power Design Techniques

Fig. 1.7(a) shows the different techniques used to design a lower power system. The basic techniques are a multi-threshold circuit and a clock gating. Multi-threshold circuits use low-threshold voltage transistors, which are fast and have high subthreshold leakage current, to implement the logic and also high-threshold transistors, which are slow and have low subthreshold leakage current, to use as sleep transistors. Clock gating is used to reduce dynamic power consumption and requires a clock tree to disable the circuitry. This means it does not have to switch states.

There are other advanced techniques of lower power designs that can reduce power dissipation. These techniques include variable frequency, variable power supply, power gating, dynamic voltage-frequency scaling (DVFS), and multi-VDD. Variable frequency allows some blocks to work inherently slower than other blocks while maintaining the same performance. Variable power supply allows the application to work with different power supplies during their activation time. Power gating allows specific blocks of the chip that might not be required to function to enter a low power mode like sleep, deep-sleep, or standby. DVFS which is a mixed technique of variable power supply and variable fre-

quency techniques. Multi VDD allows the designers to use different VDD for different blocks of the circuit.

Of the available techniques, the best and most adaptive to our application is multi VDD. We will need to use an interface circuit between two different blocks with different VDD to reduce the power consumption of the device (Fig. 1.7(b)). This circuit should be a voltage-level shifter to provide the voltage appropriate for the next block. The most critical considerations of level shifters are that the voltage swing should match both blocks, the propagation delay should be as little as possible so as not to reduce the speed and the dynamic power consumption should be as low as possible.

1.7 Inductive Power Link

Designing an efficient power transfer system depends on the transmitter and receiver coil size and the distance between them. Optimal size and distance depends on the target application. For example, in the design of a power pad, which powers up cell phones or tablets, the best distance between transmitter and receiver coils can be at least 10 times smaller than the receiver coil's diameter [53]. The flux density received by receiver coil depend on the receiver diameter. Obviously, if the diameter of the receiver coil reduced, it should be closer to the transmitter coil to receive more flux density. Therefore, the transmitter coil's diameter should be close to that of the receiver to achieve maximum power transfer efficiency [53]. Choosing a transmitter coil size that is too larger causes significant efficiency losses and unsuitable charging time.

An inductive power link is shown in Fig. 1.8(a). The main layout parameters of the square spiral coil are shown in Fig. 1.8(b), d_i , d_o and W are the inner diameter, the outer diameter, and the trace width, respectively. The minimum trace spacing (S) will be constrained by the PCB fabrication process due to the low operating frequency. The number of turns (n) is a function of the above parameters since, geometrically, $d_o = 2nW + (2n - 1)S + d_i$. The ratio between the magnetic flux generated by the current-carrying conductor and the current passing through it indicates its self-inductance. Several closed-form equations have been proposed to approximate L . We adopted 1.1 from [54] for square coils, shown in Fig. 1.8(b).

$$L = \frac{1.27 \cdot \mu_0 n^2 d_{avg}}{2} \left[\ln \left(\frac{2.07}{\phi} \right) + 0.18\phi + 0.13\phi^2 \right] \quad (1.1)$$

Where $\phi = (d_o - d_i)/(d_o + d_i)$, μ_0 is the permeability of space, n is the number of turns, $d_{avg} = (d_o + d_i)/2$, and ϕ is a parameter known as fill factor, which changes from 0 (when all the turns are concentrated on the perimeter, e.g. filament coils) to 1 (when the turns spiral all the way to the centre of the coil). To find the total parasitic dc resistance of the printed spiral coils (PSC), we need to know the length of the conductive trace (l_C), resistivity of the conductive material (ρ_C), and its thickness (t_C).

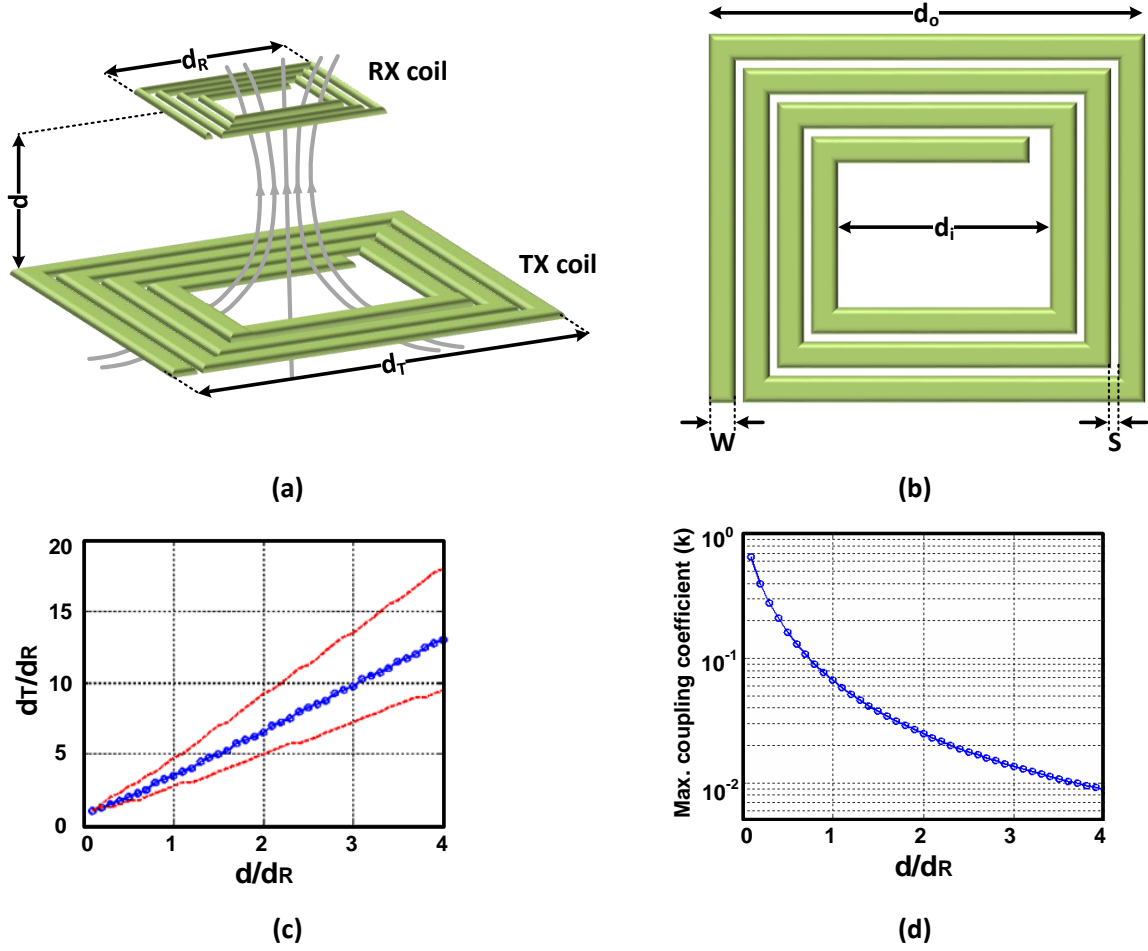


Figure 1.8 – (a) An inductive link between the TX and RX coils with a distance of d , (b) the geometrical parameters of a square-shaped printed spiral coil. (c) The ratio of the optimum diameter of TX [53] and (d) the maximum achievable coupling coefficient (k), as a function of the distance between TX and RX [53].

$$\begin{aligned}
 l_C &= 4.n.d_o - 4.n.W - (2n+1)^2 (S+W) \\
 R_{dc} &= \rho_C \frac{l_C}{W.t_C}
 \end{aligned} \tag{1.2}$$

Thus, the quality factor of the PSC without its parasitic capacitance can be found by substituting 1.1 and 1.2 in $Q = \omega L / R_{dc}$. The best value for S is the minimum trace spacing of the fabrication process (PCB fabricated coils). The choice of d_i for the transmitter is determined based on the distance between the transmitter and the receiver coils. The choice of d_o of the receiver, on the other hand, is based on a design trade-off between the implantable device and the required power transfer efficiency.

The impact of d_i on the quality factor and the coupling coefficient is less than that of d_o . Even though a small d_i typically leads to a better quality factor, a zero transmitter coil d_i is often not optimal [55]. The

turns of the coil near the centre d_o not contribute significantly to the inductance value even though it significantly increases the parasitic resistance. The optimum transmitter coil (d_T) values can be chosen with the curve illustrated in Fig. 1.8(c), which shows that as the distance between coils increases, the transmitter coil should be made larger to maintain efficiency. Similar to the receiver coil, the transmitter coil quality factor improves only by increasing its d_o . Unlike the receiver, however, the transmitter is stationary and does not have any particular size limitations.

The power transmission efficiency (η) of the inductive link shown in Fig. 1.8(a) can be written :

$$\eta = \frac{k^2 Q_T Q_R}{1 + k^2 Q_T Q_R} \quad (1.3)$$

where k is the coupling coefficient, $Q_T = \omega L_T / R_T$ and $Q_R = \omega L_R / R_R$. By maximizing both coil's quality factors, the most efficient power transfer is achieved. Since the Q factor has an inverse relation with the coil resistance, minimizing the resistive impedance of the coil in the chosen frequency will maximize the Q factor of the coil. The width and the distance between the traces and the thickness should be chosen respect to the size of the spiral coil to maximize the Q factor of the coil. The transmitter must be large enough to cover the entire area where the receiver could be located and to create the highest possible coupling coefficient (k) at the expected coil separation distance (d) in which d is already limited by k [56]. In a power-efficient design, the individual quality factor of each coil must be comparable to $1/k$ and the product of the two must be significantly larger than $1/k^2$ [57, 58]. The maximum value of the achievable k is shown in Fig. 1.8(d). Note that k drops off as $(d/d_R)^{3/2}$ if the coils are properly sized for each value of (d/d_R) . Therefore, the maximum achievable η given in 1.3 falls off as $(d/d_R)^3$ [53].

1.8 Review of Literature

Increasing power transfer efficiency (PTE) and the power delivered to the load (PDL) are essential milestones in the design of robust wireless power transmission (WPT) links intended for this application. Additional coils can be used between the transmitter and receiver coils as resonators to increase the coupling factor and extend the transmission distance. The design and optimization of 3-coil resonator links have been extensively covered. In [45] and [59], a 3-coil link and a 4-coil link were designed, as shown in Fig. 1.9(a) and Fig. 1.9(b), respectively. The 3-coil and 4-coil inductive links (depending on the application and the separation distance) achieved longer transmission distances than the 2-coil inductive link at maximum PTE and PDL.

To power up the target device over a large area, it is better to use several transmitter coils as an array structure to achieve the maximum level of PTE [60–63]. In this way, the transmitter should power up the only location of the receiver. Otherwise, the power efficiency significantly decreases. Different techniques have been suggested to increase the efficiency of the coil array. These techniques involve detecting the location of the receiver coil with a closed-loop system. These strategies increase the complexity of the system design [60].

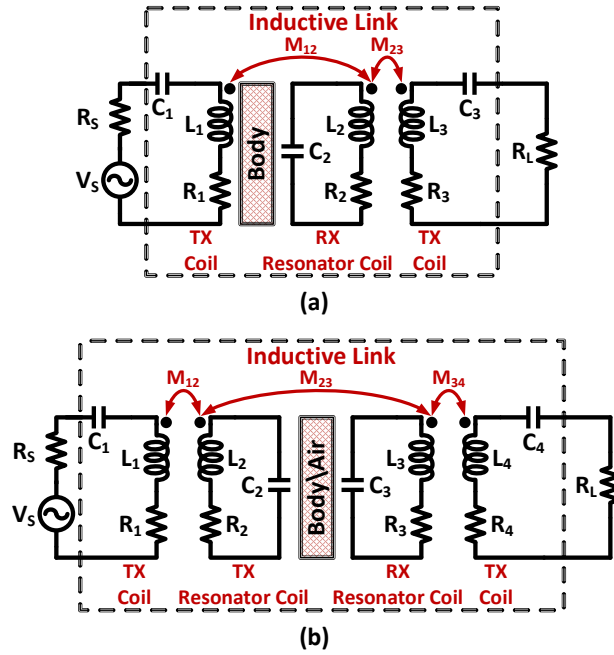


Figure 1.9 – Circuit models of (a) 3-coil inductive power link [45] and (b) 4-coil inductive link [59]

Different platforms are available for providing uniform WPT through different strategies and mechanisms. However, most solutions are barely suitable for use with standard home-cage products. In [64], such a platform is used to transfer data and power through a 4-coil link (Fig. 1.10). The power link can focus the transmitted power towards a moving receiver using a coil array and a closed-loop

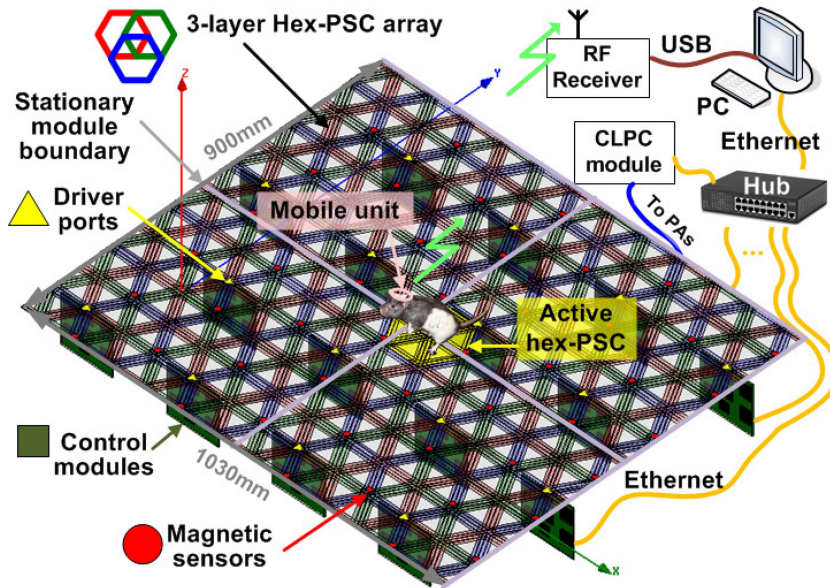


Figure 1.10 – Rendered view of the EnerCage system showing its modular architecture[64].

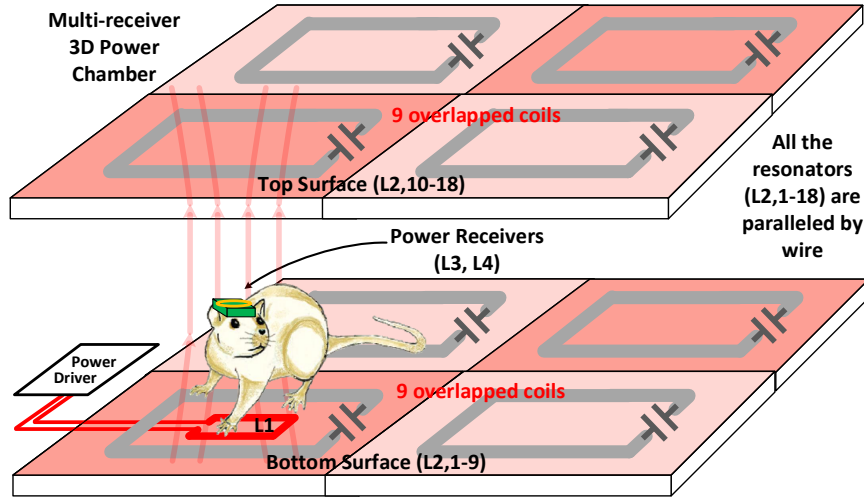


Figure 1.11 – 3D power transmitter made of several primary resonators (L2,1-L2,18) [48].

power control unit. This control unit tracks the location of the receiver in real-time using a small magnetic tracer placed in the body of the animal, which increases the complexity of the system to choose the proportion transmitter resonator transferring the power to the receiver coil. Other motion tracking systems have also been developed to track the position of an animal inside a home-cage in real-time [55,65,66].

A 3D power chamber based on a multi-coil link (Fig. 1.11) has been proposed by [48]. In this implementation, the transmitter resonator was made of several coils connected in parallel. This chamber provided power localization without any additional complex circuitry to locate the receiver. The multi-coil structure was based on a 4-coil inductive link whose primary resonator used a coil array composed of several identical coil elements connected in parallel instead of a single large coil, which is often found in conventional multi-coil links. In such a parallel arrangement, all the coils in the array have identical electromagnetic field patterns while only one has mutual inductance with the primary coil. Among other key advantages, such a structure enables building surfaces or chambers to deliver nearly constant power in 3D by leveraging ease of use and simplicity as well as higher PTE and PDL across longer separation distances.

Using a multi-coil inductive link has many benefits. First, it requires only a single primary coil. Second, it does not require calibration and tuning because it presents the same coupling for every pair of receiver coils and transmitter coils in the array. Third, it naturally localizes power towards the receiver using a limited number of primary coil elements. This saves energy and does not require complex detection circuitry to locate the receiver. Fourth, the size of the power surface can be scaled by changing n , the number of parallel coil elements in the primary resonance array. Fifth, it can easily switch from four-coil to three-coil topology through the removal of the secondary resonator on the receiver side in order to provide optimal PTE and PDL. This can be done for short and long-range power transmission

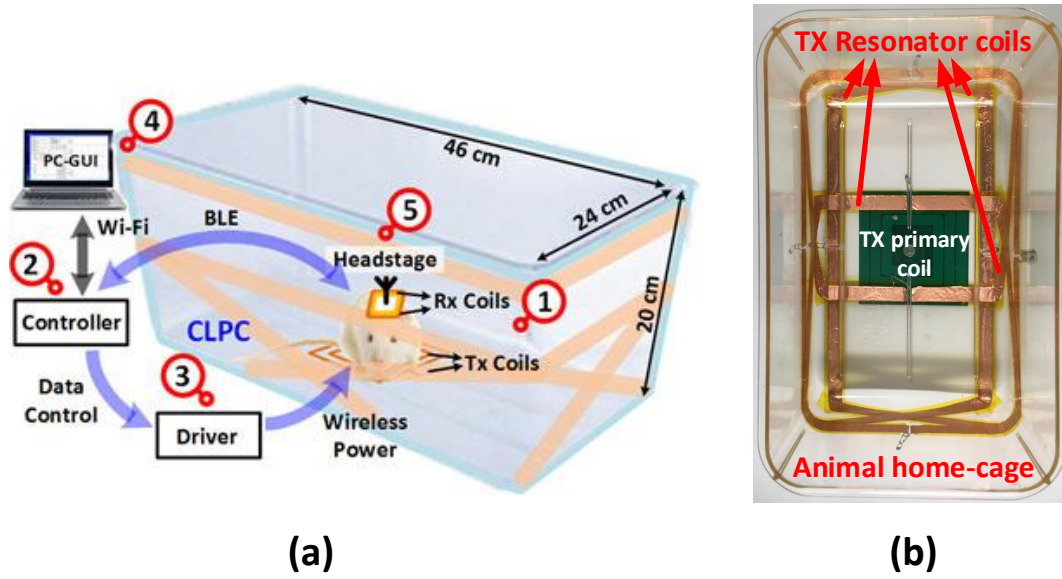


Figure 1.12 – (a) A conceptual representation of the proposed EnerCage-HC2 system for wireless powering and communication with a headstage [67]. (b) The implemented prototypes of power transmission systems scaled down for mouse application.

applications. These characteristics make multi-coil inductive links simpler, more efficient, and more cost effective than other solutions.

A 4-coil link WPT system built around a standard home-cage is presented in [67]. A conceptual representation of the proposed EnerCage-HC2 system is shown in Fig. 1.12(a). Copper foil is used to implement a resonator on the transmitter side. A magnetic resonant multi-coil design is used to localize the transmitted power from a single transmitter coil at the bottom of the cage toward the receiver. It achieves a separation distance of 0 cm to 17 cm with a maximum PTE of 51%, exhibiting a PTE drop in the middle of the home-cage. The WPT home-cage, shown in Fig. 1.12(b) is the scaled down strategy for the home-cage of the rat introduced in [67] to the home-cage of the mouse.

1.9 Contributions

My research focused on some innovative techniques to decrease the power consumption in the circuit interface and improve the performance of the wireless power transfer system. Since the wireless system would be used for optogenetics application, the power consumption of the system is one of the most significant challenges in wireless biomedical applications.

I worked toward decreasing the power consumption of the implantable system. I proposed a novel level shifter to separate the VDD of the digital and analog parts and to make it well-suited for low-power applications such as wireless sensor networks and IMDs. I published a paper titled “A Power-

Efficient Wide-Range Signal Level-Shifter” at the NEWCAS Conference in 2015. I designed the chip related to this proposed circuit, and I published an article titled “A High-Speed and Ultra-Low-Power Subthreshold Signal Level Shifter” in the journal of IEEE Transaction on Circuit and System-I, which is among the highest-level transactions in the electronic field.

I have worked on a WPT system to demonstrate a compatible system with different devices (implantable and headstages). During this time, I developed three different systems. The first used the overlapped coils for the animal home-cages to power up the implantable neural recording and stimulation system. This WPT system provided uniform power inside the home-cage using a 5-coil power link at the nominal distance of 5 cm (mouse application). A novel, double-sided coil was used as a receiver in this system. A paper related to this system, titled “A Wirelessly Powered High-Speed Transceiver for High-Density Bidirectional Neural Interfaces”, was published in the ISCAS Conference in 2017 as an invited paper.

The second WPT home-cage system I developed using a hybrid resonant link with a carrier frequency of 13.56 MHz. A parallel coil array was used as a primary transmitter coil to reduce the drop of PTE at the centre of the animal home-cage. Also, six coils, which were virtually in parallel, were used as the primary resonator to increase the PTE of the system. These two novel techniques improved the performance of the WPT system beyond available state-of-the-art systems. The results of this research were published in a paper titled “A Smart Neuroscience Platform with Wireless Power Transmission for Simultaneous Optogenetics and Electrophysiological Recording” in the ISCAS Conference in 2018 and had the honor of being published in a special edition of IEEE Transaction on Biomedical Circuits and Systems in 2018.

I developed a third system based on the second approach, and the article titled “A Wireless Neuroscience Platform for Uninterrupted Optogenetics and Electrophysiology Recording in Live Animals” has been submitted to a special edition of IEEE Transaction on Biomedical Circuits and Systems as an invited paper. In this system, the problem with the angular misalignment of the WPT home-cage was solved. Also, the performance of the system was demonstrated within an in-vivo experiment with a freely moving ChR2 mouse in the Quebec Mental Health Institute Research Center (CRIUSMQ). This was the first reported experiment that conducted simultaneous electrophysiological recording and optogenetic stimulation in a fully wireless and battery-less manner. The confirmed results show significant improvements in performance.

In short, all outcomes generated in the PhD were presented in *IEEE* transactions, journal articles, and conference proceedings. I was responsible for manuscript preparation, and I was the first author for all publications.

1.10 Thesis Outline

This thesis consists of two main parts of 1) low power design for the implantable devices in biomedical application, and 2) the wireless power transfer system for freely moving animal applications. In **Chapter 2** a new circuit is proposed to reduce the power consumption of the implantable devices for deep brain stimulation and recording applications. Also, three wireless power transfer systems for freely moving animal applications introduced in this thesis. The measurement results are reported for all these systems and the *in-vivo* measurement results of a simultaneous electrophysiological recording and optical stimulation for a freely moving animal is done for the last proposed system.

In **Chapter 2** of this thesis we propose a novel level shifter circuit converting subthreshold signal levels to super-threshold signal levels at high-speed using ultra low-power and a small silicon area, making it well-suited for low-power applications such as wireless sensor networks and implantable medical devices. The proposed circuit has been fabricated in 0.18- μm TSMC CMOS process, and the measurement results show that it significantly improves propagation delays with an acceptable power consumption compared to the other reported level shifters. It presents a transition delay of 29 ns for an input pulse signal of 0.4 V at a frequency of 500-kHz. In these typical conditions, the dynamic power consumption of the proposed circuit is of 61.5 nW, and the eic power dissipation is 330 pW, occupying only 229.5 μm^2 die area.

Chapter 3 devoted to a wirelessly powered, fully-integrated, low-power full-duplex transceiver to support high-density and bidirectional neural implants. The transmitter (TX) uses impulse radio ultra-wideband based on an edge combining approach, and the receiver (RX) uses a 2.4-GHz on-off keying narrow band topology. Our contributions are the following :

- Introduce a wireless power transfer system compatible with the commercial animal home-cage.
- propose a 5-coil inductive link using a double-sided implantable coil.
- Verifying the performance of WPT surface by measurement results.
- Powering up a fully integrated transceiver providing dual-band 500-Mbps TX uplink data rate and 100-Mbps RX downlink data rate.

In **Chapter 4** we introduce a new 3D WPT home-cage powering up : 1) a neural headstage including 1 optical-stimulation channel and 4 recording channels and, 2) an implantable device integrated in 0.18- μm TSMC CMOS process including 64 recording channels, 16 optical-stimulation channels, transceiver and, power management system. Our contributions are the following :

- Introducing a WPT home-cage to reduce the power efficiency drop inside the animal home-cage and providing a larger separation distance between TX and RX coils.
- Design and optimization of a receiver to power up the headstage implantable system.
- Designing a power management unit integrated in 0.18- μm TSMC CMOS process.

- Characterizing the functionality of both systems (discrete and integrated) powered up inside the WPT home-cage.

In **Chapter 5** we present the design implementation and experimental results regarding a 4-coil inductive link. Our contributions are the following :

- propose a new 4-coil inductive link can properly power up a headstage without interruption caused by the angular misalignment all over the animal home-cage.
- The 4-coil resonant link design procedure has been done to achieve optimum PTE.
- A motion tracking system can track and record the activity of the animal in real time for enabling simultaneous behavioural and physiological assessment.
- A comparison has been made by measuring the transmission coefficient of the system all over the WPT home-cage to show the performance of the introduced system compares to the state of the art.
- Simultaneous optogenetics and electrophysiological recording with a batteryless system are reported for the first time in a freely moving animal.
- Comparing the proposed idea with the previously published works by defining a figure of merit.

Finally, conclusions are drawn in **Chapter 6**, and some of the possible future research plans, based on the material developed in this dissertation will be suggested.

Chapitre 2

A High-Speed and Ultra Low-Power Subthreshold Signal Level Shifter

Résumé

Dans cet article, nous présentons un nouveau circuit de décalage de niveau convertissant des niveaux de signal subthreshold en niveaux de signaux superthreshold à haute vitesse, en utilisant ultra faible puissance et une petite zone de silicium, le rendant adapté pour les applications utilisant des réseaux à faible puissance et dispositifs médicaux implantables. Le circuit proposé introduit une nouvelle topologie de décaleur de niveau de tension utilisant un condensateur de décalage de niveau contribuant à augmenter la plage de tensions de conversion, tout en réduisant considérablement le retard de conversion. Un tel condensateur de décalage de niveau est rapidement chargé, chaque fois que le signal d'entrée détecte une transition de bas à haut, pour amplifier les noeuds de tension internes, et atteindre rapidement un niveau de tension de sortie élevé. Le circuit proposé atteint un délai de propagation plus court et une zone de silicium plus petite pour une fréquence de fonctionnement et une consommation d'énergie données, par rapport à d'autres solutions de circuit. Les résultats de mesure sont présentés pour le circuit proposé fabriqué dans une technologie CMOS TSMC de $0,18\text{-}\mu\text{m}$. Le circuit proposé peut convertir une large gamme de tensions d'entrée de 330 mV à 1,8 V et fonctionner sur une plage de fréquence de 100 Hz à 100 MHz. Il a un délai de propagation de 29 ns et une consommation d'énergie de 61,5 nW pour le signal d'entrée de 0,4 V, à une fréquence de 500 kHz, surpassant les conceptions précédentes.

Abstract

In this paper, we present a novel level shifter circuit converting subthreshold signal levels to super-threshold signal levels at high-speed using ultra low-power and a small silicon area, making it well-suited for low-power applications such as wireless sensor networks and implantable medical devices. The proposed circuit introduces a new voltage level shifter topology employing a level-shifting capacitor contributing to increases the range of conversion voltages, while significantly reducing the conversion delay. Such a level-shifting capacitor is quickly charged, whenever the input signal detects a low-to-high transition, to boost internal voltage nodes, and quickly reach a high output voltage level. The proposed circuit achieves a shorter propagation delay and a smaller silicon area for a given operating frequency and power consumption compared to other circuit solutions. Measurement results are presented for the proposed circuit fabricated in a 0.18- μm TSMC CMOS process. The proposed circuit can convert a wide range of the input voltages from 330 mV to 1.8 V, and operate over a frequency range of 100-Hz to 100-MHz. It has a propagation delay of 29 ns, and power consumption of 61.5 nW for the input signal of 0.4 V, at a frequency of 500-kHz, outperforming previous designs.

2.1 Introduction

One of the most efficient and direct ways to decrease the power consumption of digital integrated circuits and systems is to reduce their supply voltage [68]. As the complexity of systems on chips (SoCs) increases, subthreshold circuits, which use supply voltages lower than the threshold voltage of the MOSFET, have attracted much attention for use in several low-power applications, such as wireless sensor networks, miniature healthcare devices and environmental monitoring systems [69–75]. However, in addition to decreased power consumption, reducing the supply voltage also decreases circuit speed. One practical solution to this problem is to employ two or several supply voltages to cover different parts of the system, where the higher-voltage and lower-voltage supplies are used for circuits working at higher and lower speeds, respectively [76]. Therefore, level shifters (LS) providing wide voltage conversion ranges are needed to implement power domains working at different supply voltages and communicating with each other from inside these low-power SoCs. The propagation delay and the power consumption are two important characteristics of an LS. As the number of domains increases in a SoC, the number of required LS increases, and so does the delay and the power consumption associated with these level shifters, thus playing a key role on the overall system performance. Fig. 2.1 shows two types of conventional level shifters. Type I in Fig. 2.1(a) is based on a cross-coupled structure. In this circuit a low-supply signal V_{DDL} unbalances nodes Q and Q_b , and then the cross-coupled PMOS devices regeneratively increase the difference between Q and Q_b to reach V_{DDH} . Level conversion from V_{DDL} to V_{DDH} becomes more difficult as V_{DDL} gets smaller. The major drawback is the strong contention between the pull-up and pull-down network during switching. When IN and V_{DDL} are lowered to approximately one threshold voltage, the pull-down transis-

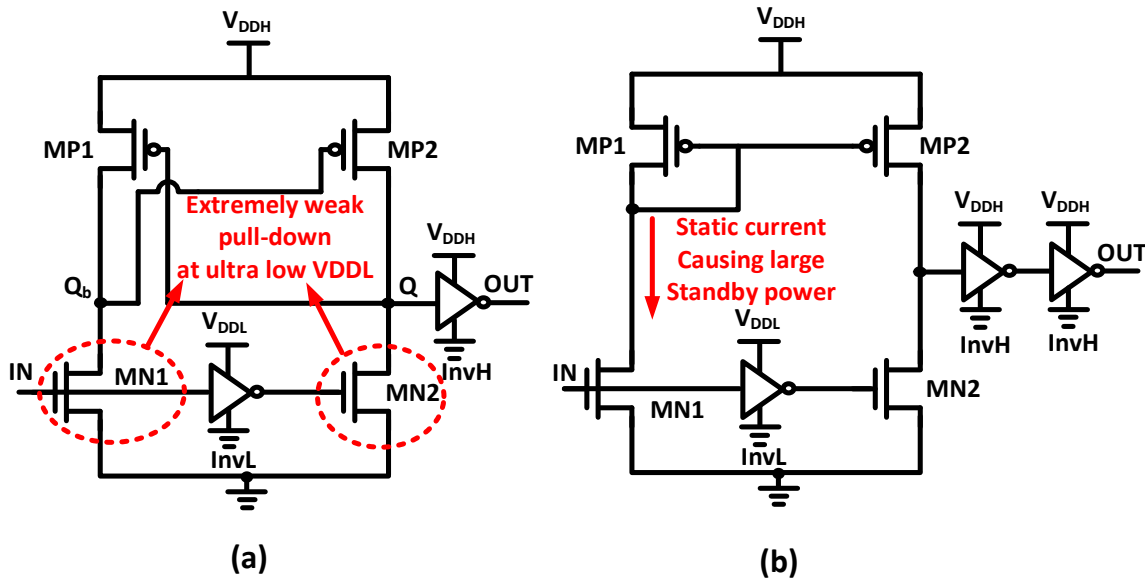


Figure 2.1 – Conventional level shifters based on : (a) cross-coupled structure, (b) current mirror structure

tors (MN1, MN2) extremely weak and cannot withstand the strength of the pull-up transistors (MP1, MP2) when V_{DDH} is in the super-threshold region. As a result, the output fails to flip. Solving this problem requires increasing the size of NMOS transistors, leading, however, to more power consumption and larger delays [77]. Type II level shifters (Fig. 2.1(b)) employ a current mirror structure to achieve fast level shifting for ultra-low input V_{DDL} and present small silicon die. The advantage of this type of topology is that it has low contention because there is almost no overlap between the pull-up and pull-down. However, a problem arises with the static current through MN1 and MP1, which causes large standby power [71]. In order to solve these problems, several LS circuits have been previously reported [70–75], [78–81]. An approach consisted in reducing the strength of the pull-up devices by limiting their currents [70], [79–82]. Other solutions propose multi-stage level shifters and feedback control to reduce the standby power which results in larger delays than with single-stage design [71–74]. Some of these reported level shifters have large areas and power overheads due to complex control mechanisms. For example, [82] uses a large number of transistors for weakening the pull-up path or for avoiding contention, while, substantial switching energy is consumed by the comparator in [70]. In this paper, a new level-shifting circuit based on a novel topology using a level-shifting capacitor approach is presented. In this new strategy, a capacitor is charged to supply a higher voltage at the gate of the higher supply voltage (V_{DDH}) inverter when needed, which enables covering a wider range of conversion voltages and higher operating frequencies, while achieving ultra-low power and shorter propagation delays. The design of the proposed LS is presented in Section 2.2. Implementation and post layout simulation of the circuit are shown in Section 2.3, Measurement results are given in Section 2.4, a discussion and a comparison are given in Section 2.5, and Section 2.6 concludes this paper.

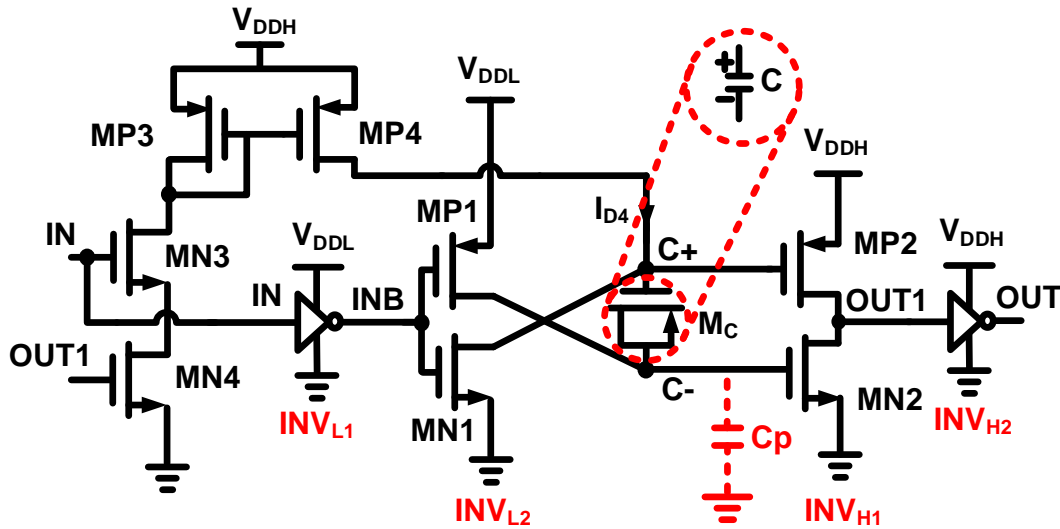


Figure 2.2 – The proposed level shifter circuit schematic based on a level-shifting capacitor.

2.2 Proposed LS Design

First, let us consider two cascaded inverters where one of them is supplied by V_{DDL} (INV_L) while the other is supplied by V_{DDH} (INV_H). In this case, if the first inverter drives the second inverter with a low voltage level (i.e., V_{DDL}), such value of V_{DDL} might not be large enough to turn off the PMOS transistor of the second inverter (INV_H which is supplied by V_{DDH}). We introduce the new LS circuit, the schematic of which is presented in Fig. 2.2, to alleviate this problem. Such new LS circuit uses a capacitor C connected between the gates of MP2 and MN2 that is charged by the voltage difference between V_{DDH} and V_{DDL} to shift the output voltage of the first stage upward during low-to-high transitions at node B . The current source I_{D4} (drain current of MP4) in Fig. 2.2 charges the capacitor C through PMOS switch MP1 up to " $V_{DDH} - V_{DDL}$ ". In this circuit, the current source is designed in such a way that it consumes the least power possible, by turning it off most of the time; it is only turned on during a low-to-high transition of the input signal "IN" (node A) and remains off otherwise. Another benefit of having this charged voltage on capacitor C is to provide a negative voltage when a "high"-level signal at node A tries to turn MN2 on and MP2 off. This negative voltage not only turns MN2 on more quickly but also reduces the static leakage current. Fig. 2.3 illustrates the operation of the circuit for two types of transitions of the input signal. The transistors that are in cut-off are greyed out in the figure. The proposed circuit operates as follows. Fig. 2.3(a), when a low-to-high transition occurs at the input and on node A, since node D had been high (before the low-to-high transition of the input), a current (I_{D3}) flows through the drains of MP3, MN3 and copied to MP4. This condition is illustrated Fig. 2.3(c). I_{D3} is mirrored by MP4, and I_{D4} charges capacitor C . At the same time, the bottom plate of capacitor C is connected to V_{DDL} through MP1 and charges capacitor C to $V_{DDH} - V_{DDL}$. Thus the top plate of the capacitor is charged to V_{DDH} . It is worth noting that capacitor C is completely charged after a single low-to-high transition. Finally, transistor MP2 is completely turned off due to the high voltage V_{DDH} at the top plate of the capacitor, while MN2 is also turned on because of the low voltage V_{DDL} at its gate. As node D is pulled down, MN4, and consequently the current source, is turned off. It is assumed that $V_C(0^-)$ is the voltage charged on the capacitor after the low-to-high transition of the input signal which is calculated using (2.1).

$$V_C(0^-) = V_{DDH} - V_{DDL} \quad (2.1)$$

Next, let's consider the case when a high-to-low transition occurs in the input signal IN (see Fig. 2.3(b)). In this condition, MP1 is turned off, and MN1 is turned on. Then, noting that the current source is off because MN4 is turned off by the low voltage level at D, it is observed that MN1 pulls down the upper plate of capacitor C , which causes a negative voltage on the gate of transistor MN2. Therefore, it turns off rapidly and node D quickly rises up to V_{DDH} through MP2 (see Fig. 2.3(c)). When MN1 is turned on, some of the charges of capacitor C is shared with the parasitic capacitor C_p , and hence,

$$V_C(0^+) = \frac{CV_C(0^-) - C_p V_{DDL}}{C + C_p} \quad (2.2)$$

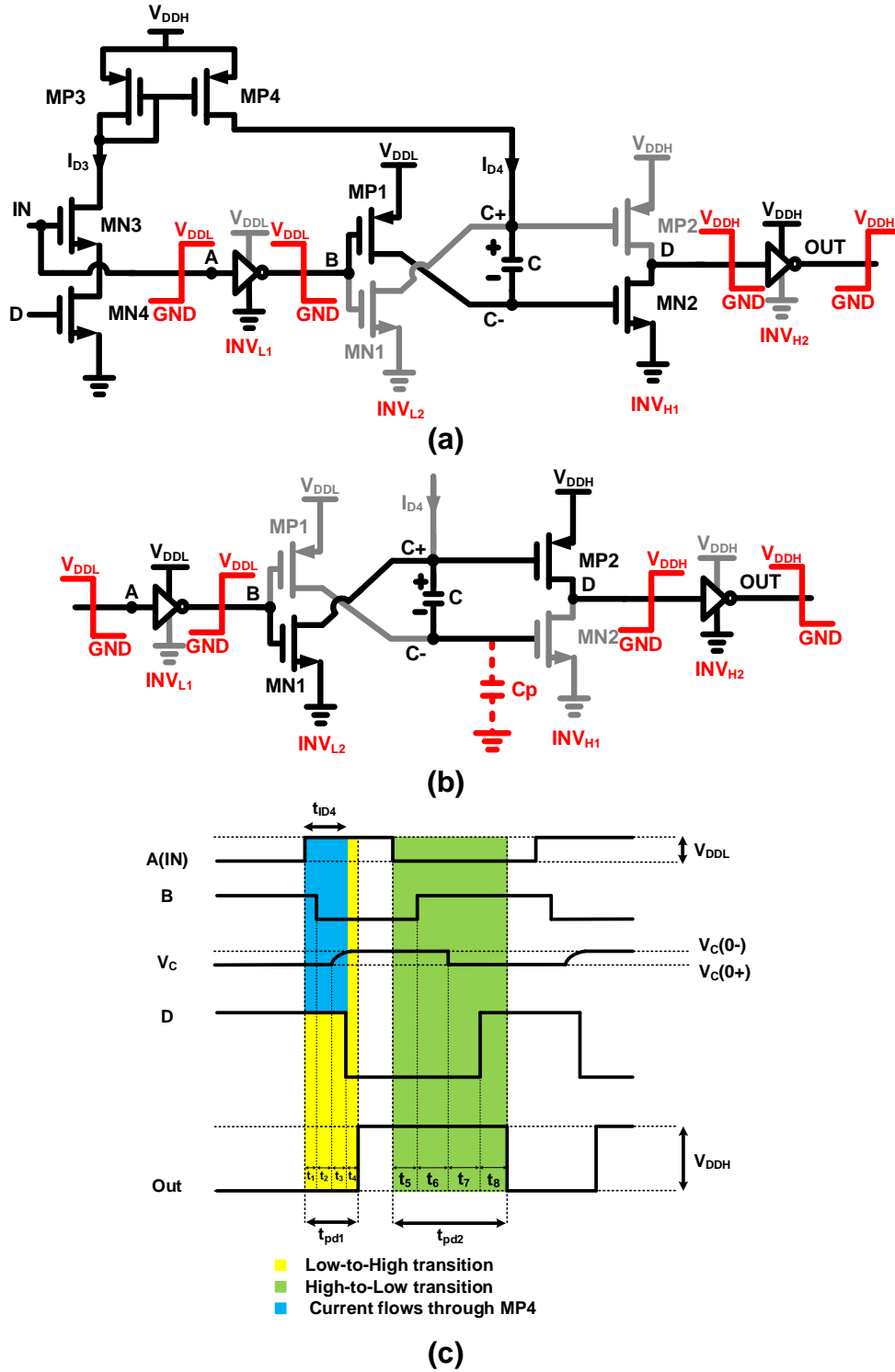


Figure 2.3 – Two operation cycles of the proposed LS circuit (a) low-to-high transition and (b) high-to-low transition of the input signal (c) time domain analysis for different nodes, from the input to the output, where t_{ID4} is the time interval during which the current source I_{D4} charges the capacitor C , while t_{pd1} and t_{pd2} are the propagation delays associated to low-to-high and high-to-low transitions, respectively.

where $V_C(0^+)$ is the voltage charged on the capacitor after a high-to-low transition of the input signal. This parasitic capacitor can be calculated as follows : $C_P = C_{GSN}^2 + C_{DSP1}$. Where C_{GSN} is the gate-source capacitance of MN2 and C_{DSP1} is the drain-source capacitors of MP1 [83]. Therefore, C needs to be recharged using the current source MP4 for every new conversion. The size of C can affect the power consumption of the circuit because of the charge-sharing effect between C and C_P , but this is not significant since C is charged only during the first transition. As can be seen in (2.2), capacitor C must be big enough so MN2 can be turned off and MP2 can be turned on after a high-to-low transition of the input signal “IN”. The value of the MOSCAP (MC) employed in this design is 880 fF, while the source of MC is connected to its drain, this capacitor is calculated using $C = C_{gmin-S} \times S + C_{gmin-Pj} \times Pj$, where C_{gmin} is a modeling parameter, S is the area of the active region of transistor MC, and Pj is the bulk junction bottom potential. Parameters S and Pj are obtained by $S=W \times L \times Mr$ and $Pj=2 \times W \times Mr$, respectively. Where W and L are the width and length of MC, respectively, and Mr is the number of gate fingers of MC. To decrease the power consumed by the current mirror made of MP3 and MP4 and to have a suitable current multiplication factor at the drain of MP4 of the current mirror, the W/L ratio of MP3 has to be smaller than the W/L ratio of MP4. The leakage discharge rate of C through MN2 and MP1 has no significant effect on the delay and the power consumption of proposed LS, since it is very small (on the order of a few 100 pW). While the value of C_P is roughly 2% of C , the charge leakage is limited and does not have a significant effect on the propagation delay [84]. The delay can be estimated by calculating the time constant formed by C and the total equivalent series resistance R_{eq} resulting from the drain-source resistances of MN1 and MP1. These transistors are operating in a subthreshold region when the input voltage “IN” is smaller than the threshold voltage of an NMOS transistor, and MP4, which is operating in strong inversion in the same condition, all connected to C . R_{eq} is obtained by (2.3).

$$R_{eq} = R_{dsP4} + R_{dsP1} \quad (2.3)$$

where R_{ds} is the on-resistance of the transistor in triode region [83]. Small R_{eq} values cause faster C discharging time, but results in longer recharging time, and thus, higher power consumption during the next transition. To prevent this effect, the width of MP1 and MP4 must be chosen small to increase the drain-source resistors. A larger W for MP4 can provide better delay performances but can increase the power consumption of the circuit at the same time. The optimum sizes of all transistors and capacitors (MOSCAP) are listed in Table 2.1. For a typical parasitic capacitor value of $C_P \approx 20$ fF, and due to the sizes of the transistors listed in Table 2.1 to calculate R_{eq} and knowing charge equation of capacitor :

$$V_C = V_C(0^-) e^{\frac{-t}{R_{eq}C}} \quad (2.4)$$

The recharging time of C is less than 2 ns which is smaller than the measured and the simulated delays of the proposed LS design. Thus, after one voltage conversion delay, C is fully charged and ready for the next transition. Of course, the circuit delay is also related to the speed of the inverters.

TABLE 2.1 – THE CIRCUIT ELEMENTS SIZES

NMOS Transistors	Value (W/L)	PMOS Transistors	Value (W/L)
MN1	$1\mu\text{m}/0.18\mu\text{m}$	MP1	$0.4\mu\text{m}/0.18\mu\text{m}$
MN2	$0.4\mu\text{m}/0.18\mu\text{m}$	MP2	$6\mu\text{m}/0.18\mu\text{m}$
MN3	$0.4\mu\text{m}/0.18\mu\text{m}$	MP3	$0.5\mu\text{m}/1\mu\text{m}$
MN4	$0.4\mu\text{m}/0.18\mu\text{m}$	MP4	$0.5\mu\text{m}/0.18\mu\text{m}$
MC (MOSCAP)		$8\mu\text{m}/1\mu\text{m}$ (880 fF)	

Fig. 2.3(c) shows the time domain analysis of low-to-high transition (t_{pd1}) and high-to-low transition (t_{pd2}) of the input signal and $t_{I_{D4}}$ is the time when the current source (I_{D4}) charges the capacitor C . In CMOS 180-nm, PMOS transistors have approximately three times the resistance values of NMOS transistors. Fig. 2.4 shows the equivalent RC circuit for the chain of inverters in the proposed LS. Thus, in INV_{L1} and INV_{H2} , the sizes of the PMOS are three times larger than the NMOS transistors in order to obtain the same resistance and mobility. Threshold voltages of NMOS and PMOS transistors in this technology are 0.42 V and 0.41 V respectively. Due to the sizes of the transistors for INV_{L2} and INV_{H1} , the values of the NMOS and PMOS resistors are different (see Fig. 2.4). R_1 , R_{MP1} , R_{MN2} and R_4 are the effective resistances of transistors in each inverter in Fig. 2.4(a)-(d), respectively. C_1 , C_2 , C_3 and C_4 are the diffusion capacitance between the drain and the body of each transistor of the inverters INV_{L1} , INV_{L2} , INV_{H1} and INV_{H2} , respectively. C_{p1} and C_{p2} shown in Fig. 2.4(b) are the capacitances seen at nodes C^- and C^+ , respectively, which are obtained as follows : $C_{p1} = C_{GSN2}$ and $C_{p2} = C_{GSP2} + C_{DSP4}$, Where C_{GSN2} and C_{GSP2} are the gate-source capacitors of MN2 and MP2 and C_{DSP4} is the drain-source capacitors of MP4. C_{G2} and C_{G4} illustrated in Fig. 2.4(a) and Fig. 2.4(c) are the gate capacitances of the transistors of INV_{L2} and INV_{H2} and C_{OUT} shown in Fig. 2.4(d) is the output capacitance of the proposed LS. Fig. 2.4 illustrates the circuit for a low-to-high transition with the switches showing

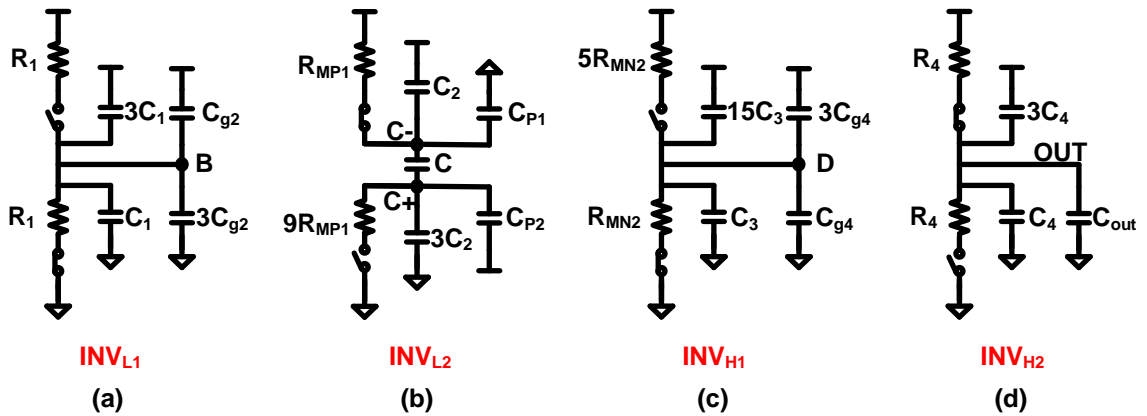


Figure 2.4 – Equivalent circuits of the inverter chain of the proposed LS.

which transistors of the inverters are on or off. R_1 and C_1 are assumed to be measured for a transistor with minimum length and minimum contact diffusion width. In the inverters, the propagation delay is defined as the time at which V_{OUT} of the inverter reaches $V_{DD}/2$ after a low-to-high transition, thus the delay of each inverter can be obtained by $t_{pd} = RC \times \ln(2)$ [84], where $\ln(2) = 0.69$. In the equivalent circuit of the proposed LS, C is large compared to the other capacitors. Therefore, it is negligible in the calculation of the propagation delay of the circuit. As illustrated in Fig. 2.3(c), the propagation delay during a low-to-high transition is obtained by :

$$\begin{aligned} t_{pd1} &= t_1 + t_2 + t_3 + t_4 \\ &= 0.69[(R_1 \times 6C_1) + (R_{MP1} \times 2C_2) + \\ &\quad (R_{MN2} \times 20C_3) + (R_4 \times 5C_4)] = 22.87R_1C_1 \end{aligned} \quad (2.5)$$

where t_1, t_2, t_3 and t_4 are the propagation delays of the $INV_{L1}, INV_{L2}, INV_{H1}$ and INV_{H2} , respectively, in a low-to-high transition of the input signal (see Fig. 2.3). For a high-to-low transition, the switches in Fig. 2.4 are inverted, and as shown in Fig. 2.3(c) the propagation delay is obtained by :

$$\begin{aligned} t_{pd2} &= t_5 + t_6 + t_7 + t_8 \\ &= 0.69[(R_1 \times 6C_1) + (9R_{MP1} \times 4C_2) + \\ &\quad (5R_{MN2} \times 20C_3) + (R_4 \times 5C_4)] = 101.89R_1C_1 \end{aligned} \quad (2.6)$$

where t_5, t_6, t_7 and t_8 are the propagation delays of the $INV_{L1}, INV_{L2}, INV_{H1}$ and INV_{H2} , respectively, in a high-to-low transition of the input signal (see Fig. 2.3). The delay is different for both types of transitions, and the total delay is approximated as an average of both of them. As shown in calculation of the delays, the propagation delay after a high-to-low transition is almost 4 times longer than the propagation delay after a low-to-high transition ($t_{pd2} \approx 4 t_{pd1}$). It will be shown in Section 2.4 that measurement results for the propagation delays are in excellent agreement with the calculations, as the propagation delay is almost four times longer for a high-to-low transition than for a low-to-high transition.

2.3 Implementation and Simulation Results

Post layout simulations are provided within a 0.18- μm TSMC CMOS technology. Fig. 2.5(a) and Fig. 2.5(b) depict the input and output signals, and the dynamic current of the current source I_{D4} , for $V_{DDL} = 0.4\text{V}$ and $V_{DDH} = 1.8\text{V}$. As it can be seen, the current source is turned on only when a high-to-low transition occurs in the input signal, and capacitor C is charged only under this condition. Capacitor C is implemented as a PMOSCAP with size of 8 $\mu\text{m}/180\text{ nm}$. In the proposed circuit, the Typical Case Corner (TCC) includes typical-NMOS and PMOS, $V_{DDH} = 1.8\text{V}$, and a temperature of 27°C. As shown in Section 2.2, transistor MN1 must be strong enough to pull-down the gate of MP2 after a high-to-low transition of the input signal. Furthermore, transistor MP1 must be strong enough to pull-up the gate of MN2 after a low-to-high transition of the input signal. Therefore, the corner including slow-NMOS and slow-PMOS is the worst corner for the delay. A decrease of V_{DDL} and an increase

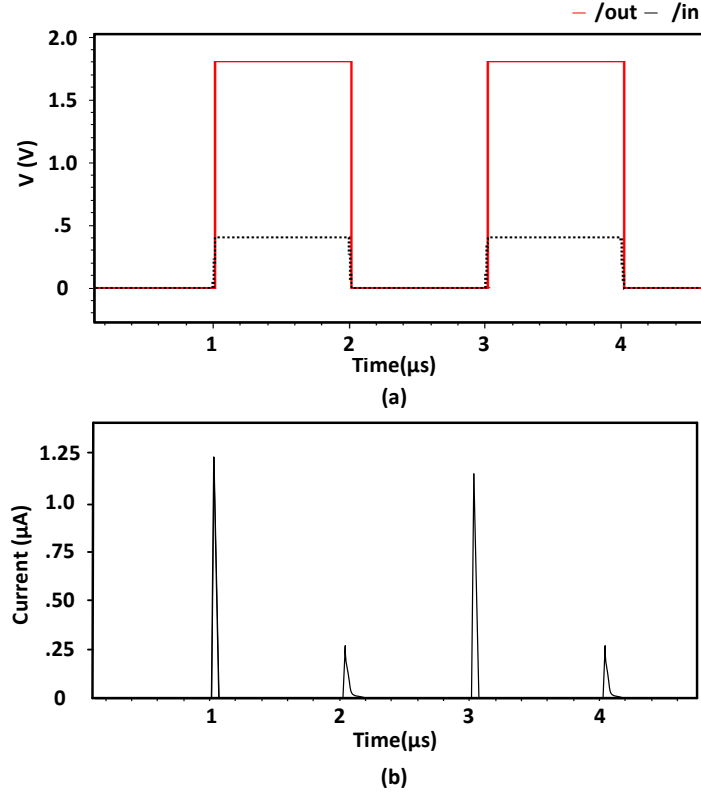


Figure 2.5 – Simulated waveforms of (a) the input and output voltages of the proposed circuit with $V_{DDL} = 0.4$ V and $V_{DDH} = 1.8$ V, (b) the current source of I_{D4} .

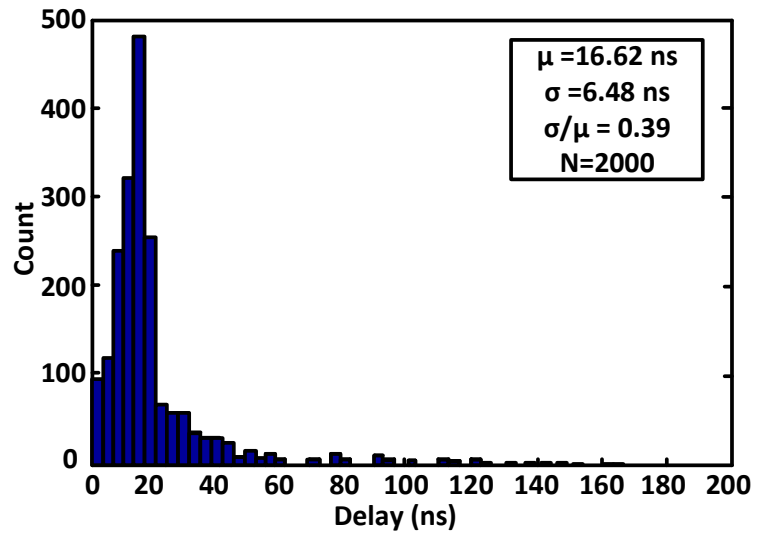
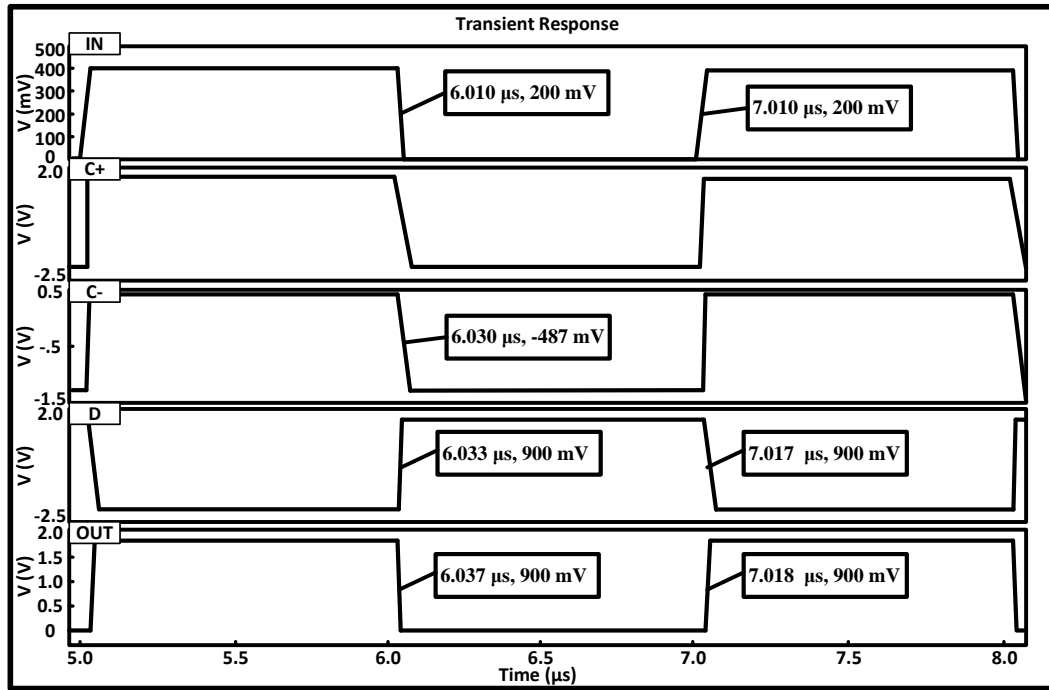
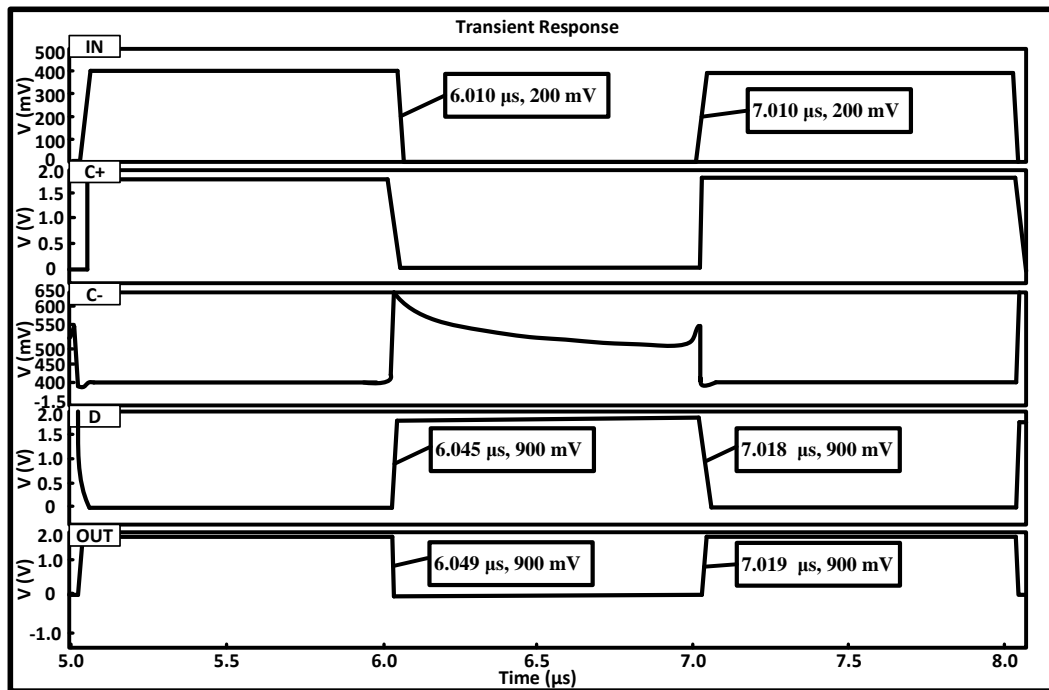


Figure 2.6 – Monte Carlo simulation results of the delay distribution for $V_{DDH} = 1.8$ V, $V_{DDL} = 0.4$ V and $T = 27^\circ\text{C}$.



(a)



(b)

Figure 2.7 – Transient response of the proposed circuit (a) with capacitor C , and (b) without capacitor C .

of V_{DDH} can further degrade the performance. Therefore, slow-NMOS, slow-PMOS, a negative low supply voltage variation of 10%, a positive high supply voltage of 10% and a temperature of -40°C are selected to illustrate the Worst Case Corner (WCC) conditions. Simulation results show that having fast-NMOS and slow-PMOS give the shortest delay. Inversely, fast-NMOS, slow-PMOS, positive low supply voltage variation of 10%, a negative high supply voltage of 10% and a temperature of 120°C are selected to illustrate the Best Case Corner (BCC). In order to show how process variations affect the characteristics of the proposed level-converter, a Monte Carlo simulations have been performed for a low supply voltage of $V_{DDL} = 0.4\text{V}$ and a high supply voltage of $V_{DDH} = 1.8\text{V}$.

Fig. 2.6 shows the results for the propagation delay, which has a log-normal distribution of variance 0.39. The mean delay is 16.62 ns, with standard deviation of 6.48 ns. The post-layout simulation results in Fig. 2.7 show the role of capacitor C to reduce the propagation delay of the proposed LS circuit. The transient response of nodes IN , D , OUT , $C+$ and $C-$ are shown with C (Fig. 2.7(a)) and without C (Fig. 2.7(b)). It can be seen in Fig. 2.7(a) that the rise time delay at node D is decreased by 12 ns when using capacitor C , which is providing a negative voltage of -487 mV at node $C-$, while a positive voltage appears at this node in Fig. 2.7(b) without using C . To show the correct operation of the proposed circuit across all PVT corners, the delay of the proposed circuit has been simulated at $V_{DDH} = 1.8\text{ V}$. Fig. 2.8 shows the variation of the delay of the proposed level shifter across all PVT corners. These results indicate that the worst case delay is two times higher than the best case delay at $V_{DDL}=0.4\text{V}$, while the circuit can still operate properly.

2.4 Measurement Results

The proposed LS is implemented in a $0.18\text{-}\mu\text{m}$ TSMC CMOS process. The chip micrograph and an enlarged view of the fabricated LS are shown in Fig. 2.9(a) and Fig. 2.9(b), respectively. The chip occupies only $229.5\text{ }\mu\text{m}^2$ ($17\text{ }\mu\text{m} \times 13.5\text{ }\mu\text{m}$) of silicon area (as shown in Fig. 2.9(c)). An inverter chain has been designed and implemented on the chip to buffer the output of the LS for driving the large capacitive load of the external testing equipment. In the proposed circuit, inverter INV_{L1} acts as an input buffer, so the proposed LS circuit does not need any additional input buffer when cascaded with other building blocks. The output load of the proposed LS consists of the gate capacitor of the first inverter of the output buffer. This capacitor includes an NMOS and a PMOS transistors of sizes of $(W/L)_N = 9\text{ }\mu\text{m}/0.18\text{ }\mu\text{m}$ and $(W/L)_P = 24\text{ }\mu\text{m}/0.18\text{ }\mu\text{m}$, respectively, which corresponds to a gate capacitor of around 10 fF in this process. The power consumption of the fabricated LS circuit was measured alone without the power of the output buffer and presented in Table 2.2. The delay of dummy buffer integrated on the same die under test was measured to be about 0.8 ns, the value of which is subtracted from the total measured LS propagation delay.

Fig. 2.10 shows a curve of the operating frequency as a function of V_{DDL} for different input voltages different input voltages between 0.33 V and 1 V. The area under the curve corresponds to the minimum voltage that can be converted by the proposed LS for a given frequency. Thus, it shows the maximum

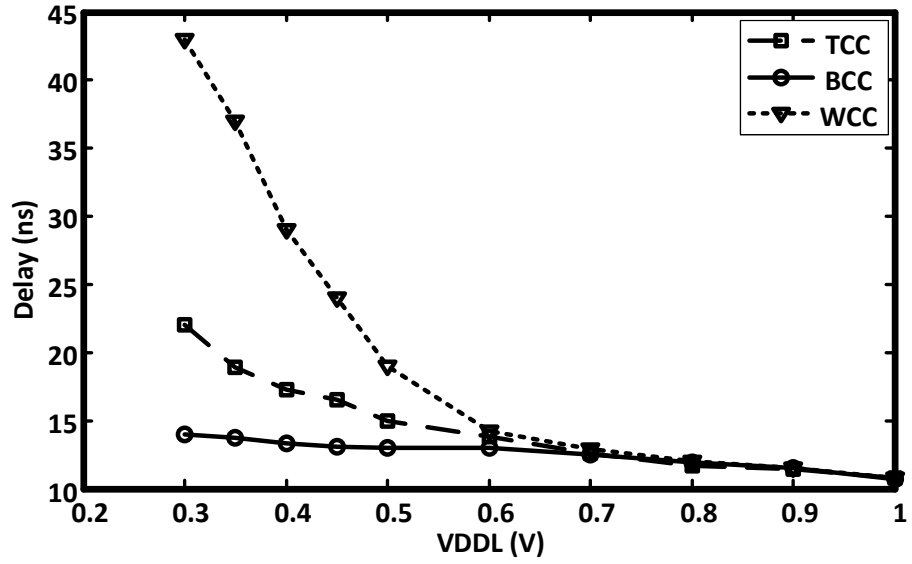


Figure 2.8 – The variation of the delay of the proposed circuit across PVT corners.

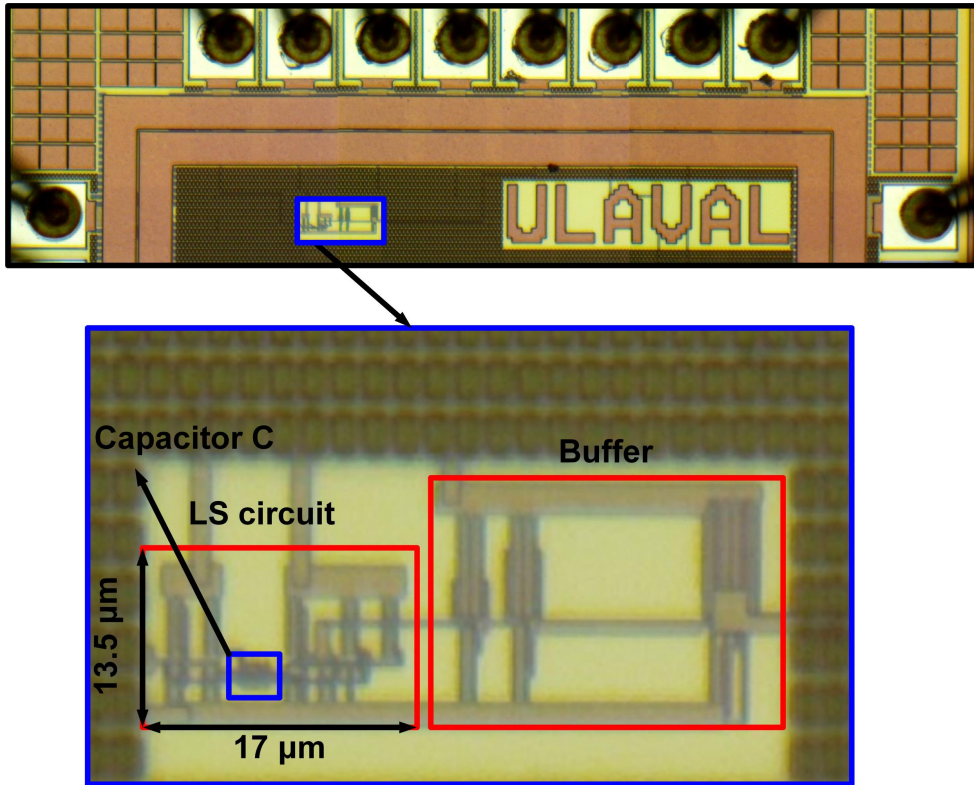


Figure 2.9 – (a) Chip micrograph, (b) partially enlarged view of the test circuit with output buffer and (c) chip view of the proposed LS (area : $229.5 \mu\text{m}^2$).

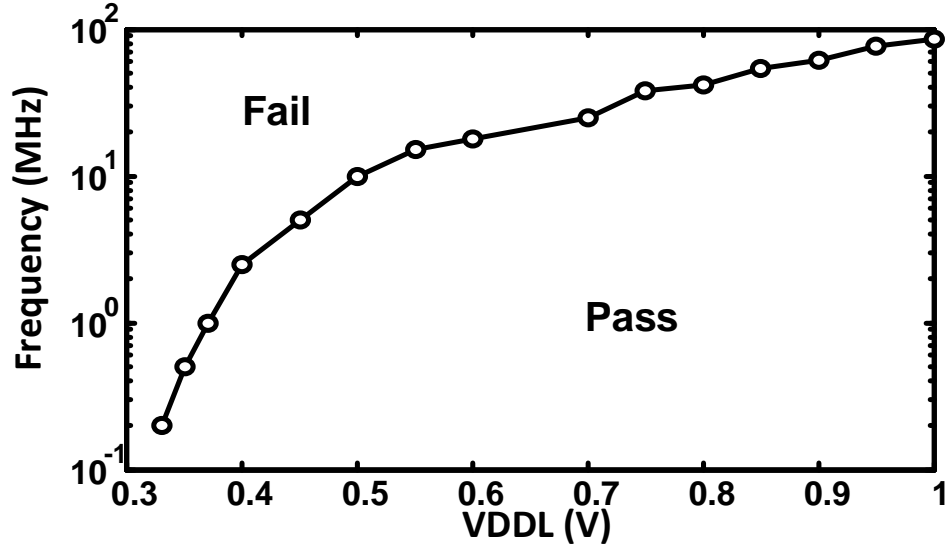


Figure 2.10 – Effect of V_{DDL} on the maximum operating frequency.

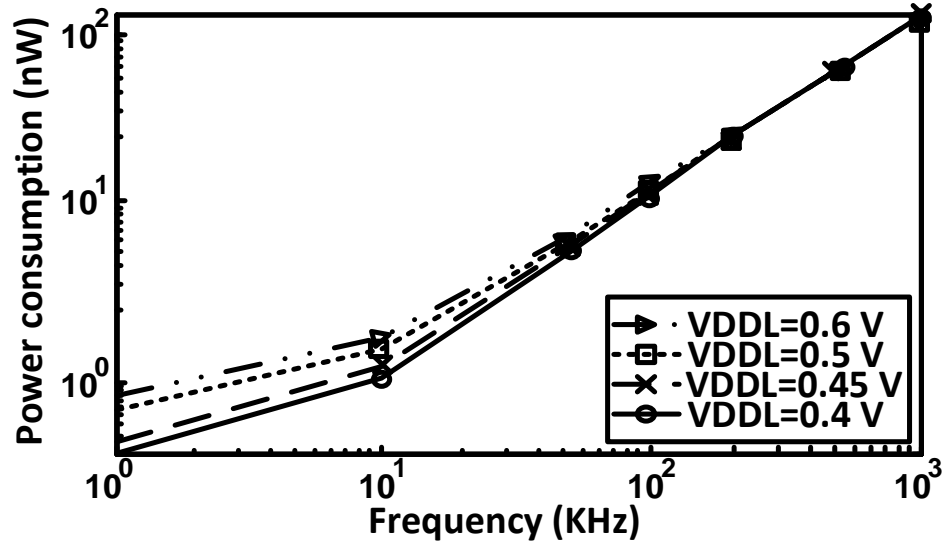


Figure 2.11 – Power consumption variation with frequency for different V_{DDL} .

frequency at which each V_{DDL} can be converted by the LS from a low level to a high level. The high-level voltage for this measurement is 1.8 V, and the minimum V_{DDL} that can be converted to 1.8 V is 0.33 V at a frequency of 200-KHz. Fig. 2.11 shows the measured power consumption as a function of input pulse frequency. In this figure, the power was measured for input pulse amplitudes of 0.4, 0.45, 0.5 and 0.6 V, and for a constant high-level output signal voltage of 1.8 V. As shown, the power consumption increases with the frequency of the input signal. In the case of a long-term standby input (≥ 1 s) $IN = GND$, causing node $B=V_{DDL}$, and MP1 to be turned off, node $C-$ can be gradually

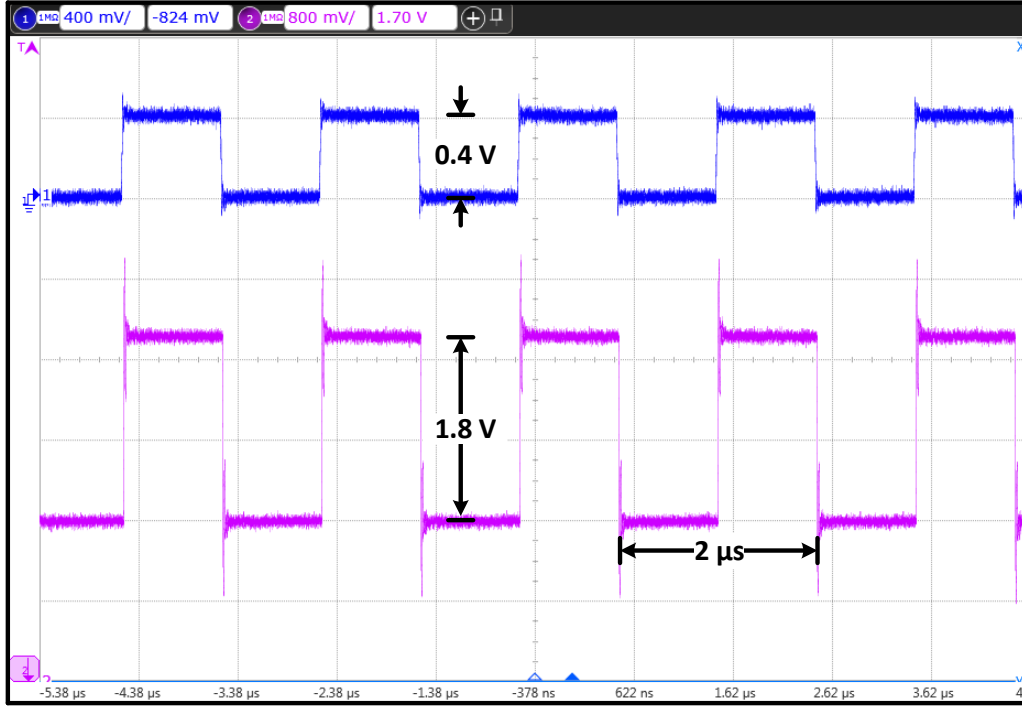
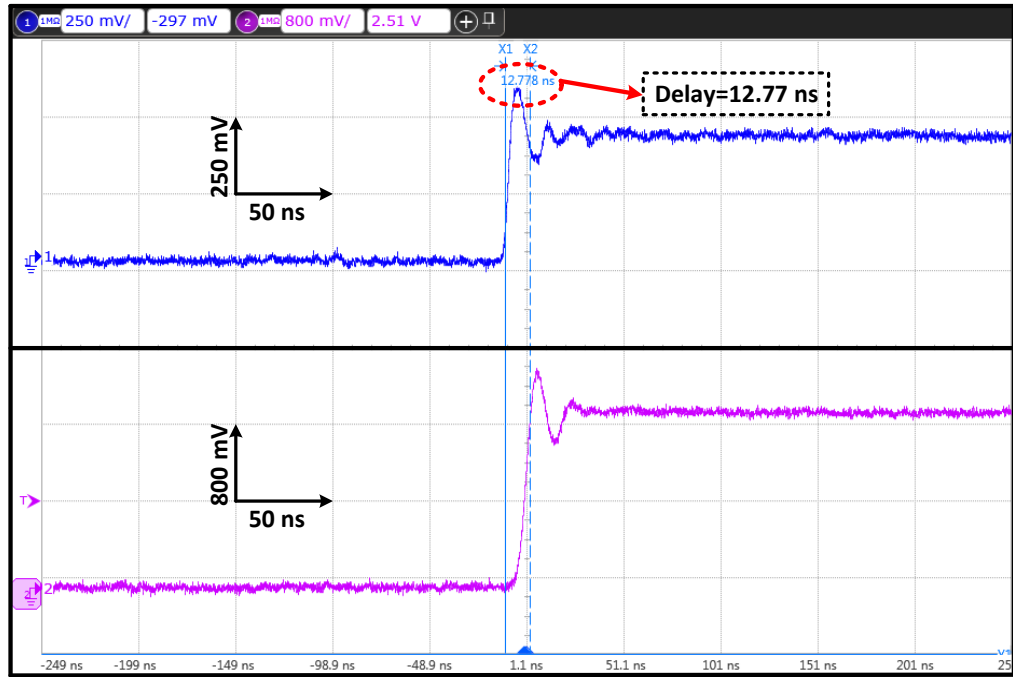
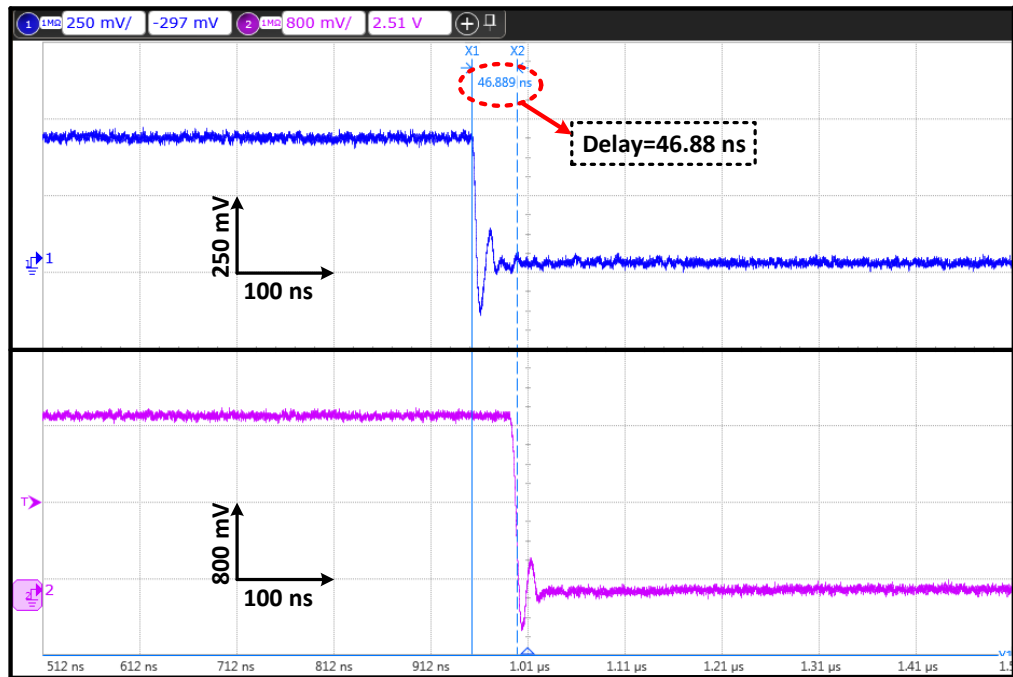


Figure 2.12 – Measured waveforms of the level shifter at 500-kHz input pulse with amplitude of 400 mVp-p to 1.8 Vp-p.

charged by a leakage current through MP1, and can eventually reach V_{th-MN2} , causing a quiescent current through MN2 once turned on. The estimated charging time of node C^- through MP1 to reach V_{th-MN2} is 1.1 s, which corresponds to a minimum operating frequency of 0.5-Hz. Thus, the circuit should not experience any quiescent current effect above this operating frequency. In order to expand the utilization of the proposed LS circuit to ultra-low frequency operation (≤ 0.5 -Hz) or to allow long standby input $IN = GND$ as well as higher V_{DDL} applications, a switch (an NMOS transistor) can be added between the drain of transistor MN2 and node D to break the leakage path between V_{DDL} and GND, thus avoiding any potential increase in power consumption due to a quiescent current. The measured input and output waveforms of the proposed LS circuit at 500-kHz are shown in Fig. 2.12. It shows the conversion of a 0.4 V signal to a 1.8 V signal. The measured propagation delay of the proposed LS for an input periodic pulse waveform at frequency of 500-kHz and a duty cycle of 50% is shown in Fig. 2.13. As illustrated in Fig. 2.13(a), the measured values of the rising transition delay is 12.77 ns whereas the measured value of the falling transition delay (Fig. 2.13(b)) is 46.88 ns. Thus, the measured average propagation delay value of the proposed LS for a transition in this situation is 29 ns.



(a)



(b)

Figure 2.13 – (a) Rise transition delay and (b) fall transition delay of the measured signal of the test chip at 500-kHz input pulse with amplitude of 400 mVp-p into 1.8 Vp-p.

2.5 Discussion and Comparison

To measure the minimum input supply voltage of the proposed LS circuit, we set V_{DDH} to 1.8 V at room temperature and measured the performance for an input signal given the following characteristics : 1 V down to 0 V at a frequency of 500-KHz. Fig. 2.14 shows the measured variation of the propagation delay and the power consumption of the circuit as a function of V_{DDL} within the acceptable input supply voltage range. In this figure, the power and the delay are measured for an input periodic pulse frequency of 500-kHz. As illustrated, the power consumption increases with V_{DDL} while the delay decreases with V_{DDL} . When V_{DDL} doubles, the delay and the power consumption are multiplied by a factor of 0.72 and 1.12, respectively. The largest value of the delay is 33.3 ns at an input signal voltage of 0.33 V. The variation of the delay and the power consumption for different V_{DDH} (1 V to 1.8 V) is shown in Fig. 2.15. For these measurements, the value of V_{DDL} and the frequency of the input pulses are set to 0.4 V and 500-kHz respectively. As can be observed, both the power consumption and the delay increase with V_{DDH} . In fact, when V_{DDH} doubles, the delay and the power consumption are multiplied by a factor of 1.7 and 2.2 respectively. Table 2.2 summarizes the measured performance of the proposed LS and compares it with the most relevant and recently reported LS designs. This comparison is based on measurement results. The proposed LS can convert a minimum V_{DDL} to V_{DDH} (1.8 V) of 0.33 V, which is a much higher operating frequency range than other solutions. The proposed LS also exhibits the smallest reported propagation delay, as can be seen in Table 2.2. The most important parameters to compare LS circuits are power consumption, operating frequency, and propagation delay.

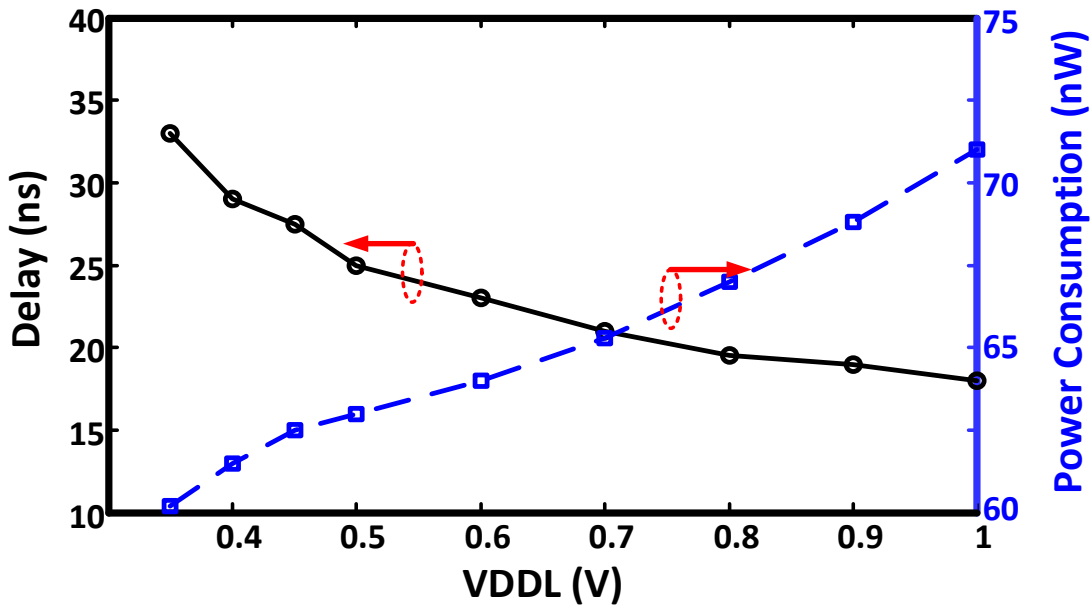


Figure 2.14 – Measured variation of the delay and power consumption for different V_{DDL} at $V_{DDH}=1.8$ V and 500-kHz.

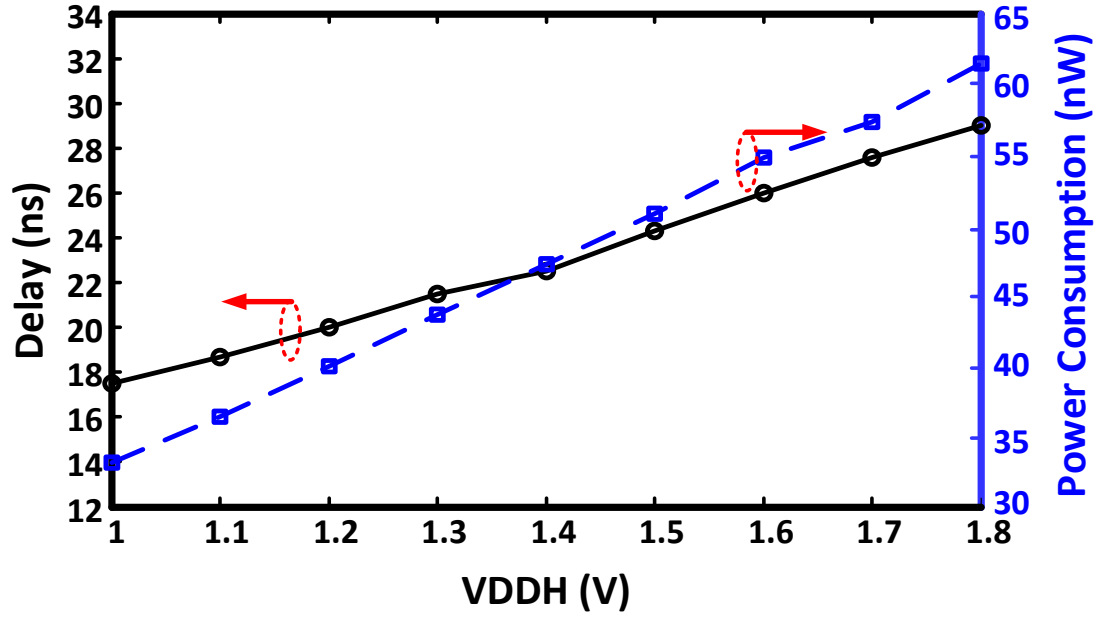


Figure 2.15 – Measured variation of the delay and power consumption for different V_{DDH} at $V_{DDL}=0.4$ V and 500-kHz.

It can be seen in Table 2.2 that the proposed LS has one of the smallest reported energy per transition (E_{tr}) as defined in [74], delay and static power (P_S) among recently published designs. The design in [72], which was fabricated in 65-nm CMOS process, presents the lowest E_{tr} and good delay, thanks to the availability of smaller transistors and lower parasitics in a more advanced process. However, this performance is achieved at the cost of a higher static power consumption of 2.5 nW, which is around eight times more than the 330 pW static power of our proposed design. This design also provides a lower conversion range of 0.3 V to 1.2 V, which is 40% lower than the range of 0.3 V to 1.8 V achieved by our design. Thanks to the pre-charged voltage on capacitor C , the speed of conversion is higher than other designs. Indeed, this charge of C contributes to turning MN2 on more quickly during a low-to-high transition (see Fig. 2.3(a)), which decreases the propagation delay. As shown in Table 2.2, the average propagation delay of the circuit within one transition is 29 ns at a frequency and input amplitude of 500-KHz and 0.4 V, respectively. Also, using capacitor C reduces the static current since the residual negative charge that remains on this capacitor after a low-to-high transition contributes to decreasing the propagation delay by providing the required voltage to turn MN2 off (see Fig. 2.3(b)). The measured power consumption that results from the static current in the circuit is as low as 330 pW, when converting a 0.4 V input signal to 1.8 V at a frequency of 500-KHz. Another advantage of the proposed approach comes from the fact that it turns off the bias circuit made of MN3, MN4, MP3, and MP4, during high-to-low transitions, which decreases further power consumption compared to conventional LS designs. Simulation results, illustrated in Table 2.2 for this circuit, also agree with measurement results.

TABLE 2.2 – MEASUREMENT COMPARISON TO THE FABRICATED LS DESIGNS

References	Tech. (nm)	Min. V_{DDL}	Delay (ns)	PS (nW)	Etr (fJ)	Result
[69]	65	0.4 V	15(0.4V→1.2V)	NA	375 (0.4V→1.2V@20KHz)	Meas.
[70]	350	0.23 V	100(0.4V→3V)	0.225(0.4V)	5800 (0.4V→3V@10KHz)	Meas.
[71]	180	0.21 V	167(0.4V→1.8V)	0.16(0.4V)	45 (0.4V→1.8V@100KHz)	Meas.
[72]	65	0.14 V	25(0.3V→1.2V)	2.5(0.3V)	30.7 (0.3V→1.2V@1MHz)	Meas.
[74]	130	0.3 V	58(0.3V→2.5V)	0.724(0.3V)	191 (0.3V→2.5V@5KHz)	Meas.
[79]	130	0.19 V	57.9(0.4V→1.2V)	NA	NA	Meas.
[82]	180	0.3 V	41.5(0.3V→2.5V)	0.475(0.3V)	229 (0.3V→2.5V@5KHz)	Meas.
[85]	130	0.1 V	31.7(0.4V→1.8V)	0.055(0.4V)	173 (0.4V→1.8V@100KHz)	Meas.
This work	180	0.3 V	17.3(0.4V→1.8V)	0.27(0.4V)	56 (0.4V→1.8V@500KHz)	Sim.
This work	180	0.33 V	29(0.4V→1.8V)	0.33(0.4V)	61.5 (0.4V→1.8V@500KHz)	Meas.

2.6 Conclusion

A fast and ultra-low power level-converting circuit that employs a new topology based on a level-shifting capacitor has been introduced. The novelty of this circuit resides in embedding a capacitor between the gates of transistors in the inverter INV_{H1} , to increase the voltage conversion range as well as to reduce the delay time of the circuit by enabling faster conversion to the higher supply voltage (V_{DDH}). This circuit presents a wide range of operating frequencies, and a wide range of convertible voltages thanks to the new voltage level shifter topology based on a level-shifting capacitor. In particular, this proposed approach achieves ultra low-power and high conversion speed. The proposed circuit has been fabricated in 0.18- μm TSMC CMOS process, and the measurement results show that it significantly improves propagation delays with an acceptable power consumption compared to the other reported level shifters. It presents a transition delay of 29 ns for an input pulse signal of 0.4 V at a frequency of 500-kHz. In these typical conditions, the dynamic power consumption of the proposed circuit is of 61.5 nW, and the static power dissipation is 330 pW, occupying only 229.5 μm^2 die area.

Chapitre 3

A Wirelessly Powered High-Speed Transceiver for High-Density Bidirectional Neural Interfaces

Résumé

Cet article présente un émetteur-récepteur full-duplex de faible puissance entièrement intégré et sans fil pour supporter des implants neuronaux à haute densité et bidirectionnels. L'émetteur (TX) utilise une bande radio à impulsions ultra-larges basée sur une approche de combinaison de fronts, et le récepteur (RX) utilise une topologie à bande étroite à incrémentation de 2,4 GHz. L'émetteur-récepteur proposé fournit un débit de données de liaison montante TX à 500 Mbits/s et un débit de données descendantes RX à 100 Mbits/s, et il est entièrement intégré dans un processus CMOS TSMC 0,18- μm d'une taille totale de 0,8 mm^2 . La consommation d'énergie totale mesurée est de 10,4 mW en mode duplex intégral (5 mW à 100 Mbps pour RX et 5,4 mW à 800 Mbits/s ou 6,7 pJ/bit pour TX). L'émetteur-récepteur est alimenté sans fil par un système de cage domestique intelligent basé sur des réseaux multi-bobines superposés à travers un mince récepteur multi-bobine implantable de taille 1×1 cm^2 , implanté sous d'une souris de laboratoire, et muni circuits intégrés de gestion de l'énergie. Ce système inductif est conçu pour fournir jusqu'à 35,5 mW de puissance délivrée à la charge à partir d'un signal porteur de 13,56 MHz avec une efficacité globale de transfert de puissance supérieure à 5 % sur une distance de séparation de 3 cm à 5 cm.

Abstract

This paper presents a wirelessly powered, fully-integrated, low-power full-duplex transceiver to support high-density and bidirectional neural implants. The transmitter (TX) uses impulse radio ultra-wideband based on an edge combining approach, and the receiver (RX) uses a 2.4-GHz on-off keying narrow band topology. The proposed transceiver provides dual-band 500-Mbps TX uplink data rate and 100-Mbps RX downlink data rate, and it is fully integrated into standard 0.18- μm TSMC CMOS process within a total size of 0.8 mm^2 . The total measured power consumption is 10.4 mW in full duplex mode (5 mW at 100-Mbps for RX, and 5.4 mW at 800-Mbps or 6.7 pJ/bit for TX). The transceiver is wirelessly powered up by a smart home-cage system based on overlapped multi-coil arrays through a thin implantable multi-coil receiver of $1 \times 1 \text{ cm}^2$ of size, implanted below the scalp of a laboratory mouse, and integrated power management circuits. This inductive system is designed to deliver up to 35.5 mW of power delivered to the load from a 13.56-MHz carrier signal with an overall power transfer efficiency above 5% across a separation distance ranging from 3 cm to 5 cm.

3.1 Introduction

Currently, there is a high demand for miniature implantable integrated microsystems to study the brain microcircuits of freely moving laboratory mouse [86–88]. Such devices can interface with the central nervous system in both electrical and optical paradigms for stimulating and monitoring neural circuits, which is critical to discover new drugs and therapeutics against neurological disorders like epilepsy, depression, and Parkinson’s disease [50, 59, 64, 65, 89].

Recently, different implantable neural recording and stimulating devices have been developed to provide Brain Machine Interfaces (BMI) with a suitable wireless connection [90]. These devices have not yet transitioned from research to commercial systems as they struggle to maintain small size and low-power consumption while reaching high wireless data rates for supporting the bidirectional transmission of high-density neural recording/stimulation data. These chronic implants must handle a very high number of recording/stimulation channels (up to several hundred), and this number is continually growing as new microprobes of increasing complexity become available.

Conventionally, separated data transmission links have been used for forwarding and backward telemetry in such implantable systems. On the other hand, using a battery as a power source is not practical since it increases the size and weight (especially at the research uses for mouse), and has a limited lifetime, which prevents chronic implantation. This has created a high demand for high-efficiency wireless power transmission systems. Previously, inductive power links have been utilized either for implementing forward or backward telemetry or for combining both into the same link, providing data rates on the order of a few mega bit-per-seconds [89]. Such strategies are prone to increased complexity and interference because of the mutual inductance with the power link. Moreover, having three separate (independent) links complicates miniaturization of the implantable devices [91]. Wireless power links based on inductively coupled coils have been previously demonstrated in [59] and [92]. Such links operate at frequencies limited to a few megahertz to avoid significant absorption in biological tissues. The power transfer efficiency obtained with an inductive link strongly depends on the geometry of the coils, the separation distance between the transmitter (TX) and the receiver (RX), and their orientation (angular alignment). Inductive approaches to transmit power above a surface for providing an implanted receiver with free positioning have been previously developed [88], [89] and [59].

The paper is organized as follow : **Section 3.2** presents an overview of the proposed power and data transmission interface. **Section 3.3** presents the implementation and the measured performance of the wireless power inductive link. **Section 3.4** presents the measured performance of the full-duplex transceiver while it is wirelessly powered by the wireless power transmission system and the integrated power management unit. Finally, conclusions are drawn in **Section 3.5**.

3.2 System Overview

Implantable neural recording and stimulating systems often need to receive configuration data or stimulation patterns data while collecting neural activity from several channels in parallel. Thus, a full-duplex data communication topology is highly sought after for this application. Considering the limited power budget of the implantable system, the receiver and the transmitter of such full-duplex transceiver must be ultra-low power.

As illustrated in Fig. 3.1, the proposed implantable system includes a wireless System on Chip (SoC) providing high-rate bidirectional data transmission for transmitting neural data and receiving control commands, a power recovery/management unit for powering up the whole implant, a low-power microcontroller unit (MCU) for controlling the SoC, and a wireless power link operating at low-frequency for powering up the implanted system with minimal absorption into biological tissues. The proposed full-duplex bidirectional RF data transceiver provides both forward and backward data transmission within the 2.4-GHz ISM band and the UWB 3.1- to 7-GHz band [91], respectively. Both the transmitter (TX) and the receiver share a single wideband implantable antenna, enabling a smaller implantable system overall. The inductive power link allows to wirelessly power up the proposed implantable system through a small receiver (RX) coil of $1 \times 1 \text{ cm}^2$ of size. The on-chip power recovery/management unit includes a rectifier and a Low-Dropout (LDO) regulator circuits which allow

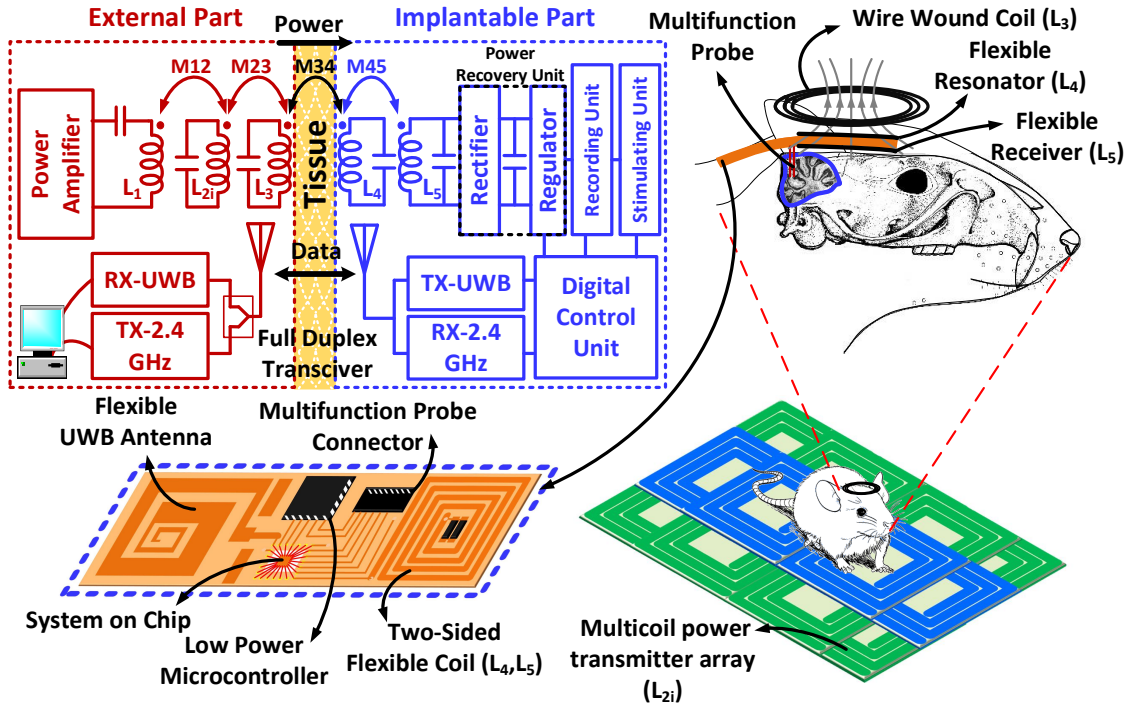


Figure 3.1 – The proposed implantable neural recording and stimulating brain machine interface including an inductive power link and a CMOS system on a chip including power recovery circuits and a full-duplex transceiver.

to extract and convert a 13.56-MHz power carrier to the regulated voltage of 1.8 V and 1.2 V for powering up the TX and RX, respectively.

The proposed interface uses an advanced version of the full-duplex integrated transceiver introduced in [91], which is provided with a new short-impulse radio BPSK modulation scheme, using short 500-ps pulses to encode the data [93]. For the receiver, an OOK modulation scheme was deemed the best choice regarding area and power consumption. The proposed transmitter consumes 5.4 mW at a data rate of 800 Mbps using short impulses having a bandwidth of 3-GHz, ranging from 2.6-GHz to 5.6-GHz, while the 2.4-GHz receiver consumes 5 mW at a data rate of 100-Mbps. As shown in Fig. 3.1, a new 5-coil inductive power link using an array topology is utilized for powering up the proposed implantable system with a thin flexible implanted receiver coil. The topology of which provides high-efficiency for separation distances of 3 cm to 5 cm, across the air and skin, between the implanted system and an external controller [59]. In this link, a primary coil (L_1), a multi-coil array (L_{2i}) and a resonator coil (L_3) are located outside the body, while a thin double-sided coil including a flexible resonator coil (L_4) and a receiver coil (L_5), is implanted inside the body. The equivalent circuit model of the proposed inductive link and a block diagram of the integrated power recovery/management unit, are presented in Fig. 3.1.

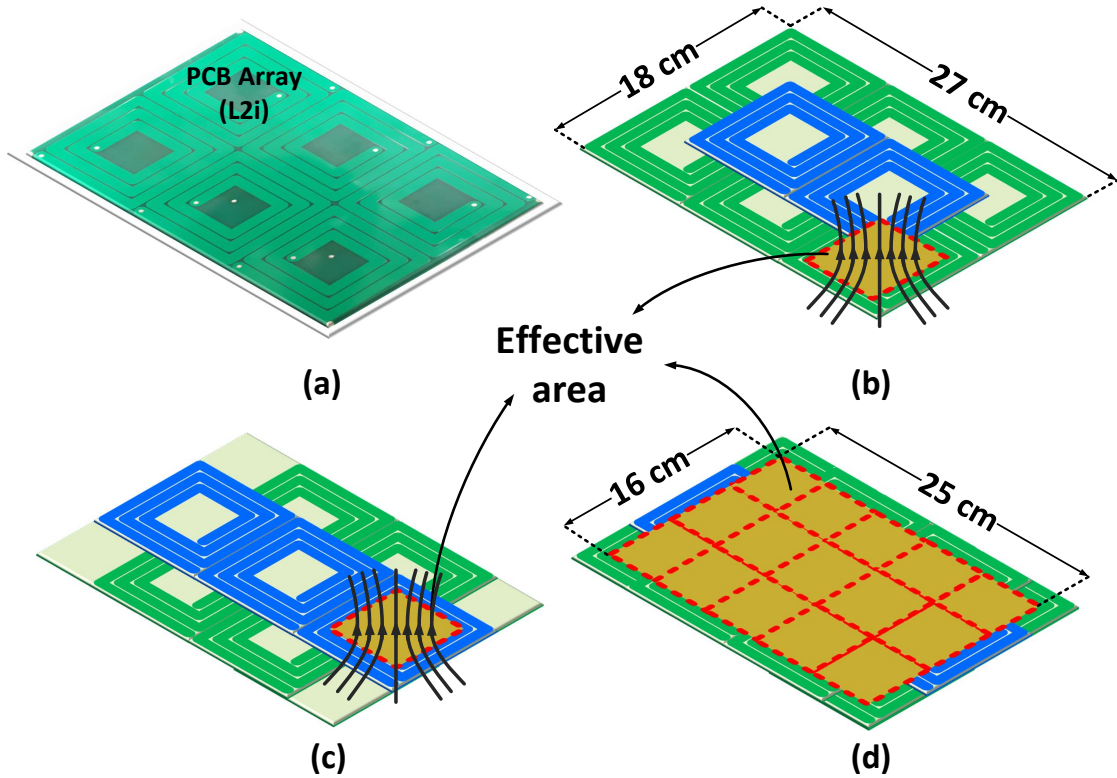


Figure 3.2 – (a) Fabricated multi-coil array including two 50%-overlapping FR4 layers. (b) The top FR4 layer of the inductive array (c) the bottom FR4 layer of the inductive array (d) the two FR4 layers are superimposed (a+b) for implementing a surface providing uniform power transmission density.

3.3 Inductive Power Transmission System Design

Designing a power transmitter coil array providing high power efficiency with a small and remote receiver is challenging since the transmitted power must be localized toward the receiver to reduce losses. A parallel resonator array featuring a natural power localization mechanism has been previously developed by our team [92].

In this system (Fig. 3.1), three resonator coils are focalizing the electromagnetic field produced by the primary coil toward the implanted receiver coil, which greatly improves the Power Transfer Efficiency (PTE) and the Power Delivered to the Load (PDL) of the wireless power link. As shown in Fig. 3.2, the proposed power surface prototype includes 15 overlapped primary resonator coil elements (L_{2i}) equally separated, and located below a home-cage. These resonators are all connected in parallel with wires, like in [92]. The resonance frequency of the primary and secondary resonators is tuned to 13.56-

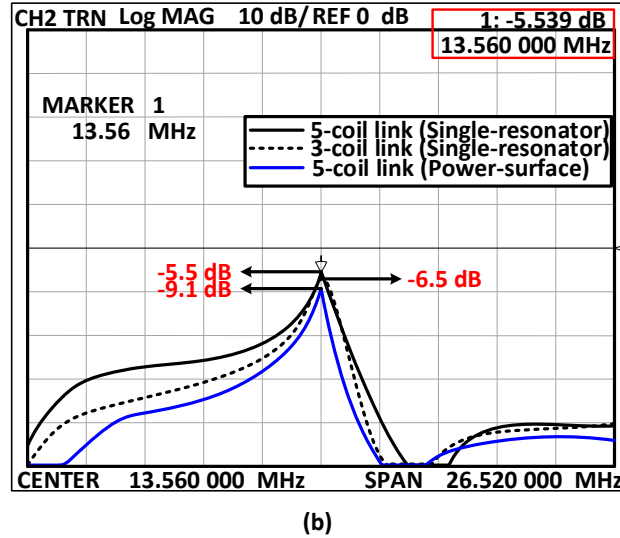
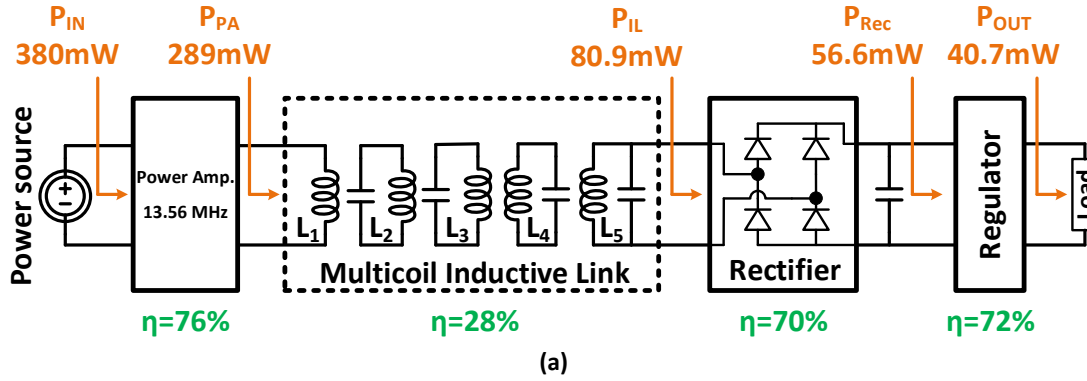


Figure 3.3 – (a) The full block diagram of the power transmission system includes a Class E power amplifier, a 5-coil inductive link, a rectifier, a regulator and end load. (b) The measured transmission coefficient of the 3-coil link and 5-coil link (for a single resonator and the power surface) at frequency of 13.56-MHz.

MHz, which frequency lies in an unlicensed ISM band. These overlapped primary resonators cover an area of $25 \times 16 \times 6 \text{ cm}^3$ for a receiver size of $1 \times 1 \text{ cm}^2$. The arrays of overlapped primary resonators provide uniform power distribution along the x and y and z directions.

The full block diagram of the power link supplied from a single primary resonator is presented in Fig. 3.3(a). Fig. 3.3(b) shows a measured 1-dB improvement of the transmission coefficient (S_{21}) of the proposed 5-coil power link compared with an optimized 3-coil link version for single resonators. The implantable resonator (L_4), the power receiver coil (L_5), and the implanted wide-band antenna are all printed on a single flexible polyimide printed circuit board (PCB). Both the flexible implantable coil and the flexible implantable antenna have a size of $1 \times 1 \text{ cm}^2$.

Fig. 3.4 shows the implemented system including the smart home-cage and the implantable interface. A class E power amplifier is used to provide the input power to the primary coil L_1 of the inductive link. The resonator array (L_{2i}) and the primary coil L_1 are separated by a distance of 1 cm. A wire wounded coil is used for the resonator L_3 which could be located above the scalp, outside the body of the mouse, while the resonator L_4 and the RX coil L_5 (implemented as a double-sided coil), are located below the scalp and inside the body, respectively. Table 3.1 summarizes the specifications of the implemented coils for this system.

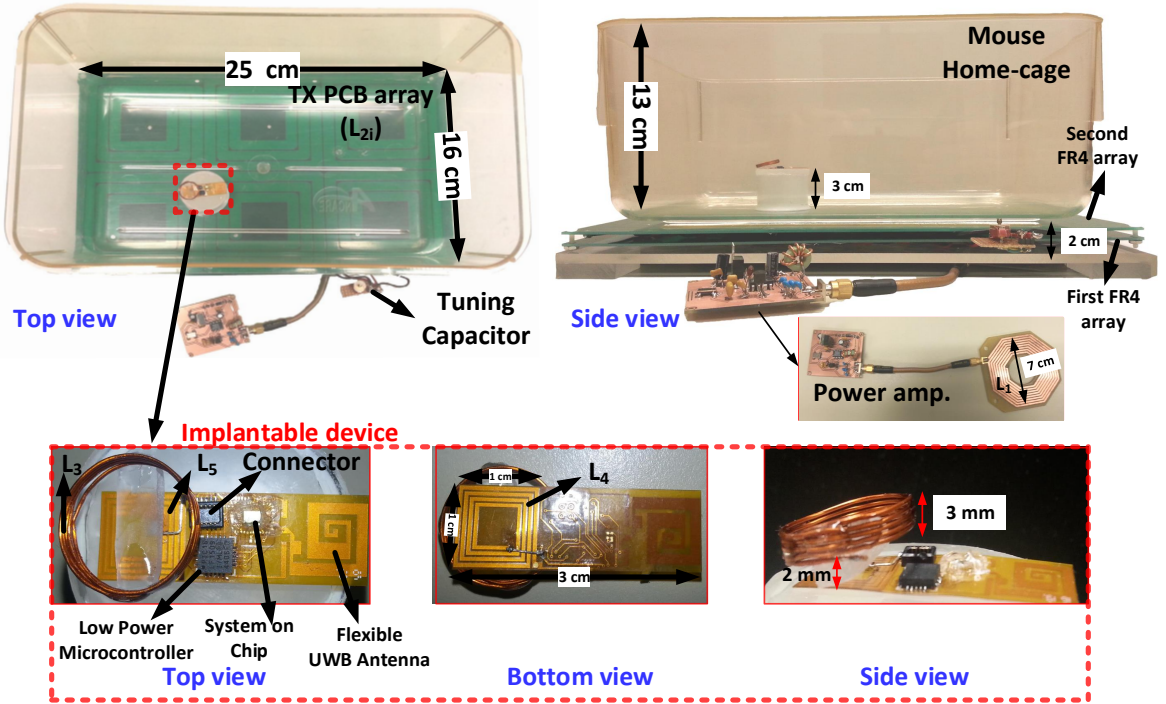


Figure 3.4 – Implemented power surface prototype located below a mouse home-cage and proposed wireless implantable device.

TABLE 3.1 – SPECIFICATIONS OF THE IMPLEMENTED SPIRAL COILS

Parameters	L_1	L_{2i}	L_3	L_4, L_5
Inductance, L (μH)	3.74	1.1	0.6	1.2
Quality factor, Q	80	306	31	22
Outer diameter, d_o (mm)	70	90	1.5	10
Inner diameter, d_i (mm)	32.5	35	1.4	4.8
Line width, W (mm)	2	9	0.5	0.5
Line spacing, S (μm)	70	90	1.5	10
Number of turns (N)	8	3	5	4
Type of coil	Printed	Printed	Wire wound	Wire wound

3.4 Measurement Results

Fig. 3.5(a) presents the measured power delivered to the load and the power transfer efficiency of the multi-coil inductive link as a function of the distance between the primary resonator array and the secondary resonator coil. As shown, the optimum separation distance lies between 3 cm and 5 cm, which corresponds to the maximum obtained PDL and PTE. The power delivered to the load is measured for the implemented power surface prototype at a typical distance of $d=4$ cm between the array and the RX coil, which is considered as a nominal distance for applications with mouse. Fig. 3.3(a) shows the measured efficiency of the power transmission system. The class E power amplifier, which is utilized to drive the primary coil of the inductive link, has an output power of 289 mW and efficiency of 76%. As illustrated in Fig. 3.3(b), the transmission coefficient (S_{21}) of the multi-coil inductive link is measured with a network analyzer, and equals -5.5 dB for a single resonator and -9.1 dB at $d=4$ cm, everywhere within the effective area of the array.

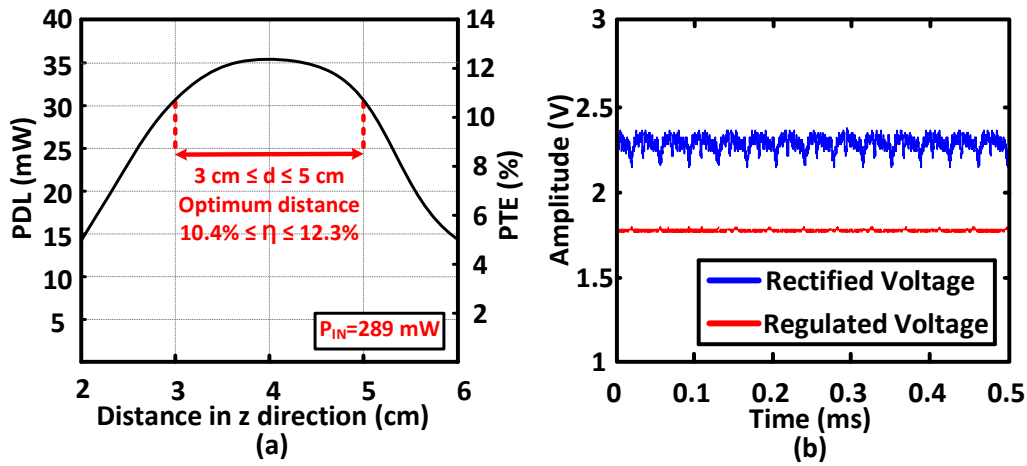


Figure 3.5 – (a) Measured power delivered to the load and power transfer efficiency of the multi-coil inductive link along the Z axis. (b) The measured voltage of the rectifier and regulator at $d=4$ cm.

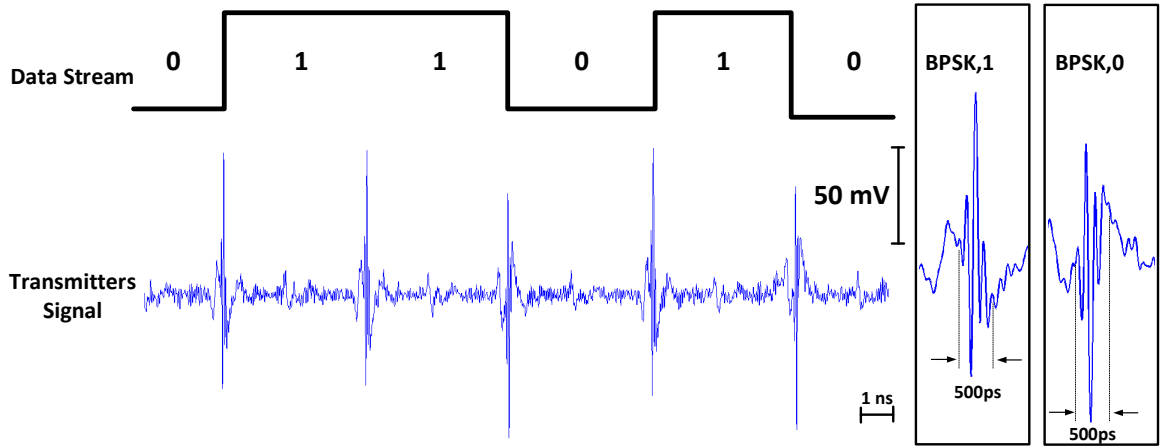


Figure 3.6 – The measured output data of the transmitter while powered up by the proposed 5-coil inductive link showing the generated short-impulse transmitter signals using BPSK modulation at a rate of 100 Mbps.

The measured dimension of the overall effective area is $16 \times 25 \text{ cm}^2$. When the receiver is located within this effective area, it receives maximum power. The measured maximum PDL and PTE of the link are 35.5 mW and 12.3%, respectively. A resistor of 100 ohms is utilized to model the typical load supplied by the receiver, and the frequency of the power carrier is 13.56-MHz. The power recovery unit, including the rectifier and the regulator circuits, which is implemented inside the SoC, provide the DC supply voltage extracted from the transmitted carrier through the inductive link. The output signal of the rectifier and the regulator circuit for a typical distance of $d=4 \text{ cm}$ is shown in Fig. 3.5(b). The implemented short impulse BPSK transmitter provides two short length pulses with 180 degrees phase difference for representing a ‘0’ and a ‘1’. Fig. 3.6 shows a sequence of transmitted impulses of 500-ps duration at 100-Mbps, while the transceiver is wirelessly powered up inside the home-cage. The RX antenna is placed at a distance of 16 cm of the TX antenna, inside the home-cage. The peak-to-peak voltage values of the transmitted BPSK short-pulses is 125 mV and 120 mV for a ‘0’ and a ‘1’, respectively. A maximum data rate of 800-Mbps was reached while the transceiver was wirelessly powered by the proposed 5-coil power link inside the home-cage. A micrograph of the fabricated SoC, including the full-duplex transceiver and the power management unit, fabricated in a $0.18\text{-}\mu\text{m}$ TSMC CMOS process is shown in Fig. 3.7. This SoC includes a 2.4-GHz receiver (LNA, mixer and an output buffer), the impulse radio transmitter (data modulator and pulse shaping circuit) and the power recovery/management unit, including the rectifier and the LDO regulator (Fig. 3.3(a)). The size of the integrated receiver is 0.375 mm^2 , while the integrated transmitter occupies 0.1 mm^2 . The total size of the power recovery unit is 0.06 mm^2 , and the size of the whole chip is 0.8 mm^2 .

Table 3.2 compares the proposed power transmission system with recently published works. Parameter d is the separation distance between the multi-coil transmitter array (L_{2i}) and the receiver coil (L_5), and d_{or} is the outer diameter of coil L_5 , which is implanted in the proposed design. In the proposed power

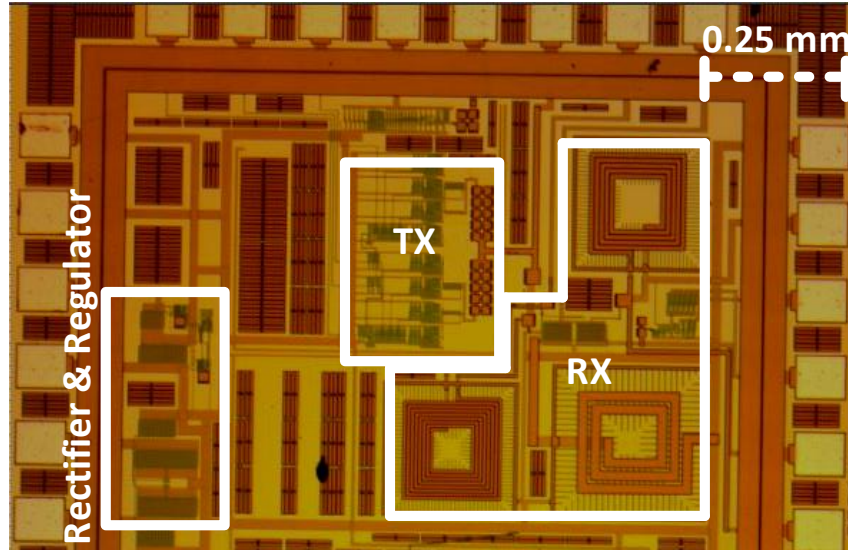


Figure 3.7 – The chip micrograph of the fabricated circuit in a CMOS 180-nm process.

TABLE 3.2 – PARAMETER COMPARISON WITH THE STATE OF THE ART

References	Array size (cm^2)	d/dor (cm/cm)	PTE (%)	PDL (mW)	FOM
[86]	25×42	7/2	14	42	20.5
[87]	29×20	1.5/3	25.9	43	5.57
[64]	58×60	12/4	6.2	20	3.72
[65]	18×34	3/1.2	17	1.7	0.73
[92]	27×27	1-15/2	20	36	14.4
This work (Single-resonator)	-	3-5/1	28	80.9	113
This work (Power-surface)	18×27	3-5/1	12.3	35.5	21.8

link, the size of the RX and TX coils are designed to match with the size of the head of the mouse and with the separation distance between the power transmitter array and the power receiver located below the scalp of the animal. As it can be seen in Table 3.2, the proposed system has the smallest receiver size for a given separation distance, and its measured PTE and PDL are among the highest achieved. The figure of merit (FOM) proposed in [92], which is $d/dor \times PTE \times PDL$, includes all the important parameters to compare different wireless power transmission systems together, and is used to compare the proposed system with previously published systems. As illustrated, the proposed link achieves the best FOM compared to other designs.

3.5 Conclusion

A wirelessly powered, fully-integrated, low-power full-duplex transceiver has been presented in this paper to support high-channel count stimulation and recording neural implants. In this design a single antenna is shared between the transmitter (TX) and the receiver (RX) to reduce implant size and complexity. The TX uses impulse short-radio impulses within the unlicensed ultra-wideband (UWB) based on an edge combining approach, and the RX uses a 2.4-GHz OOK narrow band topology. The proposed transceiver provides dual-band 500-Mbps TX uplink data rate and 100-Mbps RX downlink data rate fabricated in a 0.18- μm TSMC CMOS process occupying 0.8 mm^2 . The total measured power consumption of the RX at 100-Mbps is 5 mW and 6.7 pJ/bit for TX. Then, a smart home-cage system based on overlapped multi-coil arrays is utilized to wirelessly power up the SoC through an implantable multi-coil receiver of $1 \times 1 \text{ cm}^2$ of size. A measured power of 35.5 mW is delivered through this link to the receiver from typical separation distances ranging from 3 cm to 5 cm. The measured PTE of the 5-coil link inside the home-cage at $d=4 \text{ cm}$ is of 12.3% with a PDL of 35.5 mW. The power recovery circuit, which includes the 1.8-V voltage regulator to supply the TX circuits, and a 1.2-V voltage regulator to supply the RX circuits, occupies 0.06 mm^2 inside the SoC. The proposed 5-coil inductive power link and the integrated power recovery unit provide a total power transfer efficiency of 5% and deliver a regulated power of 18 mW to the load.

Chapitre 4

A Smart Neuroscience Platform with Wireless Power Transmission for Simultaneous Optogenetics and Electrophysiological Recording

Résumé

Cet article présente une plate-forme de neuroscience entièrement sans fil pour permettre des expériences optogénétiques ininterrompues avec des rongeurs de laboratoire vivants. Le système comprend une cage domestique de transmission de puissance sans fil (WPT) utilisant une liaison résonnante à 4 bobines, un système de suivi de mouvement, un headstage optogénétique multicanaux et une station de base. La cage domestique WPT utilise un nouveau réseau hybride de transmetteurs (TX) de puissance et des résonateurs multi-bobines segmentés pour atteindre une efficacité de transmission de puissance élevée (PTE) et délivrer une puissance élevée sur des distances allant jusqu'à 20 cm. Le récepteur (RX) de puissance à bobines multiples utilise une bobine RX d'un diamètre de 1 cm et une bobine de résonateur d'un diamètre de 1,5 cm. L'efficacité moyenne du transfert de puissance WPT est de 29,4 %, à une distance nominale de 7 cm, pour une fréquence de porteuse de 13,56 MHz. Il a des PTE maximum et minimum de 50 % et 12 % le long de l'axe Z, respectivement, et peut délivrer une puissance constante de 74 mW pour alimenter le headstage neuronal miniature. Le headstage neural comprend 1 canal de stimulation optique et 4 canaux d'enregistrement. Nous montrons que la cage domestique WPT hybride peut alimenter correctement le headstage sans interruption, tandis que le système de suivi de mouvement peut suivre l'activité de l'animal en temps réel pour permettre une évaluation comportementale et physiologique simultanée. En outre, un dispositif implantable intégré dans le processus TSMC CMOS 0,18- μm , qui comprend 64 canaux d'enregistrement, 16 canaux de stimulation optique, capteur de température, émetteur-récepteur et unité de gestion de l'alimentation,

a été introduit dans ce chapitre. Pour montrer la performance du circuit PMU, le circuit intégré est alimenté à l'intérieur de la cage domestique WPT en utilisant une bobine réceptrice d'un diamètre de 1,5 cm. Deux tensions réglées de 1,8 V et 1 V fournissent 79 mW de puissance pour tout le système sur une puce..

Abstract

This paper presents a fully wireless neuroscience platform for enabling uninterrupted optogenetic experiments with live laboratory rodents. The system includes a Wireless Power Transmission (WPT) home-cage using a 4-coil resonant link, a motion tracking system, a multichannel optogenetic headstage and a base station. The WPT home-cage uses a new hybrid parallel power transmitter (TX) coil array and segmented multi-coil resonators to achieve high power transmission efficiency (PTE) and deliver high power across distances as high as 20 cm. The multi-coil power receiver (RX) uses an RX coil with a diameter of 1 cm and a resonator coil with a diameter of 1.5 cm. The WPT home-cage average power transfer efficiency is 29.4%, at a nominal distance of 7 cm, for a power carrier frequency of 13.56-MHz. It has maximum and minimum PTE of 50% and 12% along the Z axis and can deliver a constant power of 74 mW to supply the miniature neural headstage. The neural headstage includes 1 optical-stimulation channel and 4 recording channels. We show that the hybrid WPT home-cage can properly power up the headstage without interruption, while the motion tracking system can track the activity of the animal in real time for enabling simultaneous behavioural and physiological assessment. Also, an implantable device integrated into 0.18- μm TSMC CMOS process has been introduced in this chapter which includes 64 recording channels, 16 optical-stimulation channels, temperature sensor, transceiver and Power Management Unit (PMU). To show the performance of the PMU circuit, the integrated circuit powered up inside the WPT home-cage using receiver coil with a diameter of 1.5 cm. Two regulated voltages of 1.8 V and 1 V provided 79 mW of power for all the system on a chip.

4.1 Introduction

Optogenetics and electrophysiology are state-of-the-art approaches in neuroscience used to advance our knowledge about brain functions, and to develop new therapeutics against brain diseases [67, 94, 95]. Using these experimental approaches with freely moving animals is a milestone, but requires robust, miniature, lightweight and experimental wireless systems. Small batteries have been used to power up different implantable sensors [96], but they limit the size, weight and the autonomy [97]. Neuroscience platforms utilizing Wireless Power Transmission (WPT) have been designed to avoid the utilization of a battery, and enable uninterrupted experiments with live animals. The concept is shown in Fig. 4.1 : a power amplifier converts a DC supply voltage into an AC power carrier passed to a primary coil (the power transmitter (TX) of the link), which has mutual coupling with a secondary coil (the power receiver (RX) of the link). The RX coil conveyed the received power carrier to a Power Management Unit (PMU) where it is rectified and regulated to extract a DC supply voltage. In this application, the PMU must supply several modules including a low-noise multichannel data acqui-

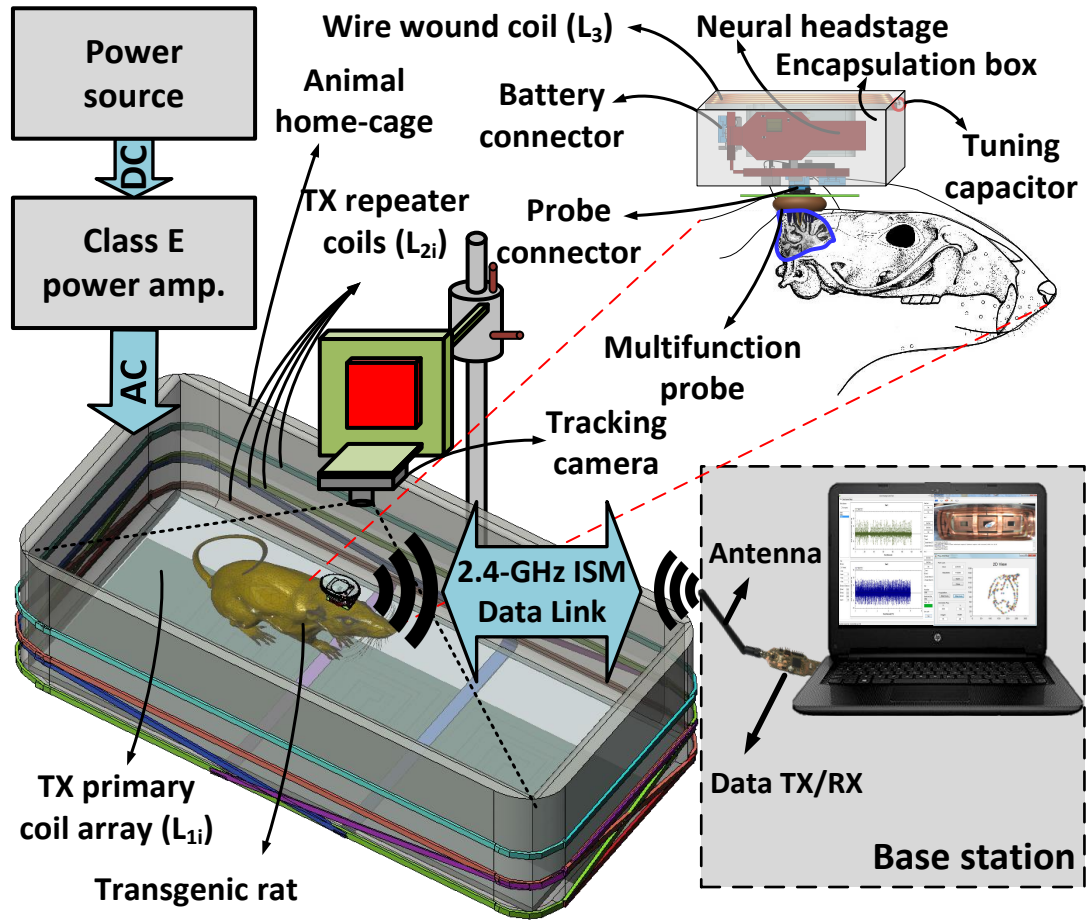


Figure 4.1 – Representation of the wireless neuroscience platform including a wireless neural headstage, a multi-coil resonant WPT system, a motion tracking system and a wireless base station.

sition system, a wireless radio transceiver, a Micro-Controller Unit (MCU) and a high power neural stimulator (either electrical or optical), etc. Therefore, increasing the PTE and the Power Delivered to the Load (PDL) are essential milestones in the design of robust wireless power transmission links intended for this application.

Additional coils can be used between the TX and RX coils as resonators to increase the coupling factor and to extend the transmission distance. The design and optimization of 3-coil resonator links have been extensively covered. In [59], a 3-coil link is designed and optimized for a carrier frequency of 13.56 MHz. It is shown that the 3-coil inductive link achieves a longer transmission distance than the 2-coil inductive link at maximum PTE and PDL. A 5-coil inductive link is used in [98] for increasing the PTE and the PDL with a small RX coil. It uses a TX primary coil, a TX coil array including 15 paralleled printed coils as a resonator, and a power RX including a small wire wound resonator coil and a double-sided flexible implantable coil implementing a third resonator coil and an RX secondary coil. The demonstrated prototype provides nearly constant power transmission across a separation distance of 4-6 cm. Different platforms previously published provide uniform wireless power transmission through different strategies and mechanisms, but most solutions are barely suitable for utilization with standard home-cage products. In [64], such a platform is used to transfer data and power through a 4-coil link. The power link can focus the transmitted power towards a moving receiver using a coil array and a closed-loop power control unit, which is tracking the location of the receiver in real-time using a small magnetic tracer placed in the body of the mouse. In [92], a method for enabling uniform power transmission, while avoiding the utilization of a complex closed-loop control strategy, is presented. Two TX resonator coil arrays are connected in parallel at the bottom and at the top of the platform to make the transmitted power nearly constant in 3D, everywhere within the delimited volume. Different motion tracking systems have also been developed to track the position of the animal inside the home-cage in real-time to correlate physiological events with behaviour [55], [65], and [66].

A 4-coil link WPT system, built around a standard home-cage is presented in [67]. Copper foil is used to implement a resonator on the TX side. A magnetic resonant multi-coil design is used to localize the transmitted power from a single TX coil at the bottom of the cage toward the RX. It achieves a separation distance of 0 to 17 cm with a maximum PTE of 51%, exhibiting a PTE drop in the middle of the home-cage.

We introduce a new wireless neuroscience platform including a WPT home-cage, a battery-less miniature neural headstage and a motion tracking system (Fig. 4.2(a)). The WPT home-cage system with hybrid resonant link provides uniform PTE achieve longer separation distances across the home-cage, compared to previous solutions. The headstage, which is wirelessly powered up by the WPT home-cage, includes 4 neural recording channels and 1 high-power optical-stimulation channel for optogenetics. The motion tracking system consists of a camera, an MCU and a Matlab user interface providing a 2D tracking diagram in real-time of the position of the animal.

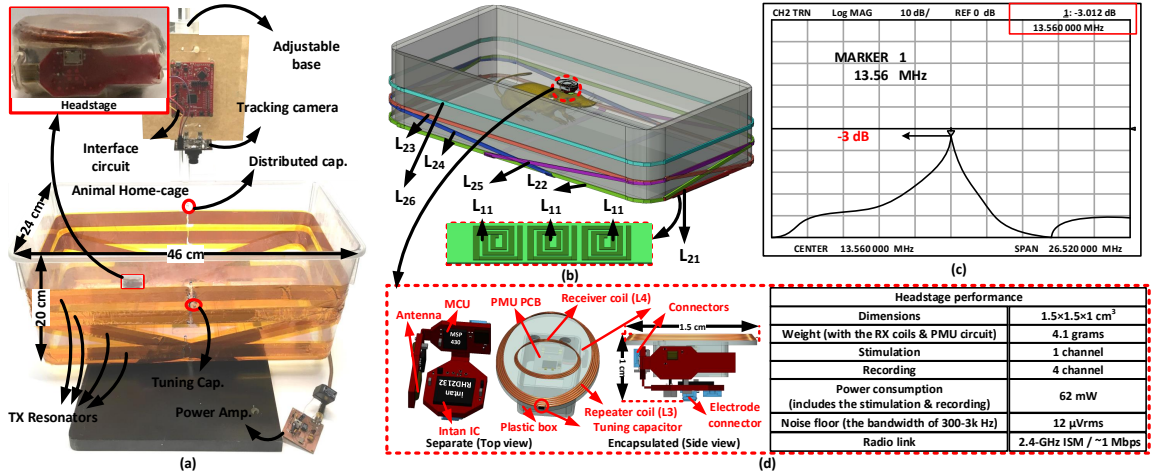


Figure 4.2 – (a) WPT home-cage prototype, and animal motion tracking system, (b) overview of the 4-coil resonant link including the primary coil array (L_{1i}) and the segmented resonators (L_{2i}), (c) measured transmission coefficient of the 4-coil resonant link, (d) the wireless headstage and the multicore receiver, including the RX resonator (L_3) and the RX secondary coil (L_4).

4.2 System Overview

As shown in Fig. 4.1, the proposed wireless platform with resonant power transmission includes three main parts : 1) a wireless neural headstage, 2) a hybrid resonant link, and 3) a motion tracking system.

Wireless Neural Headstage

The headstage, which was previously described in [96], is built using only off-the-shelf components that are mounted on a foldable flex-rigid that can fold around the WPT system. The PCB consists of four main building blocks : 1) an RHD2132 neural recording chip from Intan Technologies, USA, 2) a 2.4-GHz nRF24L01 ISM wireless transceiver from Nordic Semiconductor, Norway, 3) a PMU and 4) a low-power MSP430F5328 MCU from Texas Instruments (TI), USA. In such a system, the neural recording interface is conditioning and digitizing the neural signals acquired from up to four microelectrodes, with bandwidth selection. It can be configured to acquire the Local Field Potentials (LFP), or the spikes. The RHD2132 is configured to sample the neural signals with a precision of 16 bits at 20 ksamples/s. The headstage can stimulate optically using a high power LED driver, which can provide a maximum regulated forward current of 150 mA to accommodate various types of LEDs for optogenetics applications. The performance of the neural headstage are summarized in Fig. 4.2(d).

Hybrid Resonant Link

The resonant power transmission system uses a coil array and segmented resonators for the TX and uses a resonator and a secondary coil for the RX. On the TX side, a class E power amplifier is used

to provide power to the TX including a primary coil array and resonators. The primary coil array includes 3 parallel FR4 printed coils (L_{11} , L_{12} and L_{13}), while the segmented resonators (L_{21} , L_{22} , L_{23} , L_{24} , L_{25} and L_{26}) are implemented using copper foil with 25 mm width and 80 μm thickness placed around the animal's home-cage (Fig. 4.2(a)). The power receiver (on the headstage side) includes the secondary resonator L_3 , and the receiver coil L_4 (Fig. 4.2(b)). L_{11} , L_{12} and L_{13} are connected in parallel and connected to the output of the power amplifier, as shown in Fig. 2(a). The 6 segmented TX resonators are wrapped around a standard home-cage with a size of $24 \times 46 \text{ cm}^2$, and are virtually in parallel [94], [67]. As illustrated in Fig. 4.2(a), each coil of the TX resonator is separated into two segments leveraging the distributed capacitors to obtain better quality factor [94]. The resonant frequency of the segmented resonators L_{2i} is adjustable using the variable capacitor connected with L_{21} . The transmission coefficient (scattering parameter S_{21}) of the 4-coil link is shown in Fig. 4.2(c). The maximum measured PTE of the link is 50%. As illustrated in Fig. 4.2(d), a wire wounded coil with a diameter of 1.5 cm is used as secondary resonator (L_3). The receiver coil L_4 uses a 1-cm of diameter wire wounded coil, which is connected to the PMU on the headstage side. The PMU includes a voltage

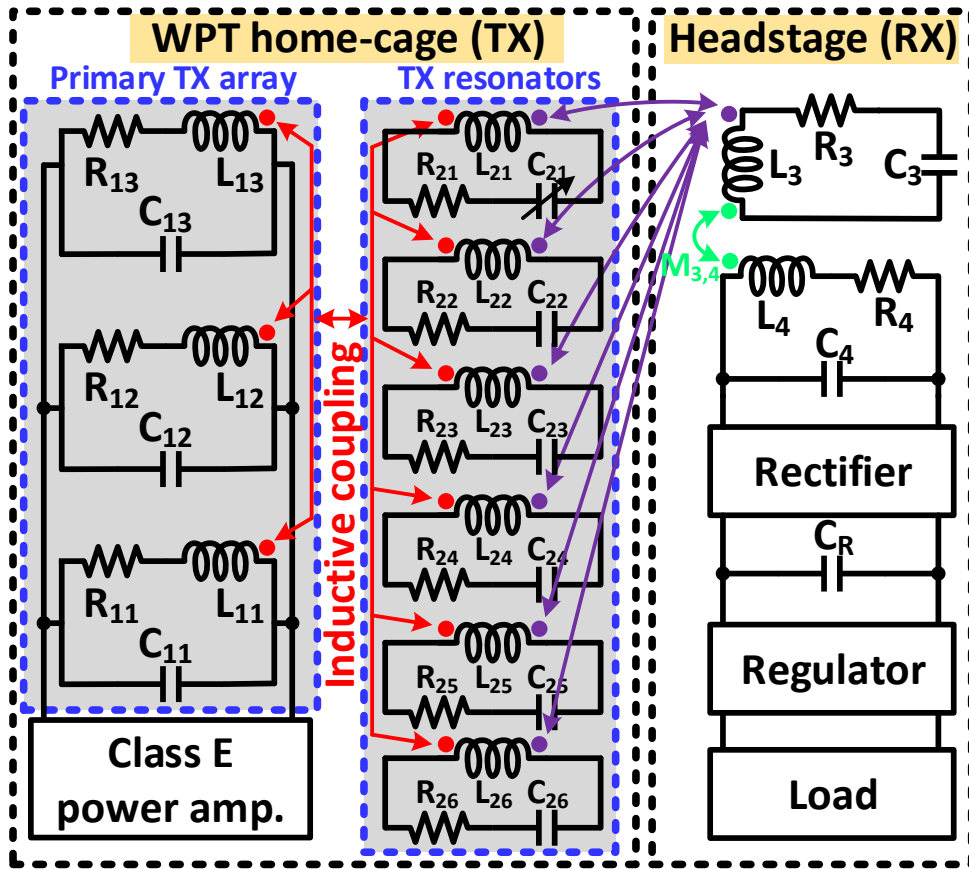


Figure 4.3 – Schematic of the equivalent circuit of the proposed wireless power transfer system.

TABLE 4.1 – SPECIFICATIONS OF THE COILS USED IN THE WPT HOME-CAGE

Parameters	L_{1i}	L_{22}, L_{23}	L_{24}, L_{25}	L_{21}, L_{26}	L_3	L_4
Inductance, L (μH)	1.2	0.9	0.87	0.85	0.8	0.6
Quality factor, Q	117	138	143	141	135	112
Outer diameter, d_o (cm)	13	26×46	24×22	24×46	1.5	1.5
Inner diameter, d_i (cm)	4.7	26×45	23×22	23×45	1.4	1.4
Line width, W (mm)	2	25	25	25	0.5	0.5
Line spacing, S (μm)	380	-	-	-	20	20
Thickness, t (μm)	-	80	80	80	-	-
Number of turns (N)	3	1	1	1	6	4
Type of coil	PCB	Foil	Foil	Foil	Wire	Wire

rectifier and a linear voltage regulator located inside the headstage. Fig. 4.3 shows the circuit schematic of the power TX and power RX of the WPT system, separately. The arrows indicate the coupling between the different coils of the system using different colours. The mutual coupling between L_{1i} - L_3 (K_{13}), L_{1i} - L_4 (K_{14}), and L_{2i} - L_4 (K_{24}) are neglected because of the large distance and significant difference in their sizes. The power transfer efficiency of the whole WPT system can be described by

$$PTE = \eta_{12} \times \eta_{23} \times \eta_{34} \quad (4.1)$$

where η_{12} , η_{23} and η_{34} are the power efficiencies between L_{1i} - L_{2i} , L_{2i} - L_3 and L_3 - L_4 , respectively. The PTE of the WPT system can be described by

$$PTE = \frac{K_{12}^2 Q_1 Q_2}{1 + K_{12}^2 Q_1 Q_2} \times \frac{2K_{23}^2 Q_2 Q_3}{(2 + K_{34}^2 Q_3 Q_4)^2} \times K_{34}^2 Q_3 Q_4 \quad (4.2)$$

where K_{12} is the mutual coupling between L_{1i} and L_{2i} , K_{23} is the mutual coupling between L_{2i} and L_3 , K_{34} is the mutual coupling between L_3 and L_4 , $Q_1 = \omega_p L_1 / R_1$, $Q_2 = \omega_p L_2 / R_2$, $Q_3 = \omega_p L_3 / R_3$ and $Q_4 = \omega_p L_4 / R_4$. Table 4.1 summarizes the specifications of the implemented coils.

Wireless Neuro Interfacing Microsystem

A wireless implantable microsystem device has been designed to be powered up using WPT home-cage. As illustrated Fig. 4.4, this system including 64 recording channels, 16 optical stimulation channels for enabling chronic optogenetic experiments with live laboratory mice, a wireless IR transmitter (TX) using a merged BPSK-OOK modulation scheme with a center frequency of 1.8 GHz, a narrow band 4.9-GHz OOK receiver that shares the antenna with the transmitter for minimal invasiveness, a temperature sensor and the power management unit (PMU).

The proposed design includes a multichip Master/Slave antenna sharing strategy enabling to scale up the system to higher recording and stimulating channel counts simply by interconnecting several chips together. The Master chip (Chip #1 in Fig. 4.4) provides two phases derived from the input

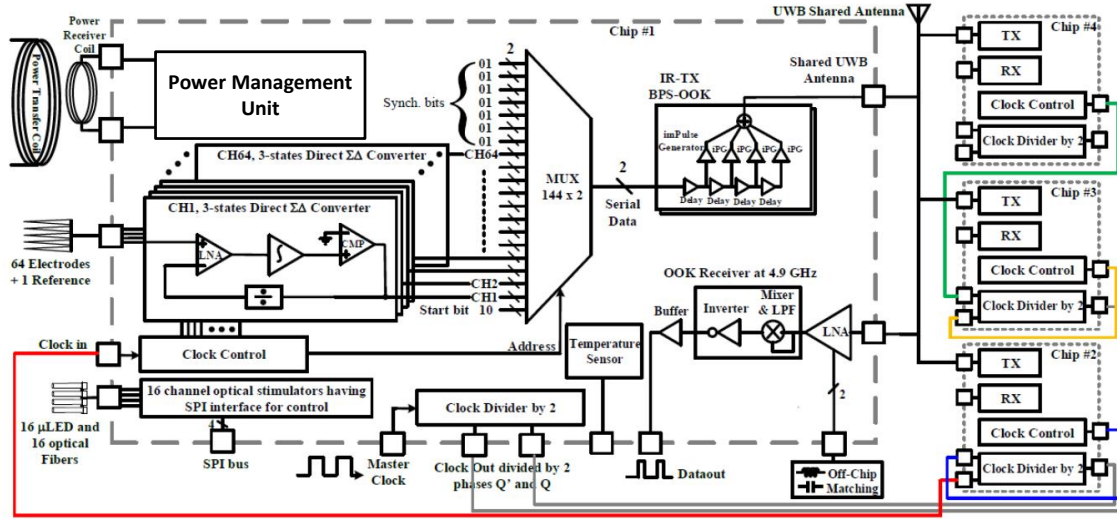


Figure 4.4 – Block diagram of the proposed system.

clock divided by two to the slave chips. Then, two other slave chips divide the clock by two again, resulting into four different clock phases derived from the input clock signal divided by 4. Therefore, the TX modules pertaining to all master/slave chips are all multiplexed towards the same antenna, while the RX of the Master chip retrieves the downlink data from the same antenna and passes it to the micro-controller. Thus, all chips can share a single antenna and a single power receiver coil through this Master/Slave scheme without the need for any additional components. Fig. 4.4 shows the interconnections between the Master and slave chips for a four-chip system (256 recording/64 photo-stimulation).

The circuit diagram of the different blocks used in PMU design is shown in Fig. 4.5. The PMU circuit includes a rectifier circuit, reference voltage, and LDO which is used to generate two regulated voltages of 1.8 V and 1 V for all the system on the chip. The signal received by the RX coil will be applied to the input of the first block of the circuit which is the rectifier [99]. Optimization of transistor sizes is based on simple scaling relationships. Bigger W/L means bigger parasitic capacitance and smaller series resistance. The main contributor to series resistance is the gate resistance R_G ; as W increases, more gate fingers can be used, so R_G decreases. Thus, the Q remains roughly constant, while R_P decreases. L is kept fixed at the minimum allowed value in the process, and W is varied to change the device size. The voltage drop per stage scales as $\log(L/W)$ for subthreshold operation, and as $\sqrt{L/W}$ above the threshold, and this is a weak function of device size. The sizes of the NMOS and PMOS transistors and capacitors in Fig. 4.5 are as follows : $(W/L)_{M3} = (W/L)_{M4} = (4 \mu\text{m}/0.18 \mu\text{m})$, $(W/L)_{M1} = (W/L)_{M2} = (1.2 \mu\text{m}/0.18 \mu\text{m})$ and $C_C = 250\text{fF}$.

The rectified voltage will be applied to the 1.8 V regulator which is sharing a reference voltage with a 1 V regulator and a low drop out (LDO) circuit to regulate the rectified voltage [100]. The LDO circuit consists of five main units : voltage reference, voltage source, an error amplifier, pass transistor,

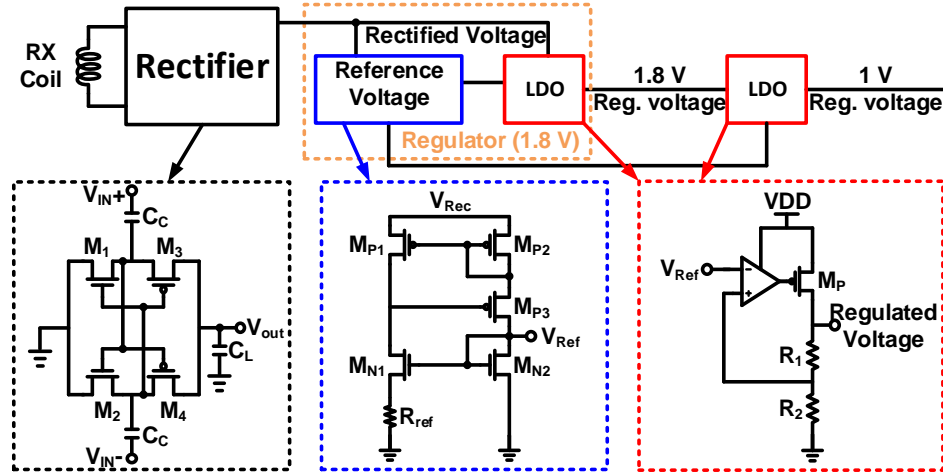


Figure 4.5 – The block diagram of the PMU circuit.

and resistive divider [101]. The differential error amplifier along with pass transistor constitutes an amplifier structure with negative feedback through the resistive divider, ensuring the required output level. The regulated voltage of 1.8 V will be used as a power source of the on-chip circuit such as recording channels, LED driver, transmitter and temperature circuits. The output of the 1.8 V LDO will also be applied to LDO circuit of 1 V to provide the VDD of the Receiver and mixer circuits. This system is implemented in TSMC 0.18- μm and occupies 12 mm^2 as shown in Fig. 4.6.

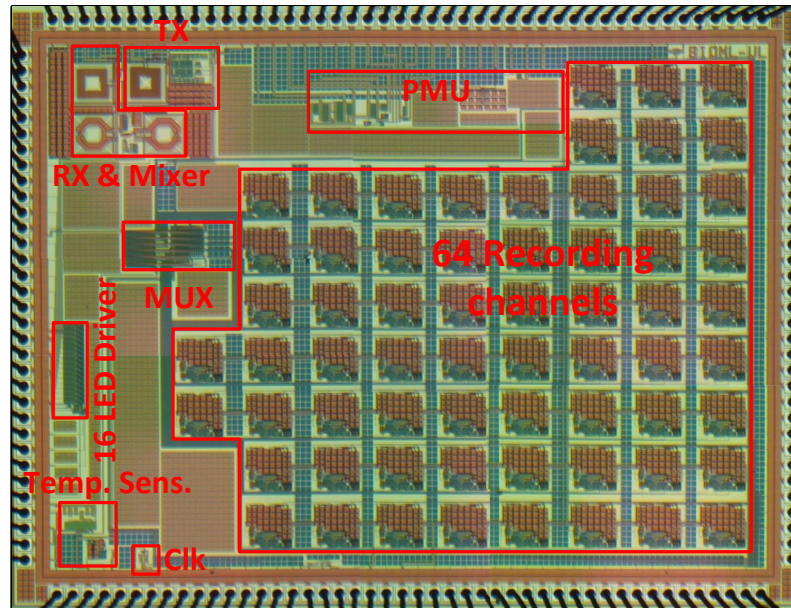


Figure 4.6 – Die photograph of the chip fabricated in a 0.180- μm CMOS process and occupying 3 mm x 4 mm.

Motion Tracking System

The motion tracking system, which includes an adjustable base, a Pixy R1.3A camera from CMUcam, a MSP-EXP430F5529LP Launchpad from TI, and a Matlab user interface program running on a PC, is shown in Fig. 4.7(a). The Pixy-cam processes images and transmits the X, Y coordinates of the object in motion to the MSP430F5529 microcontroller that reads the position of the animal. Data are stored and transmitted via USB to the PC host. A Matlab program that runs in real-time on the PC host reads the stream of the input vectors [X,Y]. Fig. 4.7(b) shows the interface program of the motion tracking system running on the PC and displaying the motion tracking path in real time. The position is printed on a 2D chart and continuously refreshed. Several markers can be monitored and printed simultaneously.

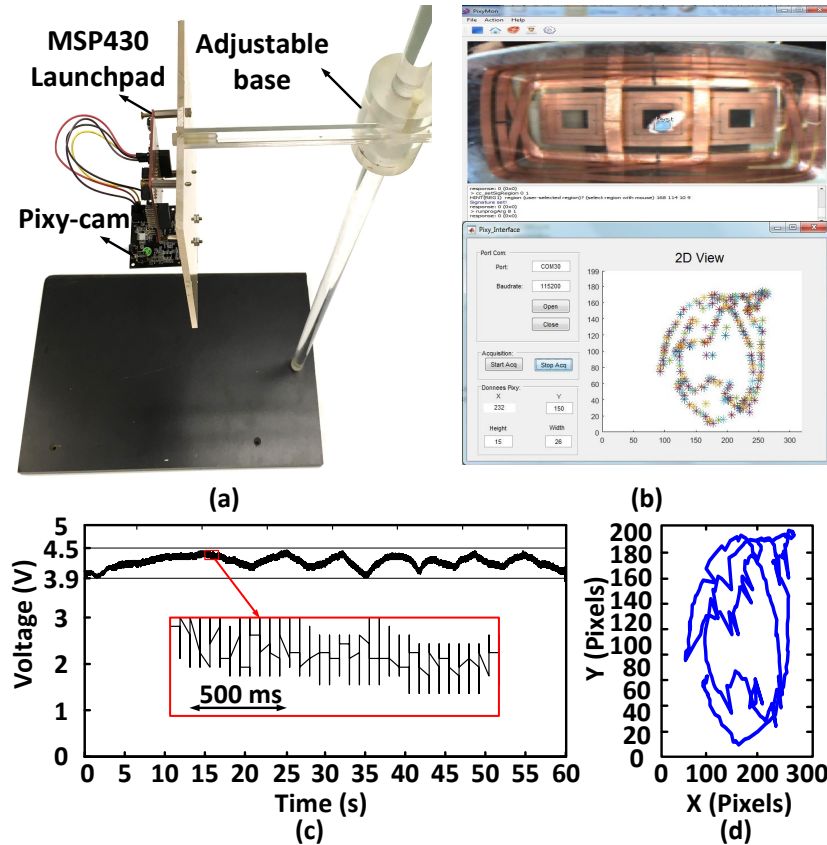


Figure 4.7 – (a) Motion tracking system, (b) user interface of the tracking system showing the tracking path, (c) measured voltage retrieved by the power RX on the headstage side (voltage across capacitor C_R), and (d) motion tracking path of an object moving inside the home-cage.

4.3 Measurement Results

Powered up Headstage Moving Inside WPT Home-cage

The PTE of the WPT system is measured when the receiver is swept across X-Y at the separation distance of $d=7$ cm inside the home-cage. The measured average PTE is 29.4%, and the minimum and maximum PTE are 12% and 50% from $d=0$ to $d=20$ cm along the Z axis, respectively. Fig. 4.7(c) shows the voltage variation across the capacitor C_R , in the PMU of the headstage, across time, while the headstage is moved inside the home-cage for 60 s.(Fig. 4.7(d)).

A $200\text{-}\mu\text{Vp-p}$ synthetic input signal is played in a Phosphate-buffered saline solution, using an arbitrary function generator, and recorded inside the home-cage with the headstage powered up by the WPT system (in Fig. 4.8(a)). The measured input referred noise of the system is of $12\text{-}\mu\text{V}_{\text{rms}}$ for a signal bandwidth of 300-Hz to 3-kHz. Fig. 4.8(b) shows one isolated synthetic spike recorded wirelessly with the headstage. The synthetic spike has a realistic amplitude of $100\text{-}\mu\text{Vp-p}$. As illustrated

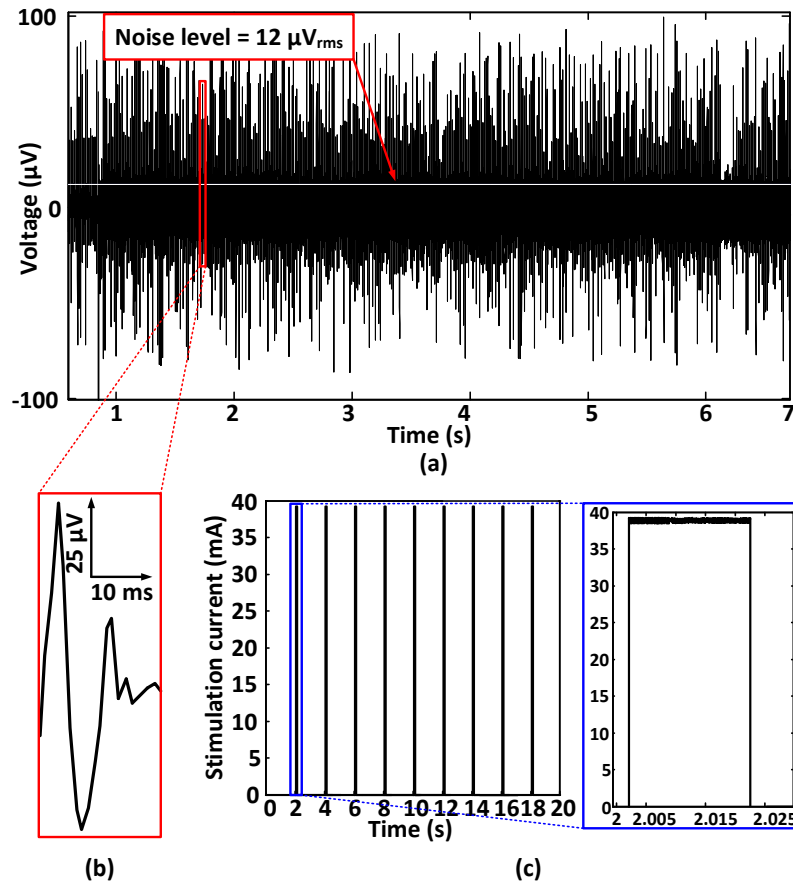


Figure 4.8 – (a) Measured $200\text{-}\mu\text{Vp-p}$ input synthetic neural signals using the headstage powered up wirelessly inside the home-cage with the WPT system, (b) an isolated recorded synthetic spike, and (c) the LED forward current provided by the wireless power link.

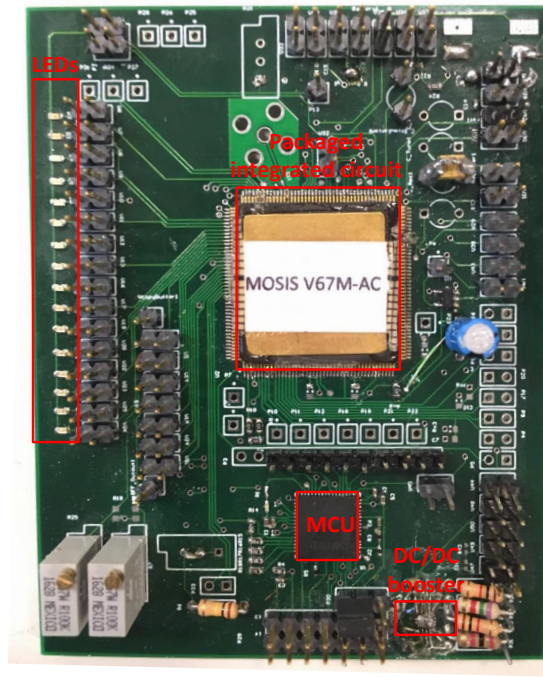


Figure 4.9 – The PCB prototype.

in Fig. 4.8(c), the LED driver powered from the wireless power link can provides a stimulation current of 40 mA, with a stimulation period of 2 s and a 10% duty cycle. This regulated output current of 40 mA is used to power up a fiber-coupled LED (LB G6SP from OSRAM Opto Semiconductors Inc.), which provides enough light power ($\geq 1 \text{ mW/mm}^2$) to activate ChR2 light-sensitive neurons [102].

Measured Performances of The Implantable Device Inside WPT Home-cage

The performance of the implantable device has been measured using the PCB prototype shown in Fig. 4.9 inside the WPT home-cage. This prototype features the packaged integrated circuit (IC), microcontroller(MSP4305328), 16 LEDs and a DC/DC booster. While clock generation and LED state management is handled by the firmware within the microcontroller unit, the DC/DC booster ensures voltage level shifting, from 1.8V to 4.2V, for charging the battery which provides the power of the LEDs. PMU circuit receives the power through a receiver with a diameter of 1.5 cm at the nominal distance of $d=7 \text{ cm}$. Fig. 4.10 shows the output of the rectifier circuit. The measured rectified voltage has a variation of 300 mV. The measured regulated voltages of 1.8 V and 1 V are illustrated in Fig. 4.11. A variation less than 5 % is achieved when providing a current of 40 mA for AFE, LED drivers and temperature sensor through regulated voltage of 1.8 V. Also, the measured regulated voltage of 1 V provides a current of 10 mA for the transceiver circuit. The measured regulated voltage of 1 V has a variation less than 80 mV. Indeed, PMU circuit can provide a power of 79 mW through both regulated voltages of 1.8 V and 1 V.

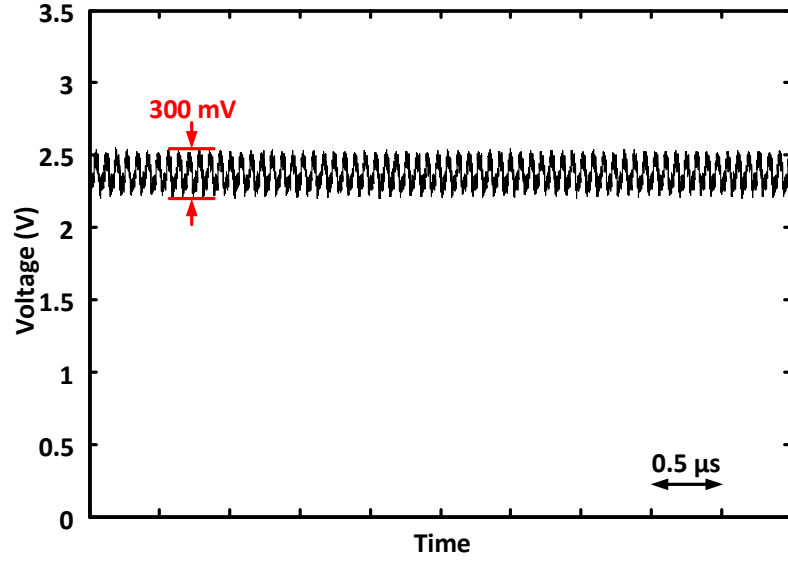


Figure 4.10 – The rectified voltage measured while the implantable device powered up inside WPT home-cage.

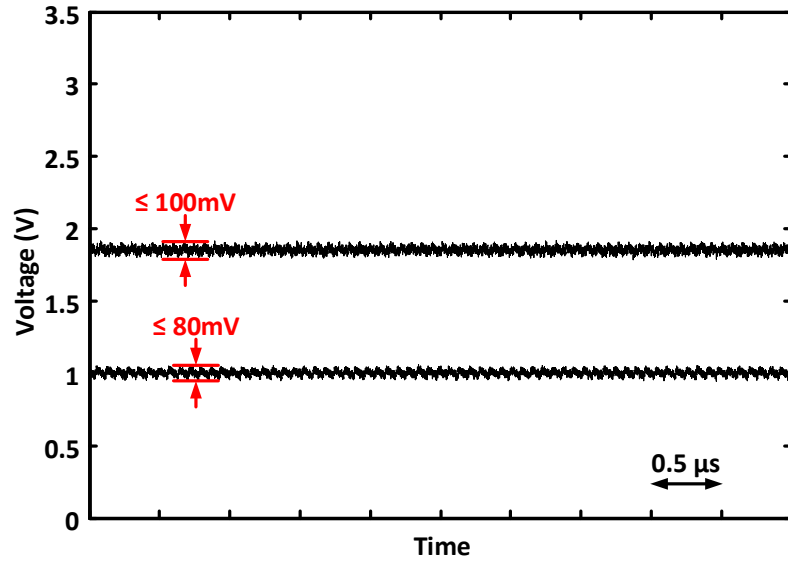


Figure 4.11 – The regulated voltages of 1.8 V and 1 V measured while the implantable device powered up inside WPT home-cage.

Table 4.2 summarizes the performance of the WPT system compared with the state-of-the-art using the FOM introduced in [98], which uses these parameters : the separation distance between the TX and RX coils (d) ; the size of the home-cage ; the size of the RX coil ; and the PDL and the PTE of the system. As shown in Table 4.2, the performance of the presented system is among the best-reported results. Using a parallel coil array in addition to 6 mutually in parallel segmented copper foil coils as

TABLE 4.2 – PERFORMANCE SUMMARY AND COMPARISON WITH THE STATE-OF-THE-ART

References	[67]	[98]	[64]	[92]	[65]	[66]	This work
Wireless link	4-coil	5-coil	4-coil	4-coil	2-coil	4-coil	4-coil
Size (cm^2)	24×46	18×27	50×60	27×27	18×34	29×20	24×46
Separation distance d (cm)	0-17	3-5	12	1-15	3	1.5	0-20
Receiver diameter d_{or} (cm)	2.2	1	4	2	1.2	2	1.5
Average PTE	18%	13%	19.6%	20%	17%	25.9%	29.4%
Minimum PTE	14%	11%	5%	-	4.7%	-	12%
PDL (mW)	65	64	20	36	1.2	43	74
FOM ($d/d_{or} \times PTE \times PDL \times Size$)	998	202	353	394	3.1	49	3200

a resonator array in this system improves the PTE uniformity and the transmission distance compared to previous solutions.

4.4 Conclusion

In this paper, a fully wireless neuroscience platform intended for conducting uninterrupted optogenetic experiments with freely moving laboratory animals has been presented. A real-time motion tracking system provides a 2D motion tracking diagram of the animal location inside the home-cage. A WPT home-cage system has been implemented using a hybrid resonant link with a carrier frequency of 13.56-MHz. A parallel coil array is used for the TX primary coil, while 6 segmented copper foil coils mutually in parallel using distributed capacitors, are used as TX resonators. On the headstage side, the power RX uses a small wire wounded RX resonator coil with a diameter of 1.5 cm and a secondary RX coil with a diameter of 1 cm, providing a maximum PDL of 74 mW to the headstage. The headstage includes 4 recording channels and 1 optical-stimulation channel and wirelessly communicates with a base station through a short-range 2.4-GHz ISM wireless link. The measurement results show an average PTE of 29.4% for the WPT system at a nominal distance of $d = 7$ cm, with maximum and minimum PTE of 50% and 12%, from $d = 0$ to 20 cm along the Z axis, respectively. Also, in this paper a PMU circuit designed and integrated in 0.18- μm TSMC CMOS process to provide the power for an implantable system for optogenetic application including 64 recording channels, 16 optical-stimulation channels, temperature sensor and transceiver. Two regulated voltages of 1.8 V and 1 V, providing 79 mW of power for all the system through a receiver coil with a diameter of 1.5 cm at the nominal distance of 7 cm inside the WPT home-cage.

Chapitre 5

A Wireless Neuroscience Platform for Uninterrupted Optogenetics and Electrophysiology Recording in Live Animals

Résumé

Une plate-forme de neuroscience intelligente est présentée dans cet article pour permettre des expériences optogénétiques et électrophysiologiques ininterrompues avec des rongeurs de laboratoire vivants. Ce prototype comprend un système de cage domestique à transmission de puissance sans fil (WPT) utilisant une liaison résonnante à 4 bobines, un système de suivi de mouvement, un headstage neuronal multicanaux et une station de base. La cage domestique WPT utilise un nouvel émetteur (TX) de puissance hybride basé sur un réseau de bobines parallèles et des résonateurs multi-bobines segmentés pour atteindre une efficacité de transmission de puissance élevée (PTE) et délivrer une puissance élevée sur des distances aussi élevées que 12 cm. Le récepteur (RX) de puissance à bobines multiples utilise une bobine RX d'un diamètre de 1,0 cm et une bobine de résonateur divisée d'un diamètre de 1,5 cm résistant au désalignement. L'efficacité moyenne du transfert de puissance WPT est de 32,6 %, à une distance nominale de 5 cm, pour une fréquence porteuse de 13,56 MHz. Il a un PTE maximum et minimum de 53 % et 15 % et peut fournir une puissance constante de 82 mW pour alimenter le headstage neuronal miniature. Le headstage neural comprend 1 canal de stimulation optique et 4 canaux d'enregistrement. Grâce à l'utilisation d'une bobine de répétition dédoublée pour L_3 du côté du récepteur, le lien de résonance hybride présenté est robuste au désalignement angulaire partout à l'intérieur de la home-cage. Un système de suivi de mouvement utilisant la caméra CMUcam5 peut suivre et enregistrer l'activité de l'animal en temps réel pour permettre une évaluation comportementale et physiologique simultanée. Nous démontrons la performance du système dans des expériences *in-vivo* avec une souris ChR2 en mouvement libre. L'optogénétique simultanée à l'enre-

gistrement électrophysiologique avec un système sans batterie sont démontrés pour la première fois chez un animal libre de ses mouvements. L'activité électrophysiologique a été enregistrée après une stimulation optogénétique dans le Cortex Cingulaire Antérieur (CAC) de la souris.

Abstract

A smart neuroscience platform enabling uninterrupted optogenetic and electrophysiology experiments with live laboratory rodents is presented in this paper. This system includes a wireless power transmission (WPT) home-cage system using a 4-coil resonant link, a multichannel neural headstage, and a base station. The WPT home-cage uses a new hybrid power transmitter (TX) based on a parallel coil array and segmented multi-coil resonators to achieve high power transmission efficiency (PTE) and to deliver high power across distances as high as 12 cm. The multi-coil power receiver (RX) uses an RX coil with a diameter of 1.0 cm and a new split resonator coil with a diameter of 1.5 cm, which is robust against misalignment. The WPT home-cage average power transfer efficiency is 32.6%, at a nominal distance of 5 cm, and at a power carrier frequency of 13.56 MHz, which represents an improvement of 7.2% over previous WPT home-cage systems. It has maximum and minimum PTE of 53% and 15% and can deliver a constant power of 82 mW to supply the miniature neural headstage. The neural headstage includes 1 optical stimulation channel and 4 recording channels. Thanks to the utilization of a split repeater coil for L_{3i} on the receiver side, the presented hybrid resonant link is robust to angular misalignment everywhere inside the home-cage. We demonstrate the performance of the system within an *in-vivo* experiments with a freely moving ChR2 mouse. Simultaneous optogenetic stimulation and electrophysiological recordings with a batteryless system are reported for the first time with a freely moving mouse. Electrophysiological activity was recorded while delivering optogenetic stimulation in the Anterior Cingulate Cortex (ACC) of the mouse.

5.1 Introduction

Optogenetics and electrophysiology are state-of-the-art approaches in neuroscience used to advance our knowledge of brain functions, and to develop new therapeutics against brain diseases such as Alzheimer [103–105] [1]-[3]. Using these experimental approaches with freely moving animals is a milestone, but requires robust, miniature, lightweight and experimental wireless systems. Small batteries have been used to power up different implantable sensors [96, 97, 106, 107] [4]-[7], but they limit the size, the weight and the autonomy. Neuroscience platforms utilizing WPT have been designed to avoid the utilization of a battery, and enable uninterrupted experiments with live animals [55, 60, 64, 92, 108] [8]-[12]. The concept is shown in Fig. 5.1 : a power amplifier converts a DC supply voltage into an AC power carrier that is passed into a primary coil (the TX of the link), which has mutual coupling with a secondary coil (the RX of the link). The RX coil conveys the received power carrier to a power management system (PMU) where it is rectified and regulated to extract a DC supply voltage.

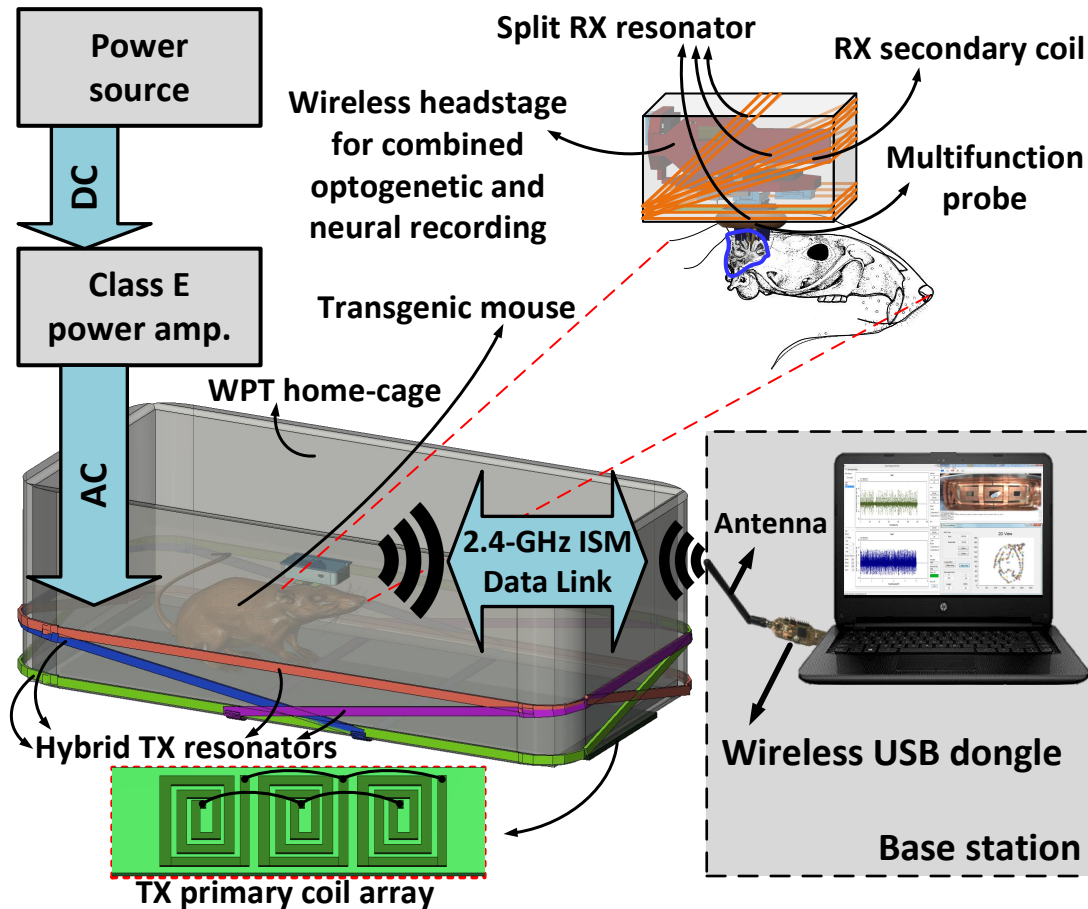


Figure 5.1 – Conceptual representation of the proposed wireless platform for combined optogenetics and electrophysiology experiments. It includes a hybrid (multi-coil/segmented) resonant link, a wireless multichannel optoelectronic headstage and a base station.

In this application, the PMU must supply several modules including a low-noise multichannel data acquisition system, a wireless radio transceiver, a microcontroller (MCU) and an optogenetic or an electrical stimulator. Therefore, increasing the PTE and the power delivered to the load (PDL) are important goals in the design of robust wireless power transmission links for this application.

Additional coils can be used between the TX and RX coils as resonators to increase the coupling factor and to extend the transmission distance. The design and optimization of 3-coil resonator links have been extensively covered. In [59] and [?], a 3-coil link is designed and optimized for a carrier frequency of 13.56 MHz. It is shown that the 3-coil inductive link achieves a longer transmission distance than the 2-coil inductive link at maximum PTE and PDL. In [109] a 4-coil inductive link designed and optimized for a power-link frequency of 700 kHz and a coil distance range of 10 to 20 mm, using a 22-mm diameter implantable coil resonance-based system, shows a power-transfer efficiency of more than 80%. A 4-coil resonance-based inductive link is designed and presented in [110]. The resonance coil of which is formed by an array of several paralleled coils as a smart power TX. The power transmitter employs simple circuit connections and includes only one power driver circuit per multi-coil resonance-based array, which enables higher power transfer efficiency and higher power delivery to the load than a 3-coil inductive link strategy. A 5-coil inductive link is used in [98] for increasing the PTE and the PDL with a small flexible square RX coil of $1 \times 1 \text{ cm}^2$. It uses a TX primary coil, a TX coil array including 15 paralleled printed coils as the resonator, and a power RX including a small wire wound resonator coil and a double-sided flexible implantable coil implementing a third resonator coil and an RX secondary coil. The demonstrated prototype provides nearly constant power transmission for a separation distance of 4-6 cm. Separation distance is the distance between the TX and RX coils in the inductive WPT systems. Different platforms previously published provide uniform wireless power transmission through different strategies and mechanisms, but most solutions are barely suitable for utilization with standard home-cage products [?, 55, 59, 60, 64, 92, 110, 111]. In [64], such a platform is used to transfer data and power through a 4-coil link. The power link can focus the transmitted power towards a moving receiver using a coil array and a closed-loop power control unit, which is tracking the location of the receiver in real-time using a small magnetic tracer placed in the body of the mouse. In [92], a method for enabling uniform power transmission is presented, while avoiding the utilization of a complex closed-loop control strategy. Two TX resonator coil arrays are connected in parallel, one at the bottom and one at the top of the platform to make the transmitted power nearly constant in 3D, everywhere within the volume of the cage. Different motion tracking systems have also been used to track the position of the animal inside the home-cage in real-time. 2D and 3D imaging systems using a Microsoft Kinect are described in [?]. Animal tracking via an array of magnetic sensors is performed in [60, 64].

A 4-coil link WPT system, built around a standard home-cage is presented in [112]. Copper foil is used to implement a resonator on the TX side. A magnetic resonant multi-coil design is used to focalize the transmitted power from a single TX coil at the bottom of the cage toward the RX. It achieves a separation distance of 0 to 17 cm with a maximum PTE of 51%, exhibiting a PTE drop in the middle

of the home-cage.

In this paper, we present a new wireless neuroscience platform intended for studying correlations between physiological events and behavior during long-term experiments. It includes a WPT home-cage, a battery-less miniature neural headstage, and a motion tracking system based on a CMUcam vision system (CMUcam5 Pixy), as illustrated in Fig. 5.1 [113]. The WPT home-cage is using a new hybrid link including a TX primary coil array and segmented multi-coil resonators, as well as a split coil for the RX resonator improving power transmission across of the home-cage, and decreasing sensitivity to angular misalignments compared to previous solutions. We demonstrate the first system enabling uninterrupted simultaneous optogenetic and electrophysiology experiments with live laboratory rodents.

The paper is organized as follow : Section 5.2 presents an overview of the proposed wireless system. Section 5.3 presents the system design, and the implementation of the two main parts of the system, namely the 1) wireless neural headstage and the base station, and 2) the 4-coil resonant link. Section IV first compare the performance of the presented hybrid WPT system with two other WPT strategies implemented inside a home-cage. Then, the measured performance of the headstage, while powered up by the WPT system inside the home-cage, is presented. Finally, optogenetic and electrophysiology results obtained in an *in-vivo* experiments performed with the presented prototype are presented and

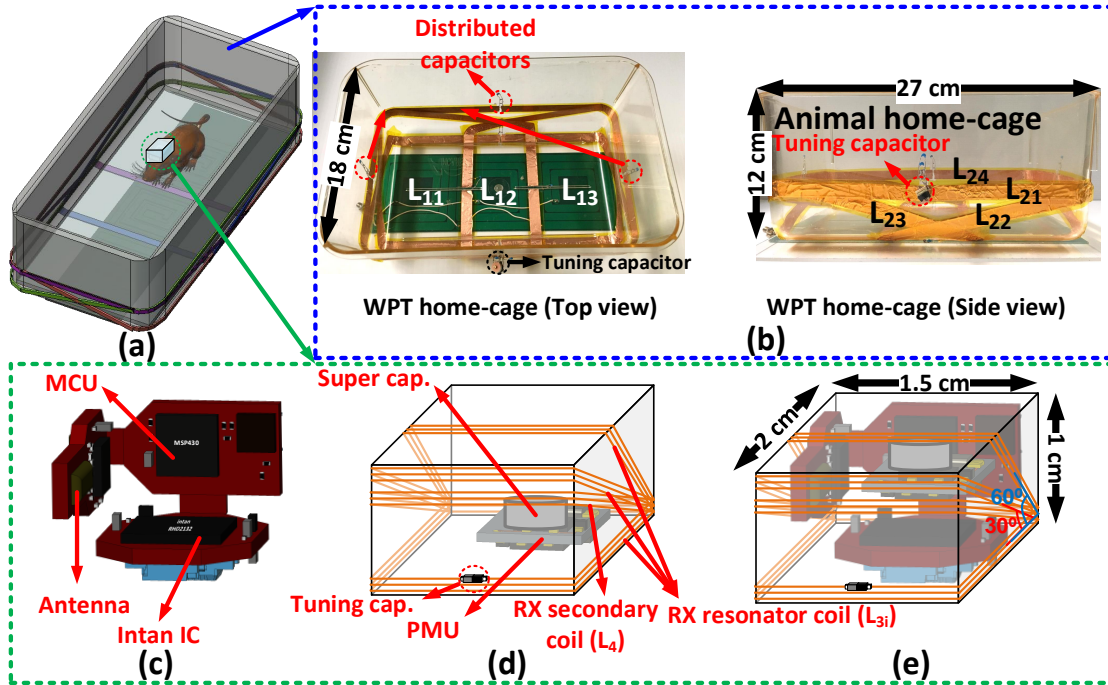


Figure 5.2 – (a) The wireless platform, (b) WPT home-cage prototype, (c) the compact folded PCB, (d) the head mountable PCB housing with split power transmission coils including the RX resonator (L_{3i}) and the RX secondary coil (L_4), and (e) the encapsulated headstage.

conclusions are drawn in [Section 5.5](#).

5.2 System Overview

As shown in [Fig. 5.2\(a\)](#), the proposed wireless platform, which was previously summarized in [113], includes two main parts : 1) a hybrid WPT system ([Fig. 5.2\(b\)](#)), and 2) a wireless neural headstage. The hybrid WPT system presented in this work, powers up the headstage implanted on the head of the animal. In contrast with previous solutions using a single TX coil at the bottom of the cage, we use an array of three coils (L11, L12, and L13), as illustrated in [Fig. 5.2\(b\)](#), for providing a uniform PTE inside the chamber, and avoid any power drop [20]. This hybrid WPT solution provides uniform PTE and can achieve longer separation distances across the home-cage, compared to previous solutions. The compact folded headstage shown in [Fig. 5.2\(c\)](#). The repeater coil of L3i is split, as shown in [Fig. 5.2\(d\)](#), to avoid any power drop due to angular misalignment during an experiment. The complete encapsulated headstage illustrated in [Fig. 5.2\(e\)](#). All parts of the system are described in details in next sections.

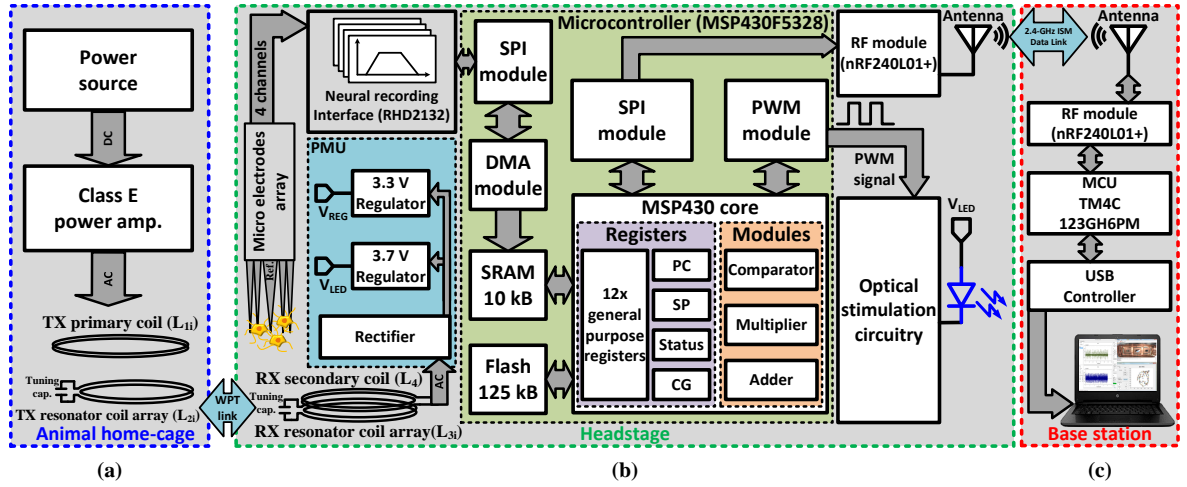


Figure 5.3 – Overall block diagram of the wireless neuroscience platform. (a) The animal home-cage consists of a power source, a class E power amplifier, TX primary parallel coil array (L_{1i}) and TX resonator segmented coil array (L_{2i}). (b) The headstage includes a split RX resonator coil array (L_{3i}), a RX secondary coil (L₄), a neural recording chip, a 2.4-GHz ISM wireless transceiver, a power management unit, a low-power MCU, an LED driver, and an optrode including one implantable fiber optic and 4 microelectrodes. (c) The base station consists of a 2.4-GHz ISM wireless transceiver, a low power MCU, a USB controller and a user interface running on a nearby computer.

5.3 System Design

Wireless Neural Headstage and Base Station

The headstage system, which was previously described in [96], is entirely built using off-the-shelf components that are mounted on a foldable flex-rigid printed circuit board (PCB) that folds around the power receiver system. Overall block diagram of the proposed neuroscience platform including animal home-cage, headstage, and base station is shown in Fig. 5.3. The printed circuit board of the headstage includes four main building blocks : 1) an RHD2132 neural recording chip from Intan Technologies, USA, 2) a 2.4-GHz nRF24L01 ISM wireless transceiver from Nordic Semiconductor, Norway, 3) a PMU and 4) a low-power MSP430F5328 MCU from Texas Instruments (TI), USA. All the recorded data will pass through an analog bandpass filter of 300 Hz-7.5 KHz in the headstage and will be transferred to the base station to be processed in computer. In this system, the neural recording interface is conditioning and digitizing the neural signals acquired from up to four microelectrodes. It can be configured to acquire local field potentials (LFP), or spikes. The RHD2132 is configured to sample the neural signals with a precision of 16 bits at 20 ksamples/s. The headstage can stimulate optically using a high-power LED driver, which can provide a maximum regulated forward current of 150 mA to accommodate various types of optogenetic LEDs.

The PCB of the headstage and the compact folded headstage are presented in Fig. 5.4(a) and 5.4(b). The head mountable PCB housing with split power transmission resonator coils of L_{3i} , and the RX coil of L_4 is shown in Fig. 5.4(c). Fig. 5.4(d) shows the wireless USB dongle which includes a wireless nRF24L01p transceiver from Nordic Semiconductors, a Cortex M4 MCU, and a USB connector. The provides a measured effective data rate of 1.4 Mbps, which allows to accomodate 4 recording channels with this system.

Hybrid WPT Home-Cage System

The resonant power transmission system uses a coil array along with segmented resonators for the TX, as well as a split resonator along with a secondary coil for the RX. On the TX side, a class E power amplifier is used to provide power to the TX including a primary coil array. The primary coil array includes 3 parallel FR4 printed coils (L_{11} , L_{12} and L_{13}), while the segmented resonators (L_{21} , L_{22} , L_{23} and L_{24}) are implemented using copper foil with 13 mm width and 80 μ m thickness placed around the animal's home-cage (Fig. 5.2(b)). The power receiver (on the headstage side) includes the secondary resonator L_{3i} , and the receiver coil L_4 (Fig. 5.2(d)) implemented using AWG wire with a diameter of 0.5 mm. As shown in Fig. 5.2(b), L_{11} , L_{12} , and L_{13} are connected in parallel and connected to the output of the power amplifier previously described in [92]. The 4 segmented TX resonators are wrapped around a standard home-cage (Dura Cage from Altdesign) with a size of 18x27 cm^2 . The resonance frequency of these resonators is optimized on the TX side by tuning the distributed capacitors of one of these resonators, as described in [21]. As illustrated in Fig. 5.2(b), each coil of the TX resonator is separated into two segments leveraging their distributed capacitors to obtain

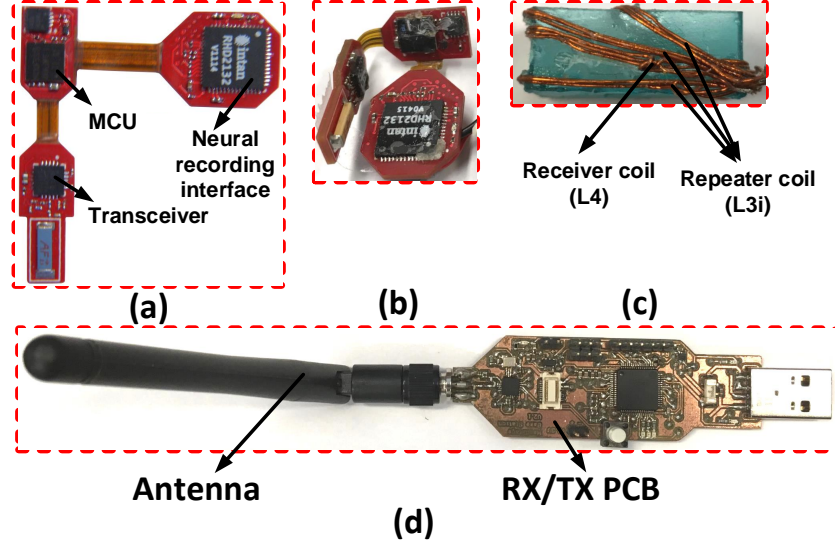


Figure 5.4 – (a) The PCB of the headstage, (b) the compact folded PCB, (c) the head mountable PCB housing with split power transmission resonator coils, and the RX coil, and (d) USB dongle including a transceiver, an antenna, and USB interface connected to the base station.

better quality factor [67]. The resonant frequency of the segmented resonators L_{2i} is adjustable using a variable capacitor connected with L_{21} . As illustrated in Fig. 5.2(d), a wire wound coil with a diameter of 1.5 cm is used as a secondary resonator (L_{3i}). The receiver coil L_4 uses a 1-cm diameter wire wound coil, which is connected to the PMU on the headstage side. The PMU circuit, which is shown in Fig. 5.2(d), includes a PG-SOT143-4 bridge voltage rectifier of from Infineon Technologies and three TLV61220 linear voltage regulators from Texas Instruments, USA with adjustable output voltages from 1.2 V to 6.5 V, maximum currents of 200 mA and SOT-23-5 package, located inside the headstage.

In [112], a strategy using the concept of virtual paralleled coils have been presented to compensate the angular misalignments on the RX side. However, the added RX resonators were designed to be mounted on the head of the animal, which increases the overall weight of the headstage. Therefore, decreasing the number of RX resonators can reduce the weight of the headstage.

This presented system uses a split RX coil to cancel the effect of the misalignment angle of the RX coil with the TX arrays located inside the home-cage. The different misalignment angles are shown in Fig. 5.5. Angle α represents the horizontal misalignment on the sides, and β represents the vertical misalignment on the back and front. According to our observations at the animal care facility, mice tend to keep their heads with a vertical angle β between 0 and 90° most of the time. Thus, we design our split coil system to cover these angles in priority.

Fig. 5.6 shows the measured PTE as a function of the angular misalignment across angles α and β , with a dedicated experimental setup to precisely vary the angles. The comparison of three configura-

tions of coil L_3 (a single L_3 , 2-split L_3 , and 3-split L_3) shows that a 3-split coil configuration has the highest PTE over the whole tested α and β angle ranges.

Fig. 5.7 shows the circuit schematic of the power TX and power RX of the WPT system, separately. The arrows indicate the coupling between the different coils of the system using different colors. The mutual coupling between L_{1i} - L_{3i} (K_{13}), L_{1i} - L_4 (K_{14}), and L_{2i} - L_4 (K_{24}) are neglected because of the large distance between the TX resonators (L_{2i}) and RX coil (L_4) and significant difference in their sizes [59]. The power transfer efficiency of the whole WPT system can be described by

$$PTE = \eta_{12} \times \eta_{23} \times \eta_{34} \quad (5.1)$$

where η_{12} , η_{23} and η_{34} are the power efficiencies between L_{1i} - L_{2i} , L_{2i} - L_3 and L_3 - L_4 , respectively. The PTE of the WPT system can be described by

$$PTE = \frac{K_{12}^2 Q_1 Q_2}{1 + K_{12}^2 Q_1 Q_2} \times \frac{2K_{23}^2 Q_2 Q_3}{(2 + K_{34}^2 Q_3 Q_4)^2} \times K_{34}^2 Q_3 Q_4 \quad (5.2)$$

where K_{12} is the mutual coupling between L_{1i} and L_{2i} , K_{23} is the mutual coupling between L_{2i} and L_{3i} , K_{34} is the mutual coupling between L_{3i} and L_4 , $Q_1 = \omega_p L_1 / R_1$, $Q_2 = \omega_p L_2 / R_2$, $Q_3 = \omega_p L_3 / R_3$ and $Q_4 = \omega_p L_4 / R_4$ [?].

Fig. 5.8 shows the 4-coil resonant link design procedure to achieve optimum PTE. The critical parameters of the inductive link are the carrier frequency (f_0), which is 13.56 Hz, the size of the animal home-cage, the size and weight of the RX side, and the expected separation distance of the RX and TX coils.

The primary TX coil array (L_{1i}) made by FR4 PCB and the TX resonator coils are implemented using the copper foil to have the best geometry of the coils in the system and the maximum PTE of the link.

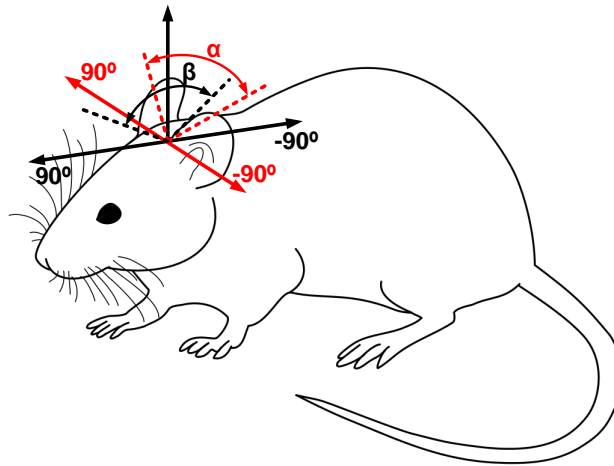


Figure 5.5 – The definition of the movement directions of the head of the mouse.

The RX resonator and receiver (L_3 and L_4) are made by the wire wounded coils using the magnet wire of AWG. The size of the standard mouse home-cage is $18 \times 27 \text{ cm}^2$. Due to the application of this system for mouse, the nominal separation distance of 4-7 cm between TX and RX been expected.

The number of turns and the spacing between the turns of the primary TX printed coil array are chosen concerning the thickness of the PCB and the number of primary coils enclosed in the TX coils array. Copper foil with a thickness of $90 \text{ } \mu\text{m}$ and a width of 13 mm has been used to implement the TX resonator coils. Each coil is separated into two segments using the distribution capacitors, [67, 94]. The most important factors on the RX side are the size and the weight of the RX unit. As can be seen in (5.2), the PTE of the system depends on the mutual coupling between L_{2i} - L_3 (K_{23}) and L_3 - L_4 (K_{34}). Assuming $K = M/\sqrt{L_T L_R}$, where, M is the mutual inductance between the TX resonators and the RX resonator (L_{2i} - L_3), L_T and L_R are the inductances of TX resonators and RX resonator, respectively. The separation distance between RX and TX resonators, the thickness of the wires of the

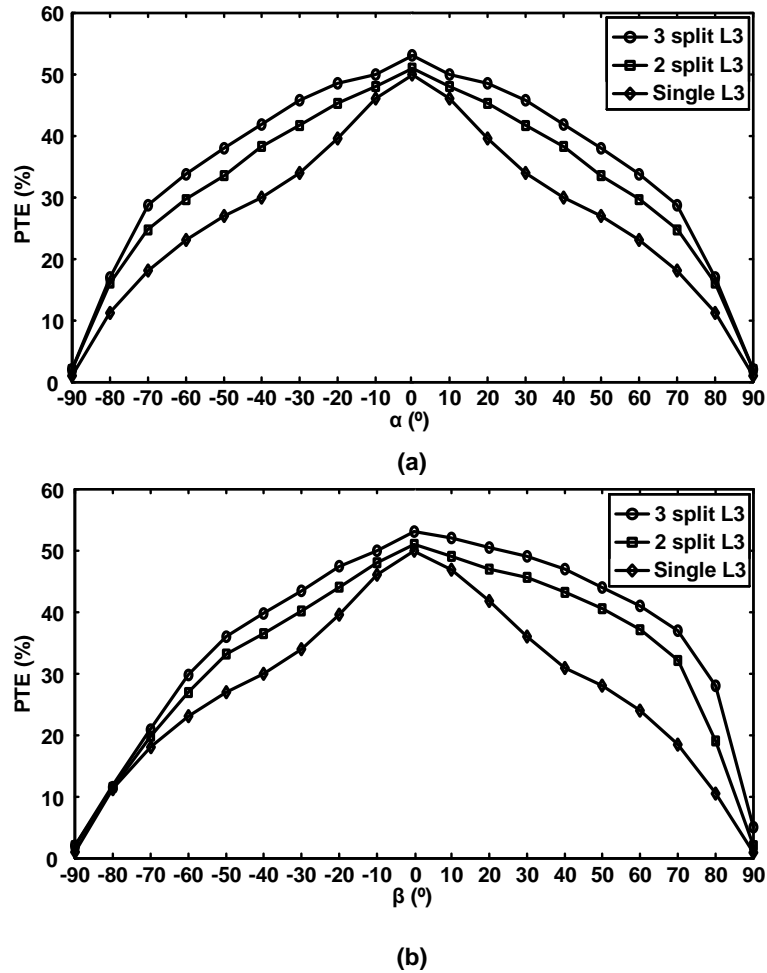


Figure 5.6 – The measured PTE of the WPTS as a function of the misalignment angle (see Fig. 5) for three L3i configurations : (a) along the angle α , (b) along the angle β .

TABLE 5.1 – SPECIFICATIONS OF THE COILS USED IN THE WPT HOME-CAGE

Parameters	L_{1i}	L_{21}, L_{24}	L_{22}, L_{23}	L_3	L_4
Inductance, L (μH)	0.64	0.85	0.77	0.8	0.6
Quality factor, Q	108	121	128	117	112
Outer diameter, d_o (cm)	9	27×19	20×18	1.2-1.8	1.8
Inner diameter, d_i (cm)	3.5	26×19	20×17	1.1-1.7	1.7
Line width, W (mm)	9	13	13	0.5	0.5
Line spacing, S (μm)	1000	-	-	-	20
Thickness, t (μm)	-	80	80	-	-
Number of turns (N)	3	1	1	9	4
Type of coil	Printed	copper foil	copper foil	Wire wound	Wire wound

receiver and the resonator, the number of turns and the diameters are chosen to optimize the PTE of the power link according to the design procedure described in [53]. The secondary 9-turns coil on the RX side, wound with three different angles allows to overcome the angular misalignment effects in the natural positions of the animal (Fig. 5.2(d)). L_3 is divided into 3 coils that are tuned using a capacitor. We empirically determined that the best PTE was achieved for an angle of 30deg between each split coils of the RX resonator, each using 3 turns. Table 5.1 summarizes the specifications of the

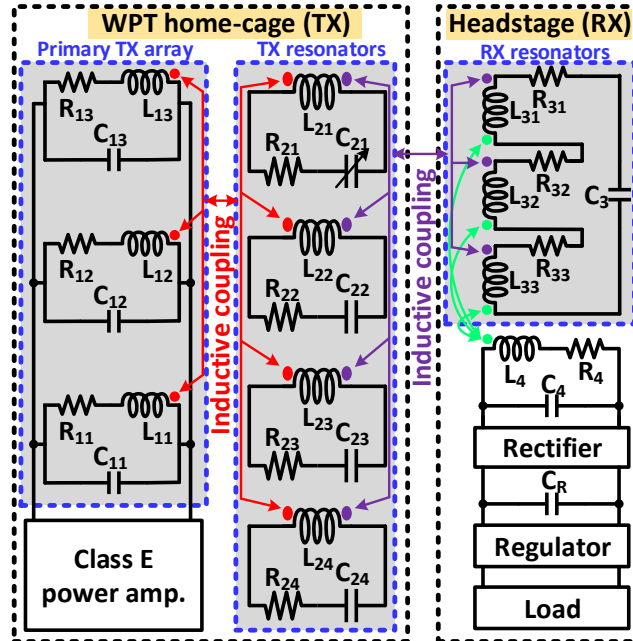


Figure 5.7 – The circuit schematic of the proposed WPT system based on a 4-coil structure including a power driver, a primary TX coil array, four TX resonators, an RX resonator, an RX secondary coil, a rectifier and a regulator.

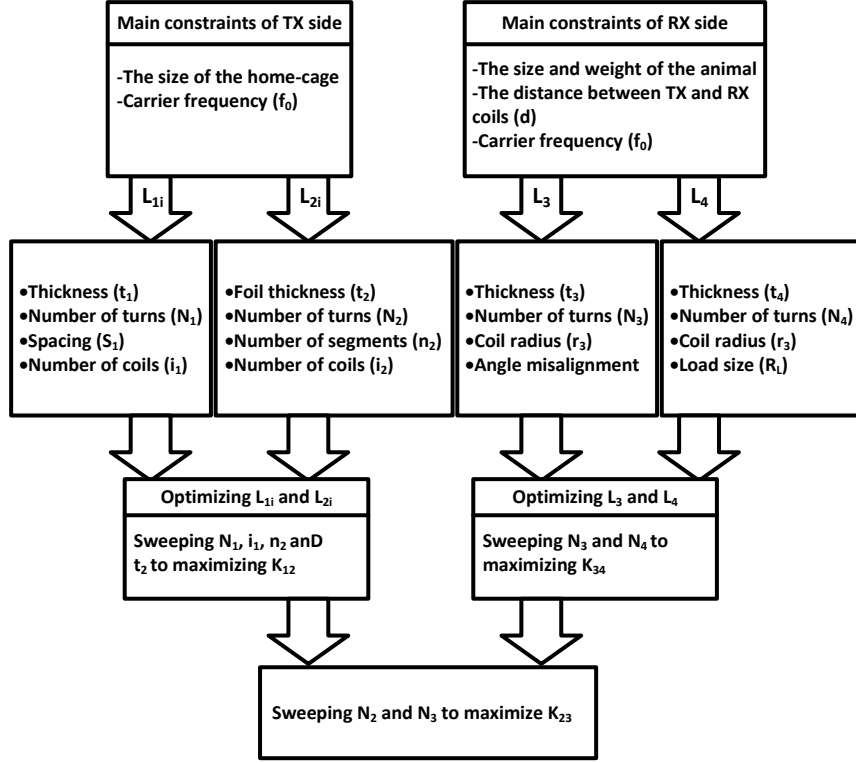


Figure 5.8 – The 4-coil resonant link optimization procedure considering the carrier of 13.56 Hz, the size of the animal home-cage, the size and weight of the RX unit, and the expected separation distance of the RX and TX coils.

implemented coils utilized in this WPT strategy depicted in Fig. 5.7.

5.4 Experimental Results

Measured Performance

Three different WPT home-cage prototypes were implemented (Fig. 5.9), tested and compared. The PTE and the power delivered to the load (PDL) of these three topologies were measured while the RX headstage was swept inside the home-cages across X-Y, at the nominal separation distance of $d=5$ cm. Separation distance d is the distance between the TX and RX coils inside the inductive WPT systems. These measurements were then used to compare the performance of these mentioned WPT systems. In these measurements, a flexible square coil of $1 \times 1 \text{ cm}^2$ and two repeaters on the RX side (described in [98]) was used for the receiver of WPTS1, and wire-wounded coils with diameters of 1 cm and split repeater coils (shown in Fig. 5.4(a)) were used for the receivers of both WPTS2 and WPTS3. The measured PTE are provided in Fig. 5.10 for all systems in 3D and across different planes, namely for Y-Z at $X=7$ cm, $X=14$ cm, and $X=22$ cm, and for X-Z at $Y=9$ cm. Topology WPTS1 (Fig. 5.9(a)), introduced in [98], uses a 5-coil inductive link. As illustrated by the measured cross sections shown in Fig. 5.10, this topology has the most uniform PTE across the whole cage. However, as shown in Table

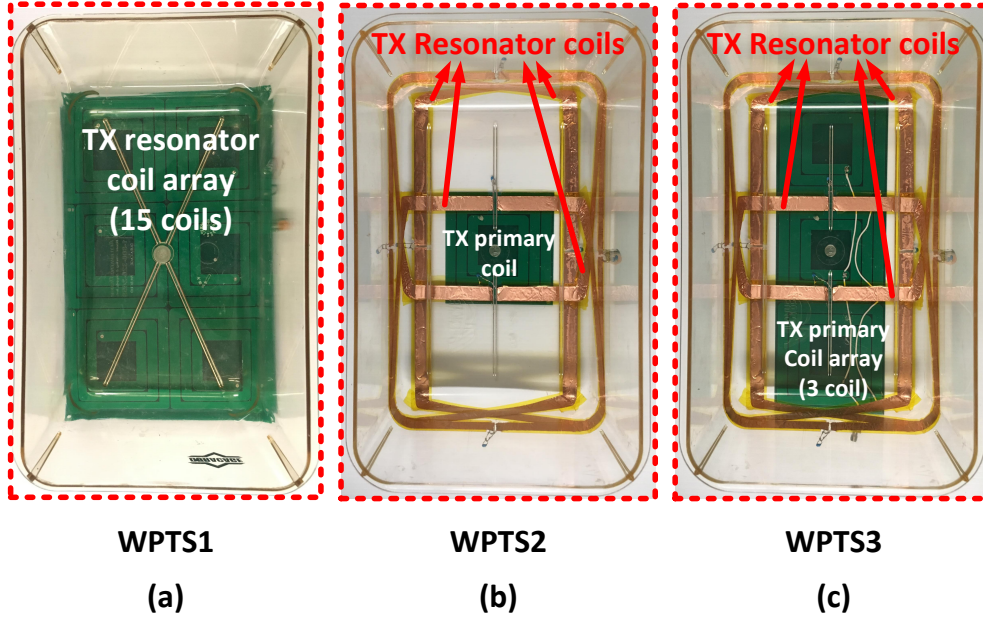


Figure 5.9 – The implemented power transmission system prototypes. (a) Power surface resonator array (WPTS1), (b) copper foil resonators using one coil as a primary TX (WPTS2) and (c) copper foil resonator using 3 TX paralleled coils as a primary TX array (WPTS3).

TABLE 5.2 – MEASURED PTE COMPARISON OF THREE WPT TOPOLOGIES

Topology	WPTS1	WPTS2	WPTS3
Minimum PTE	11%	9%	15%
Maximum PTE	14.6%	50%	53%
Average PTE	13%	25.4%	32.6%

5.2 its measured average PTE is less by 12.4% and 19.6% than the two other topologies WPTS2 and WPTS3, respectively. Topology WPTS2 (Fig. 5.9(b)) is based on the strategy introduced in [67]. As shown in Fig. 5.10, this system exhibits a significant power drop of 41% at the center compared to the edges. As can be seen in Table 5.2, topology WPTS3 introduced in this paper (Fig. 5.9(c)) represents an improvement of 19.6% in the average PTE, compared to WPTS1, and an improvement of 7.2%, compared to WPTS2. It is critical to avoid any significant drop in the PTE at the center of the hime-cage compared to the edges in this application. Otherwise, it would drastically decrease the PDL and could interrupt the operation of the headtsage, preventing any long-term in-vivo experiment. WPTS3 has a PTE drop of 38% at the center compared to the edges, which represents an improvement of 3% compared to WPTS2. It also has the best PTE and PDL in average compared to WPTS1 and WPTS2. It has a measured PDL of 82 mW, which is significantly higher than the measured PDL of WPTS1 and WPTS2, which are of 64 mW and 67 mW, respectively. As can be seen in Fig. 5.10, the PTE of the proposed WPTS3 is always higher than for the two others systems.

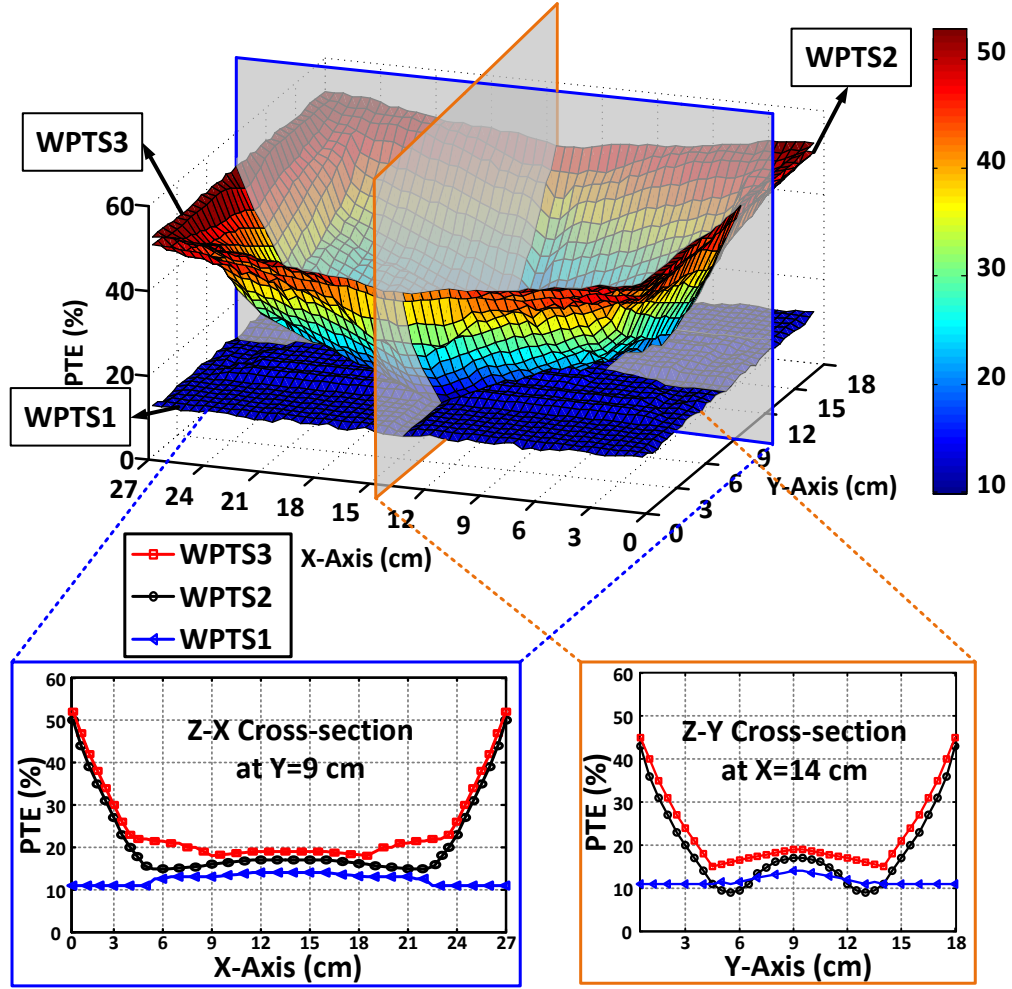


Figure 5.10 – The measured PTE when the receiver is swept inside the cage across the X-Y at a distance of $d=5$ cm.

Table 5.3 summarizes the performance of the proposed WPT system compared with the state-of-the-art, using the FOM introduced in [98] :

$$FOM = \frac{d}{d_{or}} \times PTE \times PDL \times Size \quad (5.3)$$

The FOM is based on these parameters : the separation distance between the TX and RX coils (d); the size of the home-cage (Size) and the outer diameter of the RX coil (d_{or}); and the PDL and the PTE of the system. As shown in Table 5.3, topology WPTS1 (Fig. 5.9(a)) has a measured PDL of 64 mW and a FOM of 2. Topology WPTS2, which is based on [67] (Fig. 5.9(b)), has a measured PDL of 67 mW, and a FOM of is 10, while the proposed topology WPTS3 (Fig. 5.9(c)) has a FOM of 15.5 and a PDL of 82 mW. The proposed WPT home-cage system presents the best measured performance, including for the average PTE, the minimum PTE, and the PDL, as indicated in Table

TABLE 5.3 – PERFORMANCE SUMMARY AND COMPARISON OF PROPOSED WPTS WITH THE STATE OF THE ART

References	[67]	[98]	[64]	[92]	[65]	[66]	This work (Single TX coil (L_1))	This work (TX coil array (L_{1i}))
Wireless link	4-coil	5-coil	4-coil	4-coil	2-coil	4-coil	4-coil	4-coil
Size (cm^2)	24×46	18×27	50×60	27×27	18×34	29×20	18×27	18×27
Separation distance d (cm)	0-17	3-5	12	1-15	3	1.5	0-12	0-12
Receiver diameter d_{or} (cm)	2.2	1	4	2	1.2	2	1	1
Average PTE	18%	13%	19.6%	20%	17%	25.9%	25.4%	32.6%
Minimum PTE	14%	11%	5%	-	4.7%	-	9%	15%
PDL (mW)	65	64	20	36	1.2	43	67	82
FOM	10	2	3.51	4	0.03	0.5	10	15.5

5.3. Since the amount of power transmitted through the inductive link is limited at the primary by the efficiency and the output energy of the power amplifier, a significant drop in the PTE across the WPT-home cage could interrupt the operation of the headstage during the *in-vivo* experiments. Hence, it is desirable that the WPT system provides good power transmission uniformity across the whole cage. Using a parallel coil array in this system, in addition to 4 segmented copper foil coils, as a resonator array, improves the PTE uniformity owing to the PTE drop of 38%, which represents an improvement of 10% compared to the other WPT home-cage topologies. Even though the outer diameter of the RX coil (d_{or}) is of only 1 cm, the proposed WPT home-cage allows for a competitive value of the separation distance (d) compared to the state-of-the-art. Then, the performance of the encapsulated headstage has been measured while powered up through the proposed WPT home-cage. Table 5.4 summarizes the measured characteristics of the headstage compared with the state-of-the-art.

All the systems presented in Table 5.4 can be powered up through an inductive link, and their performance were measured within freely moving animal experiments. Among these systems, only the headstage presented in this paper provides simultaneous optical stimulation and electrophysiological recording. The headstages proposed in [112], [114] and [115] include an electrical stimulator and an optical stimulator, respectively but do not include any recording electronics, resulting in lower power consumption. In the proposed system, a regulated output current of 40 mA is provided to the LED driver circuitry by the power link, which allows to power up the fiber-coupled LED (LB-G6SP from OSRAM Opto Semiconductors Inc.), while providing enough light power ($> 1 \text{ mW/mm}^2$) at the tip of the optical fiber to activate the ChR2 light sensitive neurons of the transgenic mouse [102]. The output optical power is measured using a power and energy meter console of PM100D from THORLABS.

TABLE 5.4 – PERFORMANCE SUMMARY AND COMPARISON OF THE WIRELESS HEAD-STAGE WITH THE STATE OF THE ART

Parameters	[112]	[114]	[115]	This work
Size (cm^3)	$2 \times 2.2 \times 2$	$1 \times 2.5 \times 1$	$0.07 \times 0.38 \times 0.6$	$1.5 \times 1.5 \times 1$
Weight(grams)	7	0.05	0.016	4.1
Stim. channels (Opt./Elec.)	0/1	1/0	1/0	1/0
Rec. channels	0	0	0	4
Optical power (mW/mm ²)	NA	1-20	10	~3.5
Power dis. (With stim.)	42 mW	15.7 mW	NA	62 mW
Power dis. (Without stim.)	NA	NA	NA	43 mW
Input noise (μV_{rms})	NA	NA	NA	2.4 (300Hz-3kHz)
Radio link	NA	NA	NA	2.4-GHz ISM/~1 Mbps
Inductive receiver	5-coil wire-wounded	1-coil wire-wounded	1-coil flexible	2-coil wire-wounded
Freely moving demonstration	YES	YES	YES	YES

in-vivo Results

To test the system's performance in a realistic setting, *in-vivo* experiments were conducted with a freely moving laboratory mouse. Fig. 5.11(a) shows the *in-vivo* experimental setup including the power source, the class E power amplifier, the WPT home-cage, the motion tracking system, and the base station including a dongle transceiver and a laptop computer. The headstage is attached to an implanted module which is fixed on the head of the animal (Fig. 5.11(b)). The headstage can be simply detached from the implanted module after any laboratory experiment. The implanted module includes a Molex connector mounted on a PCB, and a custom optrode manufactured by Doric Lenses, Canada. This optrode consists of an LED-coupled (LB G6SP from OSRAM Opto SemiConductors) 1.5 mm long optic fiber (250 μm diameter and NA : 0.66) and four Tungsten microelectrodes of 25, 50 and 75 μm diameter and 1400 to 1800 μm long, packaged inside a tiny polyimide tubing with a separation distance of 125 μm between the optic fiber and electrodes

Surgical procedure

A transgenic mouse (Thy1-COP4/EYFP) line 18, Jackson Laboratory [116] was used for this study (28-30 weeks old; 25-30 g) which was conducted with prior approval from the Institutional Animal

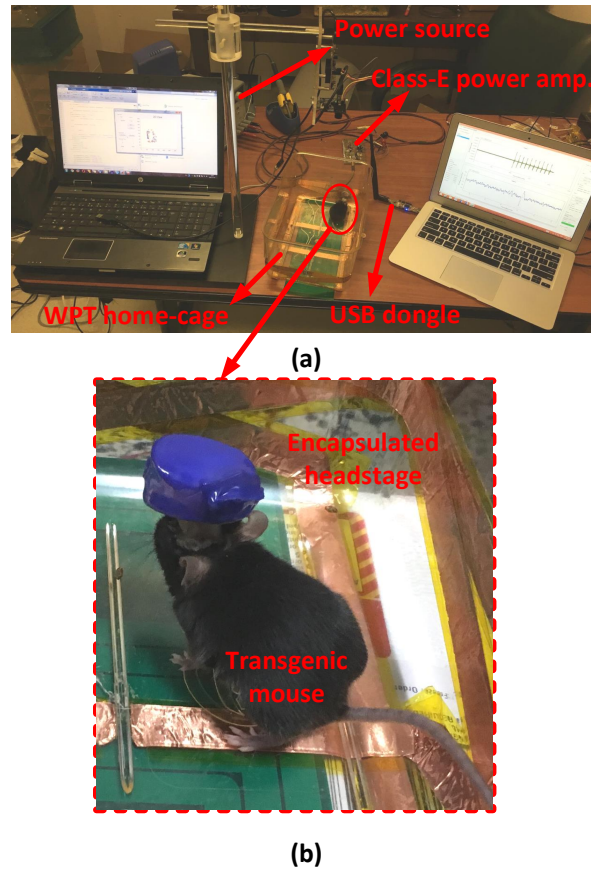


Figure 5.11 – (a) Experimental measurement setup. (b) Implanted headstage on the head of a ChR2 transgenic mouse.

Care and Use Committee (IACUC) at CERVO Brain Research Center of Laval University to test the functionality of this wireless platform. The animal was anesthetized with a constant flow of 2% isoflurane, and the depth of the anesthesia is assessed before the surgery by the respiratory rate and toe pinch reflexes. The animal was placed on a temperature controlled heating pad within a stereotaxic apparatus. The skin on top of the skull was removed to facilitate the adhesion of the implant module, and the surface of the skull was cleaned with 30% H_2O_2 solution before drilling. A large hole was drilled in the desirable coordinates (0.70 mm caudal and 0.3 mm lateral (left) from bregma), and the wireless implant was slowly lowered 1.80 mm into the brain ($4 \mu\text{m/s}$; maximum DV coordinated are measured for the longest electrode). Once in place, the implant was secured to the skull with C&B-METABOND® Parkell dental cement. The animal was left to recover at least 72h prior to any conducting recordings.

Freely moving extracellular recordings

Before performing the recordings, the animal was slightly anesthetized with 2% isoflurane in order to connect the headstage to the implanted module. After the animal fully recovered from the anesthesia, freely moving recordings were performed for 10 to 15 min. The recordings analysed for the present study were extracted from the signal collected by the 50 μm probes (0.3 MOhm). Two series of tests were conducted with the system to assess its performances. First, we recorded the basal neuronal activity without any light stimulation.

The recorded signals are then passed through a digital notch filter with a central rejection frequency of 3333 Hz and a stopband of 120 Hz in the interface program of the base station. The recorded spontaneous activity is shown in (Fig. 5.12). Two recorded spikes clusters with an amplitude of 200 μV and 150 μV , respectively are shown in inset. Secondly, extracellular recordings of the anterior

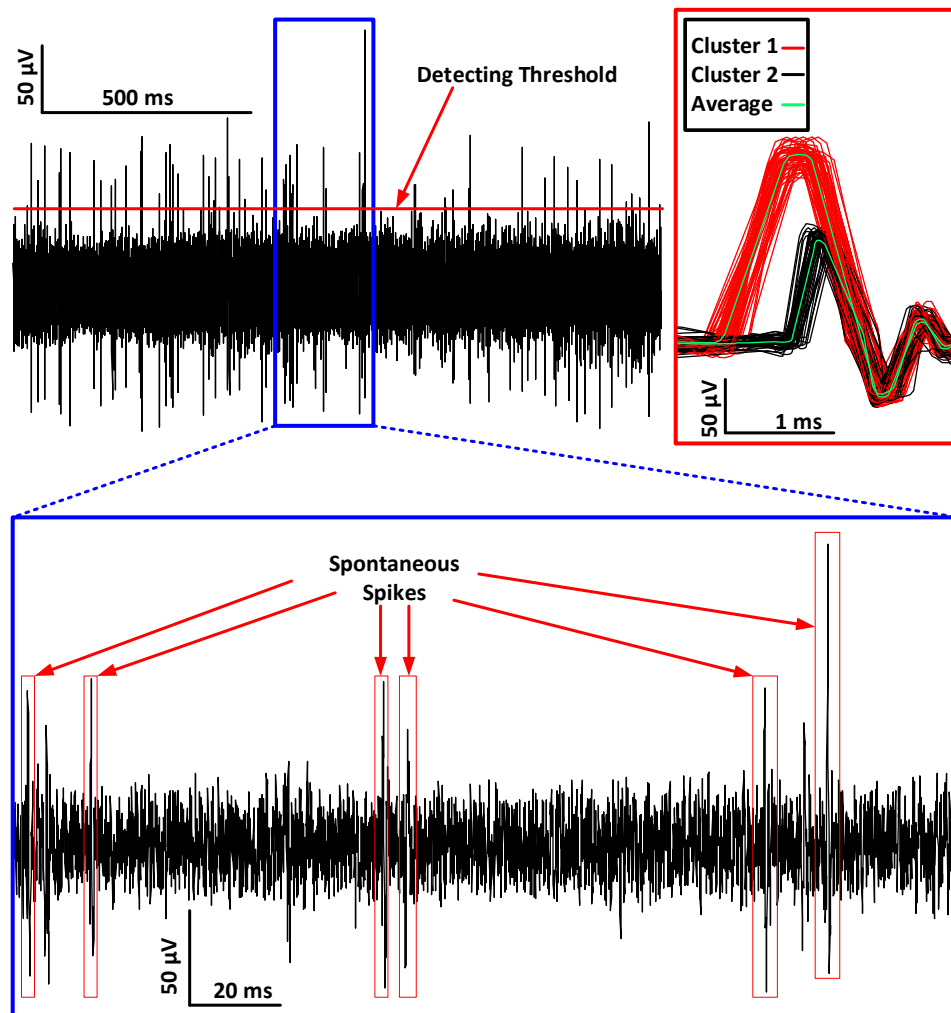


Figure 5.12 – Recorded spontaneous neural activity without any optical stimulation.

cingulate cortex in response to ChR2 activation by local light activation were conducted. Fig. 5.13 shows the voltage variation across the Capacitor C_R , in the PMU of the headstage, across time during the *in-vivo* testing. As shown in Fig. 5.14 the stimulation consisted of a 40mA, 10ms long LED light stimuli at 0.5 Hz (total duration 2s). The optical stimulation resulted in a multi-unit action potential response with an amplitude up to 1.1 mV.

5.5 Conclusion

In this paper, simultaneous optogenetics and electrophysiological recording results are presented for the first time in a freely moving animal using a fully wireless neuroscience platform prototype enabling uninterrupted live experiments. This platform includes a real-time motion tracking system, a WPT home-cage and a wireless optogenetic headstage. The motion tracking system provides a 2D motion tracking diagram of the animal movement inside the home-cage. The WPT home-cage system has been implemented using a new hybrid resonant link with a carrier frequency of 13.56 MHz. A parallel coil array is used for the TX primary coil, while 6 segmented copper foil coils mutually in parallel using distributed capacitors, are used as TX resonators. On the headstage side, the power RX uses a small wire wound RX resonator coil with a diameter of 1.5 cm and a secondary RX coil with a diameter of 1 cm, providing PDL of 82 mW to the headstage. The headstage includes 4 recording channels and 1 optical stimulation channel and wirelessly communicates with a wireless USB dongle through a short-range 2.4-GHz ISM wireless link. The measurement results show an average PTE of 32.6% for the WPT system at a nominal distance of $d = 5$ cm, with a maximum and minimum of 53% and 15% from $d = 0$ to 12 cm along the Z axis, respectively. The proposed WPT home-cage system presents the best measured performance, including for the average PTE, the minimum PTE, and the

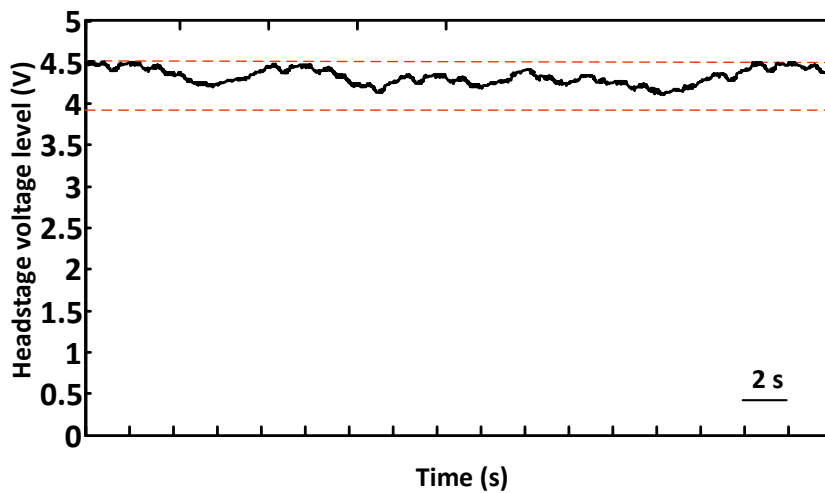


Figure 5.13 – Measured voltage retrieved by the power RX on the headstage side (voltage across capacitor C_R).

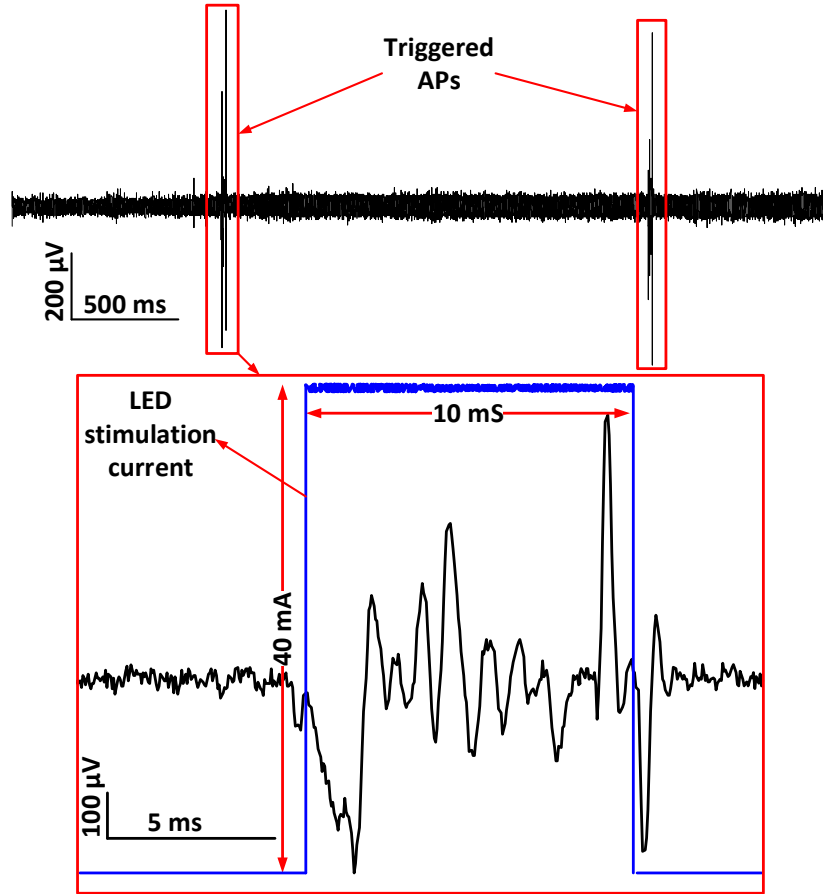


Figure 5.14 – The experimental results showing extracellular recordings in the brain of a ChR2 mouse in response to local optogenetic light activation of 10 ms with a period of 2 s. APs with amplitude of up to 1.1 mV were evoked by the light activation.

PDL compared to previous solutions. Three different WPT home-cage prototypes were implemented, tested and compared in this paper and the proposed system represents an improvement of 7.2% of average PTE and its PDL is significantly higher than the measured PDL of two other topologies. This prototype plays a key role to enable the study of brain activity at unprecedented scales and in a large variety of subject states such as awake, behaving, freely-moving, resting-state, and asleep conditions with the laboratory mouse.

Chapitre 6

Discussion and conclusion

Discussion

The main goal of this PhD was to provide and design a highly efficient WPT system for low-power implantable devices in optogenetic applications. Over the past decade, different WPT systems have been designed to avoid battery use and enable uninterrupted experiments with live animals. One of the most important challenges to WPT systems is accomplishing the power consumption. In this PhD, a novel level shifter was presented to decrease the power of the implantable system on a chip using a shifting capacitor. This circuit has been proposed and published in *IEEE ISCAS* conference in 2015. The proposed LS circuit was updated to reduce the static power consumption and has been fabricated in 0.18- μm TSMC CMOS process. Then, this idea was published in the journal of *IEEE Transactions on Circuits and Systems-I* (2016), which is among the highest-level transactions in the electronic field. The measurement results show that it significantly improves propagation delays with an acceptable power consumption compared to the other reported level shifters. It presents a transition delay of 29 ns for an input pulse signal of 0.4 V at a frequency of 500-kHz. In these typical conditions, the dynamic power consumption of the proposed circuit is of 61.5 nW, and the static power dissipation is 330 pW, occupying only 229.5 μm^2 die area.

This PhD also included designs for three different WPT home-cages to power up the implantable devices and headstages for neural recording and optical stimulation. The first wireless power transfer (WPT) system introduced in [Chapter 3](#), is a new 5-coil inductive power link using an array topology is utilized for powering up the proposed implantable system with a thin flexible implanted receiver coil. In this link, a primary coil connected to the power amplifier, a multi-coil array as a TX resonator and a wire wounded resonator coil are located outside the body, while a thin double-sided coil including a flexible resonator coil and a receiver coil, is implanted inside the body. The measured PTE of the 5-coil link inside the home-cage at $d=4$ cm is of 12.3% with a PDL of 35.5 mW. This system can provide the power for the low power implantable system on a chip for deep brain recording applications. The paper related to this system has been published in *IEEE ISCAS* conference in 2017.

The second WPT system introduced in [Chapter 4](#) uses a new hybrid parallel power transmitter coil array and segmented multi-coil resonators to achieve high PTE and deliver high power across distances as high as 20 cm. The multi-coil power receiver (RX) uses an RX coil with a diameter of 1 cm and a resonator coil with a diameter of 1.5 cm. The WPT home-cage average power transfer efficiency is 29.4%, at a nominal distance of 7 cm, for a power carrier frequency of 13.56-MHz. It has maximum and minimum PTE of 50% and 12% along the Z axis and can deliver a constant power of 74 mW to supply a miniature neural headstage for optogenetic applications. Also, an implantable device integrated into 0.18- μm TSMC CMOS process has been introduced which includes 64 recording channels, 16 optical-stimulation channels, temperature sensor, transceiver and Power Management Unit (PMU). The performance of the proposed hybrid power link has been measured for both the neural headstage and integrated system powered up inside the home-cage. The proposed WPT system has been published in *IEEE ISCAS* conference in 2018.

The angular misalignment of the head of the animal is one of the most important factors that reduce the PTE of the proposed hybrid WPT system during the freely moving animal test. We updated the hybrid WPT system considering this effect in [Chapter 5](#). The updated WPT home-cage uses the same hybrid power TX based on a parallel coil array and a segmented multi-coil resonators on the TX side and, the multi-coil power receiver uses an RX coil with a diameter of 1.0 cm and a new split resonator coil with a diameter of 1.5 cm, which is robust against angular misalignment. The WPT home-cage average power transfer efficiency is 32.6%, at a nominal distance of 5 cm, and at a power carrier frequency of 13.56 MHz, which represents an improvement of 7.2% over previous WPT home-cage systems. It has maximum and minimum PTE of 53% and 15% and can deliver a constant power of 82 mW to supply the miniature neural headstage. We demonstrated the performance of the system within an *in-vivo* experiments with a freely moving Chr2 mouse. Simultaneous optogenetic stimulation and electrophysiological recordings with a batteryless system are reported for the first time with a freely moving mouse. Electrophysiological activity was recorded while delivering optogenetic stimulation in the Anterior Cingulate Cortex (ACC) of the mouse. The paper related to this system and measurement results has been submitted to *IEEE Transaction on Biomedical Circuits and Systems*.

The topologies proposed in this thesis can be used in different biomedical applications. The proposed level shifter can be used in any system on a chip to reduce the power consumption of the system and provide a low-power design for many different applications in biomedical engineering.

The different proposed methodologies for the inductive power links used for neural recording and stimulation can also be used in different biomedical applications. These methods can also be used to extend and optimize the powering up different implantable systems on a chip or mountable discrete circuit on the head of the animal.

The performance of the last WPT hybrid link introduced in this thesis in a realistic setting, *in-vivo* experiments were conducted with a freely moving laboratory mouse. This system can be used for different transgenic mice for the long-term experiments. Also, it can be extended to larger animal

home-cages by the scalability of the proposed system to provide the freely moving animal test for several mice, simultaneously.

Conclusion

Chapter 1 introduced available implantable devices for freely moving animal application, current low-power design techniques for the implantable system on chip and WPT systems that use inductive links. A review of state-of-the-art design techniques and the main considerations of the different inductive links was introduced as well. Also, I presented the design rules, the most important challenges, the motivation of the project, the possible solutions for low-power implantable devices, and a new WPT system for optogenetics application.

In **Chapter 2**, a new level-shifting circuit based on a novel topology using a level-shifting capacitor approach was proposed. In this new strategy, a capacitor was charged to supply a higher voltage at the gate of the higher supply voltage (V_{DDH}) inverter when needed, which enabled coverage of a wider range of conversion voltages and higher operating frequencies while achieving ultra-low power and shorter propagation delays. The measurement results show that the proposed LS has one of the smallest reported energy per transitions (E_{tr}), delays, and static power (P_S) measures among recently published designs.

In **Chapter 3**, a novel 5-coil inductive power link was presented. The proposed structure used the overlapped printed coil as a power surface in the transmitter side. This power transfer system used a $1 \times 1 \text{ cm}^2$ double-sided printed coil in the receiver side. A full-duplex transceiver was powered up inside the chamber sharing a single antenna between the transmitter and receiver to reduce implant size and complexity. The high efficiency of the system was verified by measurement results presented in this chapter and was compared with previously published works for two different situations of a single resonator and power surface.

Chapter 4 introduced a new wireless neuroscience platform including a WPT home-cage, an implantable recording, and stimulation system on a chip that included PMU, a battery-less miniature neural headstage, and a motion tracking system. A 4-coil link WPT system built around a standard home-cage was used to power up the headstage. Thanks to the shape and number of the mutually paralleled transmitter resonators, a longer separation distance between the receiver and transmitter was achieved. The WPT home-cage system with a hybrid resonant link provided a more uniform PTE using an array of printed coils as a transmitter primary coil compared to previous solutions. The implantable system included 64 recording channels, 16 optical stimulation channels, a temperature sensor, a transceiver, and PMU was powered up inside the WPT home-cage. The headstage, which was wirelessly powered up by the WPT home-cage, included four neural recording channels and one high-power optical stimulation channel for optogenetics. The motion tracking system consisted of a camera, a microcontroller unit (MCU) and a Matlab user interface providing a 2D tracking diagram in real-time of the position of the animal.

In **Chapter 5**, the final chapter, a smart neuroscience platform was presented for enabling uninterrupted optogenetic experiments with live laboratory rodents. An extended strategy of the multicoil inductive link topologies using copper foil and a wire-wounded receiver coil was used to provide WPT system insensitive to angular misalignments. The inductive link optimization and a comparison of this PTE and its performance with the previously published systems (by defining a figure of merit) was also provided in this chapter. Two series of tests were conducted with the system to assess its performances. First, the basal neuronal activity was recorded without any light stimulation. Secondly, extracellular recordings of the anterior cingulate cortex in response to ChR2 activation by local light activation were conducted.

Publication List

Journals :

1. **E. Maghsoudloo**, M. Rezaei, M. Sawan, and B. Gosselin, "A High-Speed and Ultra Low-Power Subthreshold Signal Level Shifter," in *IEEE Trans. Circuits Syst. I*, vol.64, no.5, pp. 1164-1172, May 2017.
2. M. Rezaei, **E. Maghsoudloo**, C. Bories, Y. De Koninck and B. Gosselin, "A Low-Power Current-Reuse Analog Front-End for High-Density Neural Recording Implants," in *IEEE Trans. Biomed. Circuits Syst.*, vol. 12, no. 2, pp. 271-280, April 2018.
3. **E. Maghsoudloo**, G. Gagnon-Turcotte, Z. Rezaei, C. Bories, I. Keramidis, Y. De Koninck, and B. Gosselin, "A Wireless Neuroscience Platform for Uninterrupted Optogenetics and Electrophysiology Recording in Live Animals," in *IEEE Trans. Biomed. Circuits Syst.* (Submitted, Under review, 2018).

Conferences :

1. **E. Maghsoudloo**, M. Rezaei, M. Sawan, and B. Gosselin, "A Power-Efficient Wide-Range Signal Level-Shifter," *IEEE 13th International New Circuits and Systems Conference (NEWCAS)*, Grenoble, pp. 1-4, June 2015.
2. M. Rezaei, **E. Maghsoudloo**, M. Sawan, and B. Gosselin, "A Novel Multichannel Analog-to-Time Converter Based on a Multiplexed Sigma Delta Converter," *IEEE 13th International New Circuits and Systems Conference (NEWCAS)*, Grenoble, pp. 1-4, June 2015.
3. **E. Maghsoudloo**, M. Rezaei, M. Sawan, and B. Gosselin, "A New Charge Balancing Scheme for Electrical Microstimulators Based on Modulated Anodic Stimulation Pulse Width," *IEEE International Symposium on Circuits and Systems (ISCAS)*, Montreal, QC, 2016, pp. 2443-2446.
4. M. Rezaei, **E. Maghsoudloo**, M. Sawan, and B. Gosselin, "A 110-nW in-channel sigma-delta converter for large-scale neural recording implants," *IEEE Engineering in Medicine and Biology Society (EMBC)*, Orlando, FL, pp. 5741-5744, 2016.
5. **E. Maghsoudloo**, M. Rezaei, and B. Gosselin, "A Wirelessly Powered High Speed Transceiver for High-Density Bidirectional Neural Interfaces," *IEEE International Symposium on Circuits and Systems (ISCAS)*, Baltimore, MD, 2017, pp. 1-4 (Invited paper).

6. G. Gagnon-Turcotte, **E. Maghsoudloo**, Y. Messaddeq, Y. De Koninck, and B. Gosselin, "A Miniature Wireless Photostimulator for Optogenetics with Live Animals," *IEEE Conf. NEWCAS* 2017, pp. 193-196.
7. M. Rezaei, **E. Maghsoudloo**, Y. De Koninck, and B. Gosselin, "A Fully Implantable Multichip Neural Interface with a New Scalable Current-Reuse Front-End," in *IEEE Conf. NEWCAS*, 2017, pp. 365-368.
8. M. Desjardins, M. Roudjane, Y. Ledemi, G. Gagnon-Turcotte, **E. Maghsoudloo**, G. Fillion, B. Gosselin, and Y. Messaddeq, "Development of electro-conductive silver phosphate-based glass optrodes for in vivo optogenetics," *Proc. SPIE 10482, Optogenetics and Optical Manipulation*, February 2018.
9. **E. Maghsoudloo**, G. Gagnon-Turcotte, Z. Rezaei, and B. Gosselin, "A Smart Neuroscience Platform with Wireless Power Transmission for Simultaneous Optogenetics and Electrophysiological Recording," *IEEE International Symposium on Circuits and Systems (ISCAS)*, Florence, Italy, 2018, pp. 1-5.

Bibliographie

- [1] L. R. Hochberg, M. D. Serruya, G. M. Friehs, J. A. Mukand, M. Saleh, A. H. Caplan, A. Branner, D. Chen, R. D. Penn, and J. P. Donoghue, “Neuronal ensemble control of prosthetic devices by a human with tetraplegia,” *Nature*, vol. 442, no. 7099, p. 164, 2006.
- [2] L. R. Hochberg, D. Bacher, B. Jarosiewicz, N. Y. Masse, J. D. Simeral, J. Vogel, S. Haddadin, J. Liu, S. S. Cash, P. van der Smagt, *et al.*, “Reach and grasp by people with tetraplegia using a neurally controlled robotic arm,” *Nature*, vol. 485, no. 7398, p. 372, 2012.
- [3] C. E. Vargas-Irwin, G. Shakhnarovich, P. Yadollahpour, J. M. Mislow, M. J. Black, and J. P. Donoghue, “Decoding complete reach and grasp actions from local primary motor cortex populations,” *Journal of neuroscience*, vol. 30, no. 29, pp. 9659–9669, 2010.
- [4] A. Afshar, G. Santhanam, M. Y. Byron, S. I. Ryu, M. Sahani, and K. V. Shenoy, “Single-trial neural correlates of arm movement preparation,” *Neuron*, vol. 71, no. 3, pp. 555–564, 2011.
- [5] J. E. O’Doherty, M. A. Lebedev, P. J. Ifft, K. Z. Zhuang, S. Shokur, H. Bleuler, and M. A. Nicolelis, “Active tactile exploration using a brain–machine–brain interface,” *Nature*, vol. 479, no. 7372, p. 228, 2011.
- [6] W. Truccolo, J. A. Donoghue, L. R. Hochberg, E. N. Eskandar, J. R. Madsen, W. S. Anderson, E. N. Brown, E. Halgren, and S. S. Cash, “Single-neuron dynamics in human focal epilepsy,” *Nature neuroscience*, vol. 14, no. 5, p. 635, 2011.
- [7] “Neuroport, blackrock microsystems.” <http://www.blackrockmicro.com/content.aspx?id=11>.
- [8] J. L. Collinger, B. Wodlinger, J. E. Downey, W. Wang, E. C. Tyler-Kabara, D. J. Weber, A. J. McMorland, M. Velliste, M. L. Boninger, and A. B. Schwartz, “High-performance neuroprosthetic control by an individual with tetraplegia,” *The Lancet*, vol. 381, no. 9866, pp. 557–564, 2013.
- [9] H. Gao, R. M. Walker, P. Nuyujukian, K. A. Makinwa, K. V. Shenoy, B. Murmann, and T. H. Meng, “Hermese : A 96-channel full data rate direct neural interface in 0.13 μ m cmos,” *IEEE Journal of Solid-State Circuits*, vol. 47, no. 4, pp. 1043–1055, 2012.

- [10] R. R. Harrison, R. J. Kier, C. A. Chestek, V. Gilja, P. Nuyujukian, S. Ryu, B. Greger, F. Solzbacher, and K. V. Shenoy, "Wireless neural recording with single low-power integrated circuit," *IEEE transactions on neural systems and rehabilitation engineering*, vol. 17, no. 4, pp. 322–329, 2009.
- [11] M. Rizk, C. A. Bossetti, T. A. Jochum, S. H. Callender, M. A. Nicolelis, D. A. Turner, and P. D. Wolf, "A fully implantable 96-channel neural data acquisition system," *Journal of neural engineering*, vol. 6, no. 2, p. 026002, 2009.
- [12] M. Yin and M. Ghovanloo, "A low-noise clockless simultaneous 32-channel wireless neural recording system with adjustable resolution," *Analog Integrated Circuits and Signal Processing*, vol. 66, no. 3, pp. 417–431, 2011.
- [13] T. A. Szuts, V. Fadeyev, S. Kachiguine, A. Sher, M. V. Grivich, M. Agrochão, P. Hottowy, W. Dabrowski, E. V. Lubenov, A. G. Siapas, *et al.*, "A wireless multi-channel neural amplifier for freely moving animals," *Nature neuroscience*, vol. 14, no. 2, p. 263, 2011.
- [14] G. Fritsch, "Über die elektrische erregbarkeit des grosshirns," *Arch, anat. Physiol. Wiss. Med.*, vol. 37, pp. 300–332, 1870.
- [15] L. Geddes and J. Bourland, "Tissue stimulation : theoretical considerations and practical applications," *Medical and Biological Engineering and Computing*, vol. 23, no. 2, pp. 131–137, 1985.
- [16] J. Song, B. Abou-Khalil, and P. Konrad, "Intraventricular monitoring for temporal lobe epilepsy : report on technique and initial results in eight patients," *Journal of Neurology, Neurosurgery & Psychiatry*, vol. 74, no. 5, pp. 561–565, 2003.
- [17] N. Bhadra and P. H. Peckham, "Peripheral nerve stimulation for restoration of motor function," *Journal of clinical neurophysiology*, vol. 14, no. 5, pp. 378–393, 1997.
- [18] M. Schuettler, M. Franke, T. B. Krueger, and T. Stieglitz, "A voltage-controlled current source with regulated electrode bias-voltage for safe neural stimulation," *Journal of neuroscience methods*, vol. 171, no. 2, pp. 248–252, 2008.
- [19] A. Hadzic, J. D. Vloka, R. E. Claudio, N. Hadzic, D. M. Thys, and A. C. Santos, "Electrical nerve localization effects of cutaneous electrode placement and duration of the stimulus on motor response," *Anesthesiology : The Journal of the American Society of Anesthesiologists*, vol. 100, no. 6, pp. 1526–1530, 2004.
- [20] S. Plevnik, D. B. Vodušek, P. Vrtačnik, and J. Janež, "Optimization of pulse duration for electrical stimulation in treatment of urinary incontinence," *World Journal of Urology*, vol. 4, no. 1, pp. 22–23, 1986.
- [21] P. E. Crago, P. H. Peckham, J. T. Mortimer, and J. P. Van Der Meulen, "The choice of pulse duration for chronic electrical stimulation via surface, nerve, and intramuscular electrodes," *Annals of biomedical engineering*, vol. 2, no. 3, pp. 252–264, 1974.

- [22] D. R. Merrill, M. Bikson, and J. G. Jefferys, "Electrical stimulation of excitable tissue : design of efficacious and safe protocols," *Journal of neuroscience methods*, vol. 141, no. 2, pp. 171–198, 2005.
- [23] D. A. Nelson, G. S. Donaldson, and H. Kreft, "Forward-masked spatial tuning curves in cochlear implant users," *The Journal of the Acoustical Society of America*, vol. 123, no. 3, pp. 1522–1543, 2008.
- [24] M. Bingabr, B. Espinoza-Varas, and P. C. Loizou, "Simulating the effect of spread of excitation in cochlear implants," *Hearing research*, vol. 241, no. 1-2, pp. 73–79, 2008.
- [25] R. L. Snyder, J. C. Middlebrooks, and B. H. Bonham, "Cochlear implant electrode configuration effects on activation threshold and tonotopic selectivity," *Hearing research*, vol. 235, no. 1-2, pp. 23–38, 2008.
- [26] D. A. Groves and V. J. Brown, "Vagal nerve stimulation : a review of its applications and potential mechanisms that mediate its clinical effects," *Neuroscience & Biobehavioral Reviews*, vol. 29, no. 3, pp. 493–500, 2005.
- [27] D. S. Kern and R. Kumar, "Deep brain stimulation," *The Neurologist*, vol. 13, no. 5, pp. 237–252, 2007.
- [28] T. J. Foutz, D. M. Ackermann Jr, K. L. Kilgore, and C. C. McIntyre, "Energy efficient neural stimulation : coupling circuit design and membrane biophysics," *PLoS One*, vol. 7, no. 12, p. e51901, 2012.
- [29] M. Sahin and Y. Tie, "Non-rectangular waveforms for neural stimulation with practical electrodes," *Journal of neural engineering*, vol. 4, no. 3, p. 227, 2007.
- [30] G. P. Walcott, S. B. Melnick, F. W. Chapman, J. L. Jones, W. M. Smith, and R. E. Ideker, "Relative efficacy of monophasic and biphasic waveforms for transthoracic defibrillation after short and long durations of ventricular fibrillation," *Circulation*, vol. 98, no. 20, pp. 2210–2215, 1998.
- [31] O. Roy and R. Wehnert, "A more efficient waveform for cardiac stimulation," *Medical and biological engineering*, vol. 9, no. 5, pp. 495–501, 1971.
- [32] P. J. Rousche, D. S. Pellinen, D. P. Pivin, J. C. Williams, R. J. Vetter, and D. R. Kipke, "Flexible polyimide-based intracortical electrode arrays with bioactive capability," *IEEE Transactions on biomedical engineering*, vol. 48, no. 3, pp. 361–371, 2001.
- [33] A. R. Rezai, M. Phillips, K. B. Baker, A. D. Sharan, J. Nyenhuis, J. Tkach, J. Henderson, and F. G. Shellock, "Neurostimulation system used for deep brain stimulation (dbs) : Mr safety issues and implications of failing to follow safety recommendations," *Investigative radiology*, vol. 39, no. 5, pp. 300–303, 2004.

- [34] C. R. Butson and C. C. McIntyre, "Current steering to control the volume of tissue activated during deep brain stimulation," *Brain Stimulation : Basic, Translational, and Clinical Research in Neuromodulation*, vol. 1, no. 1, pp. 7–15, 2008.
- [35] M. Filali, W. D. Hutchison, V. N. Palter, A. M. Lozano, and J. O. Dostrovsky, "Stimulation-induced inhibition of neuronal firing in human subthalamic nucleus," *Experimental brain research*, vol. 156, no. 3, pp. 274–281, 2004.
- [36] E. S. Boyden, F. Zhang, E. Bamberg, G. Nagel, and K. Deisseroth, "Millisecond-timescale, genetically targeted optical control of neural activity," *Nature neuroscience*, vol. 8, no. 9, p. 1263, 2005.
- [37] S. R. Adams and R. Y. Tsien, "Controlling cell chemistry with caged compounds," *Annual review of physiology*, vol. 55, no. 1, pp. 755–784, 1993.
- [38] E. M. Callaway and L. C. Katz, "Photostimulation using caged glutamate reveals functional circuitry in living brain slices," *Proceedings of the National Academy of Sciences*, vol. 90, no. 16, pp. 7661–7665, 1993.
- [39] F. Zhang, A. M. Aravanis, A. Adamantidis, L. de Lecea, and K. Deisseroth, "Circuit-breakers : optical technologies for probing neural signals and systems," *Nature Reviews Neuroscience*, vol. 8, no. 8, p. 577, 2007.
- [40] J. Czapinski, M. Kielbus, J. Kalafut, M. Kos, A. Stepulak, and A. Rivero-Müller, "How to train a cell-cutting-edge molecular tools," *Frontiers in chemistry*, vol. 5, p. 12, 2017.
- [41] J. D. Wells, C. Kao, E. D. Jansen, P. E. Konrad, and A. Mahadevan-Jansen, "Application of infrared light for in vivo neural stimulation," *Journal of biomedical optics*, vol. 10, no. 6, p. 064003, 2005.
- [42] J. Wells, C. Kao, K. Mariappan, J. Albea, E. D. Jansen, P. Konrad, and A. Mahadevan-Jansen, "Optical stimulation of neural tissue in vivo," *Optics letters*, vol. 30, no. 5, pp. 504–506, 2005.
- [43] J. D. Wells, S. Thomsen, P. Whitaker, E. D. Jansen, C. C. Kao, P. E. Konrad, and A. Mahadevan-Jansen, "Optically mediated nerve stimulation : Identification of injury thresholds," *Lasers in surgery and medicine*, vol. 39, no. 6, pp. 513–526, 2007.
- [44] J. Wells, P. Konrad, C. Kao, E. D. Jansen, and A. Mahadevan-Jansen, "Pulsed laser versus electrical energy for peripheral nerve stimulation," *Journal of neuroscience methods*, vol. 163, no. 2, pp. 326–337, 2007.
- [45] H. S. Gougheri and M. Kiani, "Optimal frequency for powering millimeter-sized biomedical implants inside an inductively-powered homecage," in *Engineering in Medicine and Biology Society (EMBC), 2016 IEEE 38th Annual International Conference of the*, pp. 4804–4807, IEEE, 2016.

- [46] F. Zhang, S. A. Hackworth, X. Liu, H. Chen, R. J. Sclabassi, and M. Sun, "Wireless energy transfer platform for medical sensors and implantable devices," in *Engineering in Medicine and Biology Society, 2009. EMBC 2009. Annual International Conference of the IEEE*, pp. 1045–1048, IEEE, 2009.
- [47] P. Yeon, S. A. Mirbozorgi, and M. Ghovanloo, "Optimal design of a 3-coil inductive link for millimeter-sized biomedical implants," in *Biomedical Circuits and Systems Conference (BioCAS), 2016 IEEE*, pp. 396–399, IEEE, 2016.
- [48] S. A. Mirbozorgi, H. Bahrami, M. Sawan, and B. Gosselin, "A smart multicoil inductively coupled array for wireless power transmission," *IEEE Transactions on Industrial Electronics*, vol. 61, no. 11, pp. 6061–6070, 2014.
- [49] S. A. Mirbozorgi, H. Bahrami, L. A. Rusch, and B. Gosselin, "A low-power 2.4-ghz receiver for wireless implantable neural stimulators," in *Circuits and Systems (ISCAS), 2014 IEEE International Symposium on*, pp. 1082–1085, IEEE, 2014.
- [50] H. Bahrami, S. A. Mirbozorgi, L. A. Rusch, and B. Gosselin, "Biological channel modeling and implantable uwb antenna design for neural recording systems," *IEEE Transactions on Biomedical Engineering*, vol. 62, no. 1, pp. 88–98, 2015.
- [51] *IEEE Standard for Safety Levels With Respect to Human Exposure to Radio Frequency Electromagnetic Fields, 3 kHz to 300 GHz, IEEE Std C95.1-2005 (Revision of IEEE Std C95.1-1991)*. 2006.
- [52] C. Wang and G. Shen, "Relationship among sar, rf frequency and tissue," in *International Society for Magnetic Resonance in Medicine (ISMRM) Scientific Meeting & Exhibition*, International Society for Magnetic Resonance in Medicine (ISMRM), 2003.
- [53] R. R. Harrison, "Designing efficient inductive power links for implantable devices," in *Circuits and Systems, 2007. ISCAS 2007. IEEE International Symposium on*, pp. 2080–2083, IEEE, 2007.
- [54] S. S. Mohan, M. del Mar Hershenson, S. P. Boyd, and T. H. Lee, "Simple accurate expressions for planar spiral inductances," *IEEE Journal of solid-state circuits*, vol. 34, no. 10, pp. 1419–1424, 1999.
- [55] N. Soltani, M. S. Aliroteh, and R. Genov, "Cellular inductive powering system for weakly-linked resonant rodent implants," in *Biomedical Circuits and Systems Conference (BioCAS), 2013 IEEE*, pp. 350–353, IEEE, 2013.
- [56] M. Zargham and P. G. Gulak, "Maximum achievable efficiency in near-field coupled power-transfer systems," *IEEE Transactions on Biomedical Circuits and Systems*, vol. 6, no. 3, pp. 228–245, 2012.

- [57] U.-M. Jow and M. Ghovanloo, "Design and optimization of printed spiral coils for efficient transcutaneous inductive power transmission," *IEEE Transactions on biomedical circuits and systems*, vol. 1, no. 3, pp. 193–202, 2007.
- [58] M. Ghovanloo and S. Atluri, "A wide-band power-efficient inductive wireless link for implantable microelectronic devices using multiple carriers," *IEEE Transactions on Circuits and Systems I : Regular Papers*, vol. 54, no. 10, pp. 2211–2221, 2007.
- [59] M. Kiani, U.-M. Jow, and M. Ghovanloo, "Design and optimization of a 3-coil inductive link for efficient wireless power transmission," *IEEE transactions on biomedical circuits and systems*, vol. 5, no. 6, pp. 579–591, 2011.
- [60] U.-M. Jow, M. Kiani, X. Huo, and M. Ghovanloo, "Towards a smart experimental arena for long-term electrophysiology experiments," *IEEE transactions on biomedical circuits and systems*, vol. 6, no. 5, pp. 414–423, 2012.
- [61] F. Inanlou and M. Ghovanloo, "Wideband near-field data transmission using pulse harmonic modulation," *IEEE Transactions on Circuits and Systems I : Regular Papers*, vol. 58, no. 1, pp. 186–195, 2011.
- [62] J. W. Kim, H.-C. Son, D.-H. Kim, J.-R. Yang, K.-H. Kim, K.-M. Lee, and Y.-J. Park, "Wireless power transfer for free positioning using compact planar multiple self-resonators," in *Microwave Workshop Series on Innovative Wireless Power Transmission : Technologies, Systems, and Applications (IMWS), 2012 IEEE MTT-S International*, pp. 127–130, IEEE, 2012.
- [63] A. Kurs, A. Karalis, R. Moffatt, J. D. Joannopoulos, P. Fisher, and M. Soljačić, "Wireless power transfer via strongly coupled magnetic resonances," *science*, vol. 317, no. 5834, pp. 83–86, 2007.
- [64] U.-M. Jow, P. McMenamin, M. Kiani, J. R. Manns, and M. Ghovanloo, "Enercage : A smart experimental arena with scalable architecture for behavioral experiments," *IEEE Transactions on Biomedical Engineering*, vol. 61, no. 1, pp. 139–148, 2014.
- [65] E. G. Kilinc, G. Conus, C. Weber, B. Kawkabani, F. Maloberti, and C. Dehollain, "A system for wireless power transfer of micro-systems in-vivo implantable in freely moving animals," *IEEE Sensors Journal*, vol. 14, no. 2, pp. 522–531, 2014.
- [66] K. Eom, J. Jeong, T. H. Lee, J. Kim, J. Kim, S. E. Lee, and S. J. Kim, "A wireless power transmission system for implantable devices in freely moving rodents," *Medical & biological engineering & computing*, vol. 52, no. 8, pp. 639–651, 2014.
- [67] S. A. Mirbozorgi, Y. Jia, D. Canales, and M. Ghovanloo, "A wirelessly-powered homecage with segmented copper foils and closed-loop power control," *IEEE transactions on biomedical circuits and systems*, vol. 10, no. 5, pp. 979–989, 2016.
- [68] M. Alioto, "Ultra-low power vlsi circuit design demystified and explained : A tutorial," *IEEE Transactions on Circuits and Systems I : Regular Papers*, vol. 59, no. 1, pp. 3–29, 2012.

- [69] S.-C. Luo, C.-J. Huang, and Y.-H. Chu, "A wide-range level shifter using a modified wilson current mirror hybrid buffer," *IEEE Transactions on Circuits and Systems I : Regular Papers*, vol. 61, no. 6, pp. 1656–1665, 2014.
- [70] Y. Osaki, T. Hirose, N. Kuroki, and M. Numa, "A low-power level shifter with logic error correction for extremely low-voltage digital cmos lsis," *IEEE Journal of Solid-State Circuits*, vol. 47, no. 7, pp. 1776–1783, 2012.
- [71] J. Zhou, C. Wang, X. Liu, X. Zhang, and M. Je, "An ultra-low voltage level shifter using revised wilson current mirror for fast and energy-efficient wide-range voltage conversion from sub-threshold to i/o voltage," *IEEE Transactions on Circuits and Systems I : Regular Papers*, vol. 62, no. 3, pp. 697–706, 2015.
- [72] W. Zhao, A. B. Alvarez, and Y. Ha, "A 65-nm 25.1-ns 30.7-fj robust subthreshold level shifter with wide conversion range," *IEEE Transactions on Circuits and Systems II : Express Briefs*, vol. 62, no. 7, pp. 671–675, 2015.
- [73] Y. Ho, S.-Y. Hsu, and C.-Y. Lee, "A variation-tolerant subthreshold to superthreshold level shifter for heterogeneous interfaces," *IEEE Transactions on Circuits and Systems II : Express Briefs*, vol. 63, no. 2, pp. 161–165, 2016.
- [74] Y. Kim, Y. Lee, D. Sylvester, and D. Blaauw, "Slc : Split-control level converter for dense and stable wide-range voltage conversion," in *ESSCIRC (ESSCIRC), 2012 Proceedings of the*, pp. 478–481, IEEE, 2012.
- [75] K. Craig, Y. Shakhsher, S. Arrabi, S. Khanna, J. Lach, and B. H. Calhoun, "A 32 b 90 nm processor implementing panoptic dvs achieving energy efficient operation from sub-threshold to high performance," *IEEE Journal of Solid-State Circuits*, vol. 49, no. 2, pp. 545–552, 2014.
- [76] B. Zhai, L. Nazhandali, J. Olson, A. Reeves, M. Minuth, R. Helfand, S. Pant, D. Blaauw, and T. Austin, "A 2.60 pj/inst subthreshold sensor processor for optimal energy efficiency," in *VLSI Circuits, 2006. Digest of Technical Papers. 2006 Symposium on*, pp. 154–155, IEEE, 2006.
- [77] E. Maghsoudloo, M. Rezaei, M. Sawan, and B. Gosselin, "A power-efficient wide-range signal level-shifter," in *New Circuits and Systems Conference (NEWCAS), 2015 IEEE 13th International*, pp. 1–4, IEEE, 2015.
- [78] M. Lanuzza, P. Corsonello, and S. Perri, "Low-power level shifter for multi-supply voltage designs," *IEEE Transactions on Circuits and Systems II : Express Briefs*, vol. 59, no. 12, pp. 922–926, 2012.
- [79] S. N. Wooters, B. H. Calhoun, and T. N. Blalock, "An energy-efficient subthreshold level converter in 130-nm cmos," *IEEE Transactions on Circuits and Systems II : Express Briefs*, vol. 57, no. 4, pp. 290–294, 2010.

- [80] H. Shao and C.-Y. Tsui, "A robust, input voltage adaptive and low energy consumption level converter for sub-threshold logic," in *Solid State Circuits Conference, 2007. ESSCIRC 2007. 33rd European*, pp. 312–315, IEEE, 2007.
- [81] S. Lutkemeier and U. Ruckert, "A subthreshold to above-threshold level shifter comprising a wilson current mirror," *IEEE Transactions on Circuits and Systems II : Express Briefs*, vol. 57, no. 9, pp. 721–724, 2010.
- [82] Y. Kim, D. Sylvester, and D. Blaauw, "Lc 2 : Limited contention level converter for robust wide-range voltage conversion," in *VLSI Circuits (VLSIC), 2011 Symposium on*, pp. 188–189, IEEE, 2011.
- [83] D. A. Johns and K. Martin, *Analog integrated circuit design*. John Wiley & Sons, 2012.
- [84] N. H. Weste and D. Harris, *CMOS VLSI design : a circuits and systems perspective*. Pearson Education India, 2015.
- [85] M. Lanuzza, F. Crupi, S. Rao, R. De Rose, S. Strangio, and G. Iannaccone, "An ultralow-voltage energy-efficient level shifter," *IEEE Transactions on Circuits and Systems II : Express Briefs*, vol. 64, no. 1, pp. 61–65, 2017.
- [86] Y. Jia, Z. Wang, D. Canales, M. Tinkler, C.-C. Hsu, T. E. Madsen, S. A. Mirbozorgi, D. Rainnie, and M. Ghovanloo, "A wirelessly-powered homecage with animal behavior analysis and closed-loop power control," in *Engineering in Medicine and Biology Society (EMBC), 2016 IEEE 38th Annual International Conference of the*, pp. 6323–6326, IEEE, 2016.
- [87] K. Eom, J. Jeong, T. H. Lee, S. E. Lee, S. B. Jun, and S. J. Kim, "Columnar transmitter based wireless power delivery system for implantable device in freely moving animals," in *Engineering in Medicine and Biology Society (EMBC), 2013 35th Annual International Conference of the IEEE*, pp. 1859–1862, IEEE, 2013.
- [88] S. A. Mirbozorgi, H. Bahrami, M. Sawan, L. A. Rusch, and B. Gosselin, "A single-chip full-duplex high speed transceiver for multi-site stimulating and recording neural implants," *IEEE transactions on biomedical circuits and systems*, vol. 10, no. 3, pp. 643–653, 2016.
- [89] U.-M. Jow and M. Ghovanloo, "Optimization of data coils in a multiband wireless link for neuroprosthetic implantable devices," *IEEE transactions on biomedical circuits and systems*, vol. 4, no. 5, pp. 301–310, 2010.
- [90] A. Ebrazeh and P. Mohseni, "30 pj/b, 67 mbps, centimeter-to-meter range data telemetry with an ir-uwv wireless link," *IEEE transactions on biomedical circuits and systems*, vol. 9, no. 3, pp. 362–369, 2015.
- [91] M. Rezaei, H. Bahrami, A. Mirbozorgi, L. A. Rusch, and B. Gosselin, "A short-impulse uwv bpsk transmitter for large-scale neural recording implants," in *Engineering in Medicine and Biology Society (EMBC), 2016 IEEE 38th Annual International Conference of the*, pp. 6315–6318, IEEE, 2016.

- [92] S. A. Mirbozorgi, H. Bahrami, M. Sawan, and B. Gosselin, "A smart cage with uniform wireless power distribution in 3d for enabling long-term experiments with freely moving animals," *IEEE transactions on biomedical circuits and systems*, vol. 10, no. 2, pp. 424–434, 2016.
- [93] M. Rezaei and B. Gosselin, "Low-power high-speed wireless transceivers and antennas for large-scale neural implants," in *New Circuits and Systems Conference (NEWCAS), 2016 14th IEEE International*, pp. 1–4, IEEE, 2016.
- [94] S. C. Tang and N. J. McDannold, "Power loss analysis and comparison of segmented and unsegmented energy coupling coils for wireless energy transfer," *IEEE journal of emerging and selected topics in power electronics*, vol. 3, no. 1, pp. 215–225, 2015.
- [95] M. Hashimoto, A. Hata, T. Miyata, and H. Hirase, "Programmable wireless light-emitting diode stimulator for chronic stimulation of optogenetic molecules in freely moving mice," *Neurophotonics*, vol. 1, no. 1, p. 011002, 2014.
- [96] G. Gagnon-Turcotte, Y. LeChasseur, C. Bories, Y. De Koninck, and B. Gosselin, "An optimized adaptive spike detector for behavioural experiments," in *Circuits and Systems (ISCAS), 2016 IEEE International Symposium on*, pp. 1098–1101, IEEE, 2016.
- [97] G. Gagnon-Turcotte, E. Maghsoudloo, Y. Messaddeq, Y. De Koninck, and B. Gosselin, "A wireless photostimulator for optogenetics with live animals," in *New Circuits and Systems Conference (NEWCAS), 2017 15th IEEE International*, pp. 193–196, IEEE, 2017.
- [98] E. Maghsoudloo, M. Rezaei, and B. Gosselin, "A wirelessly powered high-speed transceiver for high-density bidirectional neural interfaces," in *Circuits and Systems (ISCAS), 2017 IEEE International Symposium on*, pp. 1–4, IEEE, 2017.
- [99] M. Ghovanloo and K. Najafi, "Fully integrated wideband high-current rectifiers for inductively powered devices," *IEEE Journal of Solid-State Circuits*, vol. 39, no. 11, pp. 1976–1984, 2004.
- [100] G. Rincon-Mora, *Analog IC design with low-dropout regulators (LDOs)*. McGraw-Hill, Inc., 2009.
- [101] W. Jung, "Voltage references and low dropout linear regulators," *Analog-Digital Conversion Handbook*, 2004.
- [102] Y. LeChasseur, S. Dufour, G. Lavertu, C. Bories, M. Deschênes, R. Vallée, and Y. De Koninck, "A microprobe for parallel optical and electrical recordings from single neurons in vivo," *Nature methods*, vol. 8, no. 4, p. 319, 2011.
- [103] L. Verret, E. O. Mann, G. B. Hang, A. M. Barth, I. Cobos, K. Ho, N. Devidze, E. Masliah, A. C. Kreitzer, I. Mody, *et al.*, "Inhibitory interneuron deficit links altered network activity and cognitive dysfunction in alzheimer model," *Cell*, vol. 149, no. 3, pp. 708–721, 2012.
- [104] K. Yamamoto, Z.-i. Tanei, T. Hashimoto, T. Wakabayashi, H. Okuno, Y. Naka, O. Yizhar, L. E. Fenno, M. Fukayama, H. Bito, *et al.*, "Chronic optogenetic activation augments $\alpha\beta$ pathology in a mouse model of alzheimer disease," *Cell reports*, vol. 11, no. 6, pp. 859–865, 2015.

- [105] K. V. Kastanenka, S. S. Hou, N. Shakerdge, R. Logan, D. Feng, S. Wegmann, V. Chopra, J. M. Hawkes, X. Chen, and B. J. Bacskaï, “Optogenetic restoration of disrupted slow oscillations halts amyloid deposition and restores calcium homeostasis in an animal model of alzheimer’s disease,” *PloS one*, vol. 12, no. 1, p. e0170275, 2017.
- [106] D. A. Borton, M. Yin, J. Aceros, and A. Nurmikko, “An implantable wireless neural interface for recording cortical circuit dynamics in moving primates,” *Journal of neural engineering*, vol. 10, no. 2, p. 026010, 2013.
- [107] C. A. Chestek, V. Gilja, P. Nuyujukian, R. J. Kier, F. Solzbacher, S. I. Ryu, R. R. Harrison, and K. V. Shenoy, “Hermesc : low-power wireless neural recording system for freely moving primates,” *IEEE Transactions on Neural Systems and Rehabilitation Engineering*, vol. 17, no. 4, pp. 330–338, 2009.
- [108] P. Cong, N. Chaimanonart, W. H. Ko, and D. J. Young, “A wireless and batteryless 130mg 300 μ w 10b implantable blood-pressure-sensing microsystem for real-time genetically engineered mice monitoring,” in *Solid-State Circuits Conference-Digest of Technical Papers, 2009. ISSCC 2009. IEEE International*, pp. 428–429, IEEE, 2009.
- [109] A. K. RamRakhiani, S. Mirabbasi, and M. Chiao, “Design and optimization of resonance-based efficient wireless power delivery systems for biomedical implants,” *IEEE Transactions on Biomedical Circuits and Systems*, vol. 5, no. 1, pp. 48–63, 2011.
- [110] S. Mirbozorgi, M. Sawan, and B. Gosselin, “Multicoil resonance-based parallel array for smart wireless power delivery,” in *Engineering in Medicine and Biology Society (EMBC), 2013 35th Annual International Conference of the IEEE*, pp. 751–754, IEEE, 2013.
- [111] R. E. Millard and R. K. Shepherd, “A fully implantable stimulator for use in small laboratory animals,” *Journal of neuroscience methods*, vol. 166, no. 2, pp. 168–177, 2007.
- [112] Y. Jia, S. A. Mirbozorgi, Z. Wang, C.-C. Hsu, T. E. Madsen, D. Rainnie, and M. Ghovanloo, “Position and orientation insensitive wireless power transmission for enercage-homecage system,” *IEEE Transactions on Biomedical Engineering*, vol. 64, no. 10, pp. 2439–2449, 2017.
- [113] E. Maghsoudloo, G. Gagnon-Turcotte, Z. Rezaei, and B. Gosselin, “A smart neuroscience platform with wireless power transmission for simultaneous optogenetics and electrophysiological recording,” in *Circuits and Systems (ISCAS), 2018 IEEE International Symposium on*, pp. 1–4, IEEE, 2018.
- [114] K. L. Montgomery, A. J. Yeh, J. S. Ho, V. Tsao, S. M. Iyer, L. Grosenick, E. A. Ferenczi, Y. Tanabe, K. Deisseroth, S. L. Delp, *et al.*, “Wirelessly powered, fully internal optogenetics for brain, spinal and peripheral circuits in mice,” *Nature methods*, vol. 12, no. 10, pp. 969–974, 2015.
- [115] S. I. Park, D. S. Brenner, G. Shin, C. D. Morgan, B. A. Copits, H. U. Chung, M. Y. Pullen, K. N. Noh, S. Davidson, S. J. Oh, *et al.*, “Soft, stretchable, fully implantable miniaturized op-

toelectronic systems for wireless optogenetics,” *Nature biotechnology*, vol. 33, no. 12, p. 1280, 2015.

- [116] B. R. Arenkiel, J. Peca, I. G. Davison, C. Feliciano, K. Deisseroth, G. J. Augustine, M. D. Ehlers, and G. Feng, “In vivo light-induced activation of neural circuitry in transgenic mice expressing channelrhodopsin-2,” *Neuron*, vol. 54, no. 2, pp. 205–218, 2007.